UNIVERSITÀ DEGLI STUDI DI PADOVA

Sede Amministrativa: Università degli Studi di Padova

Dipartimento di Scienze Chimiche

CORSO DI DOTTORATO DI RICERCA IN: Scienze molecolari

CURRICOLO: Chimica

CICLO: XXXIV

Investigating energy and charge transfers in hybrid molecule-nanoparticle systems through atomistic computational methods

Tesi redatta con il contributo finanziario del Ministero dell'Istruzione dell'Università e della Ricerca attraverso il progetto PLASMOCHEM afferente al programma Framework per l'Attrazione e il Rafforzamento delle Eccellenze per la ricerca in Italia

Coordinatore: Ch.mo Prof. Leonard Prins

Supervisore: Ch.mo Prof. Stefano Corni

Dottorando: Mirko Vanzan

To my past self for never stop believing

To my present self for the efforts spent

To my future self as a reminder for the strength of my willpower

Per aspera ad astra

Abstract

Light-matter interaction at the nanoscale is known to produces a wide variety of unique phenomena, whose origins are intimately connected to the ultra-small dimensions of the systems. Understanding those effects within a comprehensive and unitary paradigm represent one of the main challenges of modern nanoscience and is pivotal for the development of future effective technologies. Although the physics behind these phenomena are generally well characterized on the basis of fundamental processes, there is still an open debate about the way these light-matter interactions affect molecules when they are interacting with nanosystems. The proposed theoretical approaches usually interpret these evidences on the basis of single phenomenon such as charge-transfer or carriers excitation, neglecting the role the other processes can play. This naturally limits the predictive and explanatory power of the theories which should account not only for all the effects occurring, but also for their mutual interplay.

This thesis aims to propose new perspectives on the theoretical treatment of light-matter interaction at the nanoscale, demonstrating the pivotal role some mechanisms usually neglected can play in hybrid molecule-nanoparticle devices. These evidences were achieved applying atomistic methods based on classical and ab-initio computational approaches on technologically relevant nanosystems such as atomically precise metal aggregates and nanoparticle surfaces, interacting with atomic or molecular species. The new perspectives proposed allowed (or at least laid the foundations) for atomistic inspections of relevant phenomena like photo-driven carbon dioxide reduction, enhanced lanthanide ions emission, hot-carriers mediated reactions, and nanoalloys photochemistry. Specifically, the main outcomes of this thesis include: findings on the nature of the energy transfer occurring when small metallic nanoclusters enhances lanthanide ions luminescence, a precise characterization of the Rh-catalysed carbon dioxide reduction rate-determining step, evidences about the hot-carriers capability to effectively transfer energy to molecules absorbed on the nanoparticle surface selectively stimulating particular vibrational modes; a rigorous analysis of gold-rhodium aggregates which sizes ranges between 20-150 atoms.

The novelty and the quality of the results collected in this thesis, mostly corroborated with experimental observations, provide new rationale on the physics behind nano-supported photo-stimulated processes and constitute a solid base for future inspections on light-matter interaction at this scale.

Sommario

È noto che su scala nanometrica l'interazione luce-materia produce un'ampia varietà di fenomeni, le cui origini sono intimamente legate alle dimensioni molto piccole dei sistemi. La comprensione di questi effetti all'interno di un paradigma completo e unitario rappresenta una delle principali sfide della moderna nanoscienza ed è fondamentale per lo sviluppo di nuove tecnologie. Sebbene la fisica alla base di questi fenomeni sia ben caratterizzata sulla base dei processi fondamentali, esiste ancora un dibattito aperto sul modo in cui queste interazioni influenzano le molecole quando queste interagiscono con nanosistemi. Gli approcci teorici proposti interpretano queste evidenze sulla base di singoli fenomeni come il trasferimento di carica o l'eccitazione di portatori, trascurando il ruolo che altri processi possono avere. Questo naturalmente limita il potere predittivo ed esplicativo delle teorie che dovrebbero rendere conto non solo di tutti gli effetti che si possono verificare, ma anche della loro reciproca interazione.

Questa tesi mira a proporre nuove prospettive sul trattamento teorico dell'interazione luce-materia su scala nanometrica, dimostrando il ruolo fondamentale che alcuni meccanismi solitamente trascurati possono giocare in sistemi ibridi composti da molecole e nanoparticelle. Queste evidenze sono state ottenute applicando metodi atomistici classici e ab-initio, su sistemi tecnologicamente rilevanti, come aggregati metallici atomicamente precisi e superfici di nanoparticelle interagenti con specie atomiche o molecolari. Le nuove prospettive proposte hanno permesso (o almeno gettato le basi per) una analisi a livello atomistico di fenomeni rilevanti come la riduzione fotostimolata dell'anidride carbonica, l'emissione stimolata da parte di ioni lantanidi, le reazioni mediate dai portatori caldi e la fotochimica delle nanoleghe. In particolare, i principali risultati di questa tesi includono: scoperte sulla natura del trasferimento di energia tra piccoli nanocluster metallici e ioni lantanidi, una caratterizzazione precisa dello step limitante della riduzione dell'anidride carbonica catalizzata da rodio, evidenze sulla capacità dei portatori caldi di trasferire energia alle molecole assorbite sulla superficie delle nanoparticelle stimolando selettivamente particolari modi vibrazionali; un'analisi rigorosa degli aggregati oro-rodio le cui dimensioni variano tra 20-150 atomi.

La novità e la qualità dei risultati raccolti in questa tesi, per lo più corroborati da osservazioni sperimentali, forniscono nuove prospettive sulla fisica soggiacente processi fotostimolati supportati dalle nanoparticelle e costituiscono una solida base per futuri studi sull'interazione luce-materia a questa scala.

Contents

Introduction

The study of light-matter interaction at the nanoscale is undoubtedly one of the most exciting and promising field of modern nanoscience.[1] The reduced dimensions of the systems and the consequent quantized nature of the physical phenomena occurring at these scale, makes them extremely effective in manipulating electromagnetic radiations with nanometric accuracy, opening brand new opportunities in the field of applied nanophotonics.

When light and nanosystems interact in the proper way, specific collective electronic modes are excited by the external radiation, leading to a condition where the electromagnetic energy is converted into the energy of an oscillating electronic cloud. This phenomenon is called Surface Plasmon Resonance (SPR) and is one of the most peculiar and relevant features of optically active nanosystems possessing free conduction electrons. By properly tuning structural properties of nanostructures such as shape or composition, it is indeed possible to precisely manage the physics of the SPR. This in turn allow an highly-accurate manipulation of the electromagnetic radiation at the nanometric scale, potentially affecting a wide variety of technological relevant fields such as photonics, catalysis, nanomedicine, renewable energy and material sciences.[2,3] As examples, consider that modern probing techniques such as Surface Enhanced Raman Spectroscopy, Tip Enhanced Raman Scattering or Plasmon Enhanced Fluorescence Spectroscopy are based on SPR and, specifically, exploit the enormous enhancement of the electric field occurring in the proximity of the structure, when SPR is activated.[4–6]

During the past 20 years, the community started to investigate the role of SPR in hybrid nanostructure-molecular devices i.e., systems where a molecular species is chemically bounded to nanoparticle surface. In this configuration, the discrete electronic structure of the molecule is strongly hybridized with the band-like energy level distribution of the nanosystem (usually a metallic nanoparticle). When a proper external electromagnetic field stimulates one of the optical excitations of the system e.g., the nanoparticle SPR, peculiar phenomena can arise within the nanosystem-molecule interface, with profound consequences for the chemical and physical features of the molecular species.[7]

One of these phenomena is the Effective Energy Transfer (EET) from the nanoparticle to the adsorbed species. Here the optical excitation, originally localized within the nanosystems, is transferred to the molecule, providing a configuration where the species is electronically excited.[8,9] Depending on the way the species relaxes the acquired excitation, there are a few processes can

then occur: the transferred energy can be radiatively emitted, thus increasing the molecular emission quantum yield; can prompt chemical reactions, thus allowing to follow certain reaction energy paths that without EET would be forbidden; or can be thermally dissipated, gradually relaxing within the vibrational structure and exciting specific vibrational excitation.[8,9]

To date, there is not a comprehensive and unified mechanism describing how this effect occur within these nanostructure-molecule devices. Filling this modelling gap is something of primarily importance for the nanoscience community since controlling EET and its consequent features could have large impacts on applications such as renewable energy[10,11], highly sensible spectroscopic imaging tecniques[12,13] and telecommunications.[14,15]

As first step to properly model this physical phenomenon, it is possible to rely on what is already known about how this process occurs among molecules in solution. It is indeed well-known within the photochemistry community how EET phenomena can be selectively stimulates when two molecular systems are opportunely coupled. Describing in detail how the various EET mechanism works in these systems is out of the scope of this thesis, however it is important to remark how these processes strongly depends on the molecular relative orientation, their mutual distance, the proper alignment of their transition dipole moments and the relative difference among the donor and acceptor energy levels.[8,16] Typical examples of systems which efficiently exploit EET are the organic complexes of lanthanide ions. In these systems, the radiation is first absorbed by the organic ligands, also called “antenna”, providing a configuration where it is excited in a singlet state. The excitation is then converted via intersystem crossing into a long living triplet state and then transferred to one of the lanthanide accepting levels. The ions finally relaxes the excitation by radiative emission, emitting with radiative quantum yield impressively larger than the one of the isolated lanthanide ion.[17] Having in mind this mechanism, it could be argued if this picture can be successfully applied to systems where the role of antenna is hold by a nanostructure. If so, this could provide a solid base for the development of the theoretical framework formerly mentioned.

Another notable class of technologically relevant outcomes of nanosystems optical excitation and in particular the SPR, relies on the exploitation of the energy released by its decay, via charge transfer. Besides specific applications in the field of thermoplasmonics[18], the decay of SPR into thermal energy is detrimental for devices aimed to convert or manipulate electromagnetic energy, since it represent the main source of dissipations. However, when properly controlled, it may turn extremely effective and useful for applications such as photocatalysis, solar energy harvesting and sensing.[19–21] To understand this concept it is necessary to recall how the SPR evolves and gradually

dissipates within a nanoparticle. The currently accepted model representing the SPR lifecycle is pictured in Figure 1 and works as follows. During the first tenth of fs following the activation of the SPR, the collective motion of the electron cloud starts to dephase.[22] The plasmon can indeed be considered as combination of single electron-hole transitions initially characterized by in-phase oscillations. The mutual electron-electron interactions prompted by the reduced volume of the systems, gradually changes the relative phases of the single electronic transitions (or, in other terms, promotes the coupling between the SPR and single particle states) thus reducing the whole collective oscillations coherency. Such effect goes under the name of Landau damping and lead to a configuration where most of the energy is redistributed within the electronic system itself as electrons and holes are excited as single particles.[23] These early energy and momentum transfers within the electronic system, result in an out-of-equilibrium distribution of the carriers (Figure 1B) which rapidly relaxes to an equilibrium Fermi-Dirac distribution with an apparent larger temperature than the lattice one (Figure 1C).

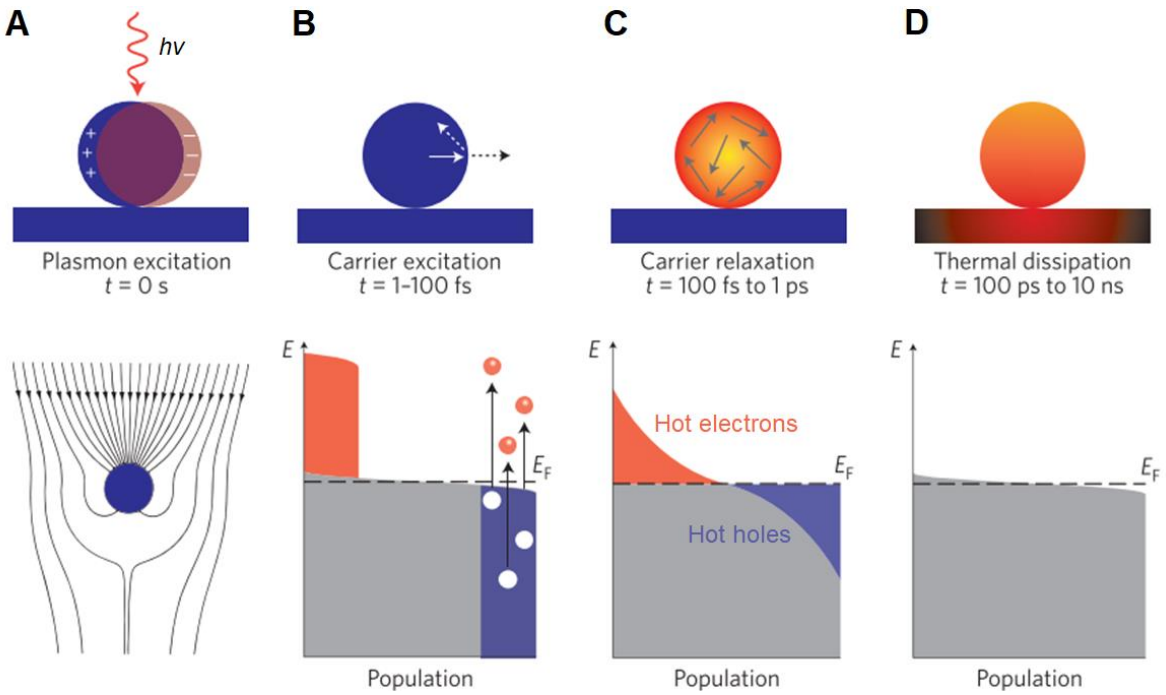

Figure 1. Graphical representation of SPR decays *via* hot-carriers production. First, the SPR is excited with subsequent perturbation of the electromagnetic field around the system (A). Within 1-100 fs the SPR starts to dephase and generate electron–hole pairs (B). In longer timescales the hot-carriers first thermalize with themselves through electron–electron scattering (C) and then with the lattice via electron-phonon coupling, dissipating their energy (D). In this scheme the population of the electronic states are pictured in grey, while hot-electrons and hot-holes are represented in red and blue respectively. All these quantities are defined with respect to the nanoparticle Fermi energy E_F. Figure adapted from ref.[26] Copyright 2015 Nature Publishing Group.

In this state there exist carriers (electrons and holes) whose energies are higher than in the unexcited system, as they are heated up; this is why such particles are named “hot-carriers”. Without further intervention, the carriers preserve their distribution for 100-1000 fs before thermalizing to the ambient temperature through electron-phonon scattering (Figure 1D), recovering the original temperature Fermi-Dirac distribution.[24,25] Else, if the appropriate molecules or interfaces are present, the energetic carriers could interact with these species triggering chemical reaction or being collected into a separate device.[27–29] In the past decade, much effort was spent in order to understand and exploit hot-carriers dynamics in the field of photocatalysis[30,31], further including new species such as multiple plasmonic devices,[32–34] or accounting for alloyed nanoparticles.[35,36] In particular, the latter seems very promising for photocatalytic purposes since, they can join the existence of an intense SPR with high propensity in bounding molecules and activate catalytic processes. This indeed can be obtained by properly alloying optically active metals such as gold and silver, with species showing high catalytical capabilities like palladium, ruthenium and rhodium. Within these systems, plasmonic-related effects such as EET and hot-carriers production, can be effectively exploited and can prompt chemical reactions through the mediation of the catalytic species.[37] The study of nanoalloys is a rapidly growing promising field which, in perspective, can enable new possibilities in applications involving photocatalysis.[38] To date, there are many evidences about the impressive photocatalytic capabilities of these systems toward reactions such as CO_2 reduction, H_2O splitting or reduction of small organic molecules.[39–42] However, a complete understanding of the various features involved in these systems is missing. In particular, there are no theoretical models that can effectively correlate structural features such as chemical arrangement, shape and composition with physico-chemical properties such as the magnetic moment, absorption spectrum and catalytic activity. In this view, a detailed investigation on the way two metals tends to mix within a certain structure and on the properties of the resulting alloy, cannot prescind by the usage of computational atomistic methodologies which allow a precise control over the various parmeters involved in these systems.

As mentioned, these plasmonic-based approaches exploiting energy and charge transfers, already open new ways of thinking about the technological application of metallic nanoparticles.[43–48] The high yields and selectivity of plasmonic stimulated chemical reactions[49,50] persuaded the scientific community to better understand the dynamic of these processes in detail. Despite the mentioned potentiality of plasmonic stimulated chemical reactions to date there is still no general consensus

on the basic mechanisms of plasmon enhanced photocatalysis and even on the role played by energy and charge transfers, preventing a rational design of these devices. Many fundamental questions are under debates and their answer might require efforts from different scientific communities. To name a few, which is the role of surface or bulk optical excitations? What is the precise interplay between charge transfer, energy transfer and molecules? To date, several mechanisms were proposed to justify the impressive photocatalytic capabilities of certain nanostructures, involving carriers transfer to specific adsorbate orbitals, lowering of reactions kinetic energy barriers in the excited state, near fields stimulated intramolecular transitions, or simple local temperature enhancing in proximity of the nanoparticle surface.[51–58]

This thesis approaches some of the mentioned questions, aiming to investigate the dynamics of energy and charge transfer processes occurring in hybrid nanostructure-molecule systems, by applying computational techniques based on ab-initio and atomistic methods.

The choice of study those problems through computational techniques resides in the complexity of the systems that prevent an exhaustive and complete investigation through the sole use of experimental activities. An effective control of all the variables affecting the phenomena would require an atomistic resolution in building the systems and the interfaces, the precise determination of local temperatures, and sub-picoseconds resolutions of the signals.[59–62] Thus, the mechanisms causing and affecting the plasmonic evolution can be only inferred by experimental data, but cannot be directly explored.[63] In this view, the computational methods developed in modern quantum chemistry could provide valuable tools to overcome these difficulties, allowing a detailed insight on the physical processes involved in the systems and contributing to characterize the experimental outcomes. This is why, in recent years, lots of effort were spent to model these phenomena using theoretical approaches. The complexity and variety of this growing literature is remarkable: some of these studies describe SPR either as an effective field acting on the electronic system[64–66], or as stemming directly from the electronic system as one of its possible natural excitation[67–69]; in some works the system is treated on fully atomistic grounds[70–72], in other the plasmonic device is treated as a continuum[73–76]; the interactions within carriers are taken into account at many different levels of accuracy ranging from independent electrons[77–79] to highly correlated quantum chemistry methods[80–82] and finally the electron-nuclei interactions, when accounted, can be estimate either determining the lowest diagrammatic contribution to carriers lifetimes[83,84], or by using non-adiabatic molecular dynamics simulations.[85–87] The variety of methods used to approach this topic

is an evidence of the interest in it, of the challenges it poses and of the different communities that are involved.

Performing theoretical simulation of these processes and precisely controlling all the factors playing within the systems, would represent a privileged point of view which should in principle unambiguously unravel the physics underlying hot-carriers and in general behind all SPR-related effects. Of course, such large advantages are balanced by the great challenges this kind of phenomena poses. Challenges are not only ascribed to the modelling of non-equilibrium excited state dynamics of an interacting electronic system (possibly coupled to the nuclear degrees of freedom) but also to the need of taking into account different components and different space and time scales. For instance, in modelling plasmon-molecules interactions, the electronic coupling at the nanoparticle-adsorbate interface requires an atomistic description of that region, whereas common plasmonic devices size ranges within 10-100 nm; the plasmon decays within 10 fs, but hot-carrier relaxation and thermalization may take 100-1000 fs. To date, an exhaustive and yet sufficiently accurate treatment of this problem is thus far-fetched. Despite these limitations, computational treatments of plasmonic-related phenomena demonstrated to provide meaningful insights and to support the experimental activities, integrating the empirical findings with a more fundamental and theoretical perspectives.[88,89] The research activities contained in this thesis represent valuable cases in this sense.

Here I propose new and original perspectives on the physics underlying energy and charge transfer processes occurring in technologically relevant devices. This allowed novel interpretations on the role the various components of the system have in the observed processes, and provide a new picture where the two investigated processes cannot be treated separately. Notably, despite the nature of the treated systems and the type of inspected mechanisms are very different, all outcomes coming from the simulations highlight the primary importance charge and energy transfers phenomena have in the dynamics of plasmonic devices and suggests that, in proper conditions, they can cooperate toward a common outcome. These evidences were obtained by applying computational approaches based on Density Functional Theory (DFT) techniques and classical Molecular Dynamics (MD) simulations on atomistic models representing four different physical systems, which involves plasmon-driven charge and energy transfers processes. This thesis is divided in four chapters, each treating one of the four systems and is organized as follows.

Chapter 1 is based on the article “Lanthanide Ions Sensitization by Small Noble Metal Nanoclusters” by M. Vanzan, T. Cesca, B. Kalinic, C. Maurizio, G. Mattei and S. Corni, published in *ACS Photonics*,

2021, 8, 1364–1376. The experimental part of this work was performed by the NanoStructures Group of the Department of Physics and Astronomy of University of Padova. The study aims to give a rationale to the physical process involved in the sensitization of lanthanide ions by small noble metal nanoclusters (10-60 atoms), when implanted in a silica matrix. Such lanthanide-sensitizers systems are indeed extremely compelling since, when properly illuminated, energy transfers processes occur between the nanostructures and the ions, leading to massive enhancement of the lanthanide spectral emission, with important consequences in the field of optoelectronics and telecommunications.[90–93] Despite its relevance the precise processes interplaying within the species were not fully understood. The available experimental findings indicate a strong dependence of the enhancement magnitude on the nanoclusters size and composition, but no detailed and comprehensive theoretical framework was proposed to support those data.[14,94,95]

In this chapter it is illustrated how the findings on these systems can be ascribed into a paradigm typically adopted to model the photophysical properties of organic lanthanide complexes in solution, namely the antenna-lanthanide.This was demonstrated by systematically studying the optoelectronic properties of several nanoclusters differing in size and composition, by means of linear-response Time Dependent Density Functional Theory (lr-TDDFT) calculations, accounting also for the presence of the environment and explicitly considers the presence of matrix defects.

Joining what is already known about the mechanism occurring in lanthanide−antenna complexes with the data coming from lr-TDDFT calculation, I was able to demonstrate that the proposed theoretical paradigm can be successfully applied to design and optimize rare-earth ion sensitizers based on metal clusters. Such observations are supported by prior and novel experimental findings and provide new insights on the physics behind the photo-stimulated energy transfer capabilities of these nanosystems.

Chapter 2 is based on the article “Study of the rate-determining step of Rh catalysed CO_2 reduction: Insight on the hydrogen assisted molecular dissociation” by M. Vanzan, M. Marsili and S. Corni, published in *Catalyst*, 2021, 11, 538. Here it is presented a detailed characterization of the energetics and the dynamics of the rate determining step of the rhodium catalysed carbon-dioxide reduction in presence of hydrogen. This work was stimulated by a paper from Zhang et. al. whose demonstrated that CO_2 can be effectively turned into CH_4 in the presence of gaseous hydrogen using as photocatalyst Rh nanocubes.[96] The authors of this paper propose that the reaction is mediated by plasmon-generated hot-carriers which are directly injected into the antibonding orbital of the rhodium-adsorbed CHO* molecular species (* indicates the species is adsorbed on the catalyst

surface), easing its cleavage into CH* and O*. This stage was indeed proved to be the rate determining step of the whole CO_2 methanation reaction.[97,98] However, other light-driven mechanisms can occur when the system is photoexcited and to precisely investigate those possibilities, this reaction step needs to be first well characterized from a thermodynamic point of view. This is why in this paper the Rh-supported CO* conversion into CH* and O* through CHO* formation, was characterized by means of Density Functional Theory and Nudged Elastic Band calculations. Besides this thermodynamic characterization, the chapter contains a series of investigations conducted to determine the configurations the various molecules can assume on the Rh (100) surface, which were further refined by exploiting three different computational setups. What emerges from this study is that the rhodium-catalysed CO* to CH* and O* conversion consists of two different subprocesses, which subsequently form and split the CHO* species. The obtained reaction energy profiles together with the predictions on the dynamics of the species are coherent with what is already known on this and on similar systems, and provide a complete and detailed analysis of this reaction stage. These results represent a solid ground for future investigation on the photocatalytic features of Rh nanoparticles, which are currently being investigated within two different lines of research. Such projects aim to analyse (i) the photo-driven mechanisms occurring at the nanoparticle-molecule interface through multiscale real-time analysis of the system electronic wavefunction and (ii) the variation of the reaction thermodynamic landscape in the excited states. Project (i) is conducted in collaboration with the group of Prof. E. Coccia and Prof. M. Stener of University of Trieste within the context of the European sponsored program "Partnership for Advanced Computing in Europe (PRACE)".

Chapter 3 is based on the manuscript "Energy transfer to molecular adsorbates by transient hot-electron tunnelling" by M. Vanzan, G. Gil, D. Castaldo, P. Nordlander and S. Corni, in preparation. This work was conducted in collaboration with Dr. G. Gil from Institute of Cybernetics, Mathematics and Physics of La Habana (Cuba) and Prof. P. Nordlander from Department of Physics and Astronomy, Rice University in Houston (Texas, United States).

This chapter proposes a new perspective on the way hot-carriers can interact with molecules species in hybrid nanoparticle-molecule systems. This approach relies on the possibility of effective energy transfers processes between the hot-carriers and the vibrational states of the adsorbate, occurring when the carriers transiently transfer from the nanostructure to the molecular adsorbate, via tunnel effect. This charge-mediated energy transfer mechanism was investigated by means of real-time Time Dependent Density Functional Theory (rt-TDDFT) calculations, adopting simplified model

systems representing the nanoparticle-molecule interface and focusing on the interactions among the molecular species and a single hot-electron moving within the systems.

The outcomes of the calculations clearly show how, within this framework, certain molecular vibrational modes are selectively activated by the interaction with the hot-electron and the entity on this activation strongly depends on the nature of target molecule and on the energy of hot-electron itself. These observations, support the available experimental evidences and allow new atomistic-based interpretations of the processes occurring in hot-carriers mediate reactions involving small molecules, highlighting in particular the role the molecule itself has in the process. Finally, I estimate this mechanism can provide non-negligible contributions (up to 10^{-1} eV) to the whole reaction energetics when the effect of the injection of several hot-electrons, previously generated within the nanoparticle, is cumulatively accounted. This in turn suggests that such inelastic energy transfer mechanism could have a relevant role and has to be accounted as one of the possible processes involved in plasmonic-driven photocatalysis.

Chapter 4 is based on the manuscript "Exploring AuRh nanoalloys: a computational perspective on synthesis and physical properties" by M. Vanzan, R. M. Jones, S. Corni, R. D'Agosta and F. Baletto, submitted to *ChemPhysChem*, for a special issue dedicated to the synthesis and modelling of alloy nanoparticles. This work was conducted in collaboration with Prof. R. D'Agosta from Department of Polymers and Advanced Materials of University of the Basque Country (Spain) and Prof. F. Baletto from University of Milano, thanks to the HPC-EUROPA3 program for transnational collaboration, which financed this work upon awarding a research proposal. With such grant I could spend a 3-months visiting Prof. D'Agosta and Prof. Baletto at the University of the Basque Country (Spain).

This chapter resumes a computational study on the synthesis and the physical properties of AuRh nanoalloys, which sizes ranges between 20 and 150 atoms. AuRh nanoalloys was indeed proven to have a superb photocatalytic activity towards several technologically relevant reactions.[36,41,99–103] However to date, the sparse investigations on these systems did not highlight neither the precise mechanism behind their photocatalytic performances, nor their most favourable arrangement and physical properties. This work aims to supply this lack of information, by investigating how gold and rhodium can aggregate at the nanoscale and how the properties of the obtained alloys depends on their shapes and composition, exploiting a multiscale approach based on MD and DFT simulations.

Starting from what is already known about the stability of small gold and rhodium nanoclusters, three different synthetic protocols for the AuRh alloys were tested. These procedures, produced a set of notable nanostructures, some of which were then studied with ab-initio accuracy.

Interestingly, regardless the synthetic procedure adopted, the simulations always generate structures marked by a strong phase segregation presenting a Rh@Au core-shell ordering. Ab-initio investigation revealed noticeable physical and geometrical features such as unusual magnetic moments or IR-localized energy gaps. Notably, such properties seem to be strongly correlated to the symmetry assumed by the inner Rh core, which axial tilting determine the properties of the whole system.

All results collected in the mentioned chapters are presented in the form of published papers and related supporting information, as well as unpublished manuscripts with appendixes. Each chapter is introduced by a short section where I highlight my specific contributions to the work.

Compared to the initial state of the art, the approaches and the results presented in this thesis provide novel and effective interpretations of plasmon-driven energy and charge transfer processes and their interplay, lay the foundation for future and more sophisticated investigations on technologically relevant applications and shine new light on the various processes taking place within the field of plasmonic-mediated photochemistry.

Bibliography

1 S. A. Maier, *Plasmonics: Fundamentals and Applications*, Springer, New York, NY, 1st edn., 2007.

2 V. G. Kravets, A. V. Kabashin, W. L. Barnes and A. N. Grigorenko, *Chem. Rev.*, 2018, **118**, 5912–5951.

3 H. Yu, Y. Peng, Y. Yang and Z. Y. Li, *npj Comput. Mater.*, 2019, **5**, 45.

4 R. Pilot, R. Signorini, C. Durante, L. Orian, M. Bhamidipati and L. Fabris, *Biosensors*, 2019, **9**, 57.

5 P. Verma, *Chem. Rev.*, 2017, **117**, 6447–6466.

6 J. F. Li, C. Y. Li and R. F. Aroca, *Chem. Soc. Rev.*, 2017, **46**, 3962–3979.

7 A. J. Wilson and K. A. Willets, *Annu. Rev. Anal. Chem.*, 2016, **9**, 27–43.

8 G. A. Jones and D. S. Bradshaw, *Front. Phys.*, 2019, **7**, 1–19.

9 L. Y. Hsu, W. Ding and G. C. Schatz, *J. Phys. Chem. Lett.*, 2017, **8**, 2357–2367.

10 S. K. Cushing, J. Li, F. Meng, T. R. Senty, S. Suri, M. Zhi, M. Li, A. D. Bristow and N. Wu, *J. Am. Chem. Soc.*, 2012, **134**, 15033–15041.

11 J. Li, S. K. Cushing, F. Meng, T. R. Senty, A. D. Bristow and N. Wu, *Nat. Photonics*, 2015, **9**, 601–607.

12 Y. Choi, Y. Park, T. Kang and L. P. Lee, *Nat. Nanotechnol.*, 2009, **4**, 742–746.

13 Y. Choi, T. Kang and L. P. Lee, *Nano Lett.*, 2009, **9**, 85–90.

14 T. Cesca, B. Kalinic, C. Maurizio, C. Scian, G. Battaglin, P. Mazzoldi and G. Mattei, *ACS Photonics*, 2015, **2**, 96–104.

15 T. Cesca, B. Kalinic, N. Michieli, C. Maurizio, A. Trapananti, C. Scian, G. Battaglin, P.

Mazzoldi and G. Mattei, *Phys. Chem. Chem. Phys.*, 2015, **17**, 28262–28269.
16 J. T. Yardley, *Introduction to Molecular Energy Transfer*, Academic Press, 1980.
17 Y. Hasegawa, Y. Kitagawa and T. Nakanishi, *NPG Asia Mater.*, 2018, **10**, 52–70.
18 K. Te Lin, H. Lin and B. Jia, *Nanophotonics*, 2020, **9**, 3135–3163.
19 Y. H. Jang, Y. J. Jang, S. Kim, L. N. Quan, K. Chung and D. H. Kim, *Chem. Rev.*, 2016, **116**, 14982–15034.
20 C. Zhan, X. J. Chen, J. Yi, J. F. Li, D. Y. Wu and Z. Q. Tian, *Nat. Rev. Chem.*, 2018, **2**, 216–230.
21 H. Chatterjee, D. Bardhan, S. K. Pal, K. Yanase and S. K. Ghosh, *J. Phys. Chem. Lett.*, 2021, **12**, 4697–4705.
22 J. B. Khurgin, *Nanophotonics*, 2019, **9**, 453–471.
23 J. B. Khurgin, *Faraday Discuss.*, 2019, **214**, 35–58.
24 P. Christopher and M. Moskovits, *Annu. Rev. Phys. Chem.*, 2017, **68**, 379–398.
25 L. Chang, L. V. Besteiro, J. Sun, E. Y. Santiago, S. K. Gray, Z. Wang and A. O. Govorov, *ACS Energy Lett.*, 2019, **4**, 2552–2568.
26 M. L. Brongersma, N. J. Halas and P. Nordlander, *Nat. Nanotechnol.*, 2015, **10**, 25–34.
27 J. Gargiulo, R. Berté, Y. Li, S. A. Maier and E. Cortés, *Acc. Chem. Res.*, 2019, **52**, 2525–2535.
28 Z. Zhang, C. Zhang, H. Zheng and H. Xu, *Acc. Chem. Res.*, 2019, **52**, 2506–2515.
29 M. Kim, M. Lin, J. Son, H. Xu and J. M. Nam, *Adv. Opt. Mater.*, 2017, **5**, 1700004.
30 Y. Zhang, S. He, W. Guo, Y. Hu, J. Huang, J. R. Mulcahy and W. D. Wei, *Chem. Rev.*, 2018, **118**, 2927–2954.
31 Q. Wei, S. Wu and Y. Sun, *Adv. Mater.*, 2018, **30**, 1802082.
32 D. F. Swearer, R. K. Leary, R. Newell, S. Yazdi, H. Robatjazi, Y. Zhang, D. Renard, P. Nordlander, P. A. Midgley, N. J. Halas and E. Ringe, *ACS Nano*, 2017, **11**, 10281–10288.
33 D. F. Swearer, H. Zhao, L. Zhou, C. Zhang, H. Robatjazi, J. M. P. Martirez, C. M. Krauter, S. Yazdi, M. J. McClain, E. Ringe, E. A. Carter, P. Nordlander and N. J. Halas, *Proc. Natl. Acad. Sci.*, 2016, **113**, 8916–8920.
34 D. F. Swearer, H. Robatjazi, J. M. P. Martirez, M. Zhang, L. Zhou, E. A. Carter, P. Nordlander and N. J. Halas, *ACS Nano*, 2019, **13**, 8076–8086.
35 F. Calvo, *Nanoalloys: From Fundamentals to Emergent Applications*, Elsevier, 2013.
36 N. Kang, Q. Wang, R. Djeda, W. Wang, F. Fu, M. M. Moro, M. D. L. A. Ramirez, S. Moya, E. Coy, L. Salmon, J. L. Pozzo and D. Astruc, *ACS Appl. Mater. Interfaces*, 2020, **12**, 53816–53826.
37 K. Sytwu, M. Vadai and J. A. Dionne, *Adv. Phys. X*, 2019, **4**, 1619480.
38 F. Baletto, *J. Phys. Condens. Matter*, 2019, **31**, 113001.
39 S. Neatu, J. A. Maciá-Agullò, P. Concepciòn and H. Garcia, *J. Am. Chem. Soc.*, 2014, **136**, 15969–15976.
40 H. Li, L. Luo, P. Kunal, C. S. Bonifacio, Z. Duan, J. C. Yang, S. M. Humphrey, R. M. Crooks and G. Henkelman, *J. Phys. Chem. C*, 2018, **122**, 2712–2716.
41 S. García, L. Zhang, G. W. Piburn, G. Henkelman and S. M. Humphrey, *ACS Nano*, 2014, **8**, 11512–11521.
42 S. Zhang, P. Kang, M. Bakir, A. M. Lapides, C. J. Dares and T. J. Meyer, *Proc. Natl. Acad. Sci. U. S. A.*, 2015, **112**, 15809–15814.
43 A. Naldoni, U. Guler, Z. Wang, M. Marelli, F. Malara, X. Meng, L. V. Besteiro, A. O. Govorov, A. V. Kildishev, A. Boltasseva and V. M. Shalaev, *Adv. Opt. Mater.*, 2017, **5**, 1601031.

44 U. Aslam, V. G. Rao, S. Chavez and S. Linic, *Nat. Catal.*, 2018, **1**, 656–665.
45 G. Kumari, X. Zhang, D. Devasia, J. Heo and P. K. Jain, *ACS Nano*, 2018, **12**, 8330–8340.
46 X. Zhang, X. Li, M. E. Reish, D. Zhang, N. Q. Su, Y. Gutie, F. Moreno, W. Yang, H. O. Everitt and J. Liu, *Nanoletters*, 2018, **18**, 1714–1723.
47 A. Gellé, T. Jin, L. De La Garza, G. D. Price, L. V. Besteiro and A. Moores, *Chem. Rev.*, 2020, **120**, 986–1041.
48 C. H. Choi, K. Chung, T. T. H. Nguyen and D. H. Kim, *ACS Energy Lett.*, 2018, **3**, 1415–1433.
49 E. Cortés, *Adv. Opt. Mater.*, 2017, **5**, 1700191.
50 X. Zhang, X. Ke and J. Yao, *J. Mater. Chem. A*, 2018, **6**, 1941–1966.
51 J. Pettine, S. M. Meyer, F. Medeghini, C. J. Murphy and D. J. Nesbitt, *ACS Nano*, 2021, **15**, 1566–1578.
52 L. Zhou, D. F. Swearer, C. Zhang, H. Robatjazi, H. Zhao, L. Henderson, L. Dong, P. Christopher, E. A. Carter, P. Nordlander and N. J. Halas, *Science*, 2018, **362**, 69–72.
53 S. Linic, S. Chavez and R. Elias, *Nat. Mater.*, 2021, **20**, 916–924.
54 Y. Sivan and Y. Dubi, *Appl. Phys. Lett.*, 2020, **117**, 130501.
55 P. K. Jain, *J. Phys. Chem. C*, 2019, **123**, 24347–24351.
56 J. M. P. Martirez and E. A. Carter, *Sci. Adv.*, 2017, **3**, 1–11.
57 J. L. Bao and E. A. Carter, *ACS Nano*, 2019, **13**, 9944–9957.
58 F. Binkowski, T. Wu, P. Lalanne, S. Burger and A. O. Govorov, *ACS Photonics*, 2021, **8**, 1243–1250.
59 Z. Li and D. Kurouski, *Nanophotonics*, 2021, **10**, 1657–1673.
60 S. C. Huang, X. Wang, Q. Zhao, J.-F. Zhu, C.-W. Li, Y.-H. He, S. Hu, M. M. Sartin, S. Yan and B. Ren, *Nat. Commun.*, 2020, **11**, 4211.
61 R. F. Hamans, R. Kamarudheen and A. Baldi, *Nanomaterials*, 2020, **10**, 2377.
62 H. Lee, K. Song, M. Lee and J. Y. Park, *Adv. Sci.*, 2020, **7**, 2001148.
63 J. J. Baumberg, *Faraday Discuss.*, 2019, **214**, 501–511.
64 J. G. Liu, H. Zhang, S. Link and P. Nordlander, *ACS Photonics*, 2018, **5**, 2584–2595.
65 A. Manjavacas, J. G. Liu, V. Kulkarni and P. Nordlander, *ACS Nano*, 2014, **8**, 7630–7638.
66 E. Molinari, J. D. Cox, A. Alabastri, S. Corni, A. Manjavacas, E. A. Carter, P. Nordlander, L. Bursi, R. Zhang, A. Calzolari, F. J. García de Abajo, H. Zhang, Y. Cui and C. M. Krauter, *ACS Nano*, 2017, **11**, 7321–7335.
67 L. V. Besteiro, X. T. Kong, Z. Wang, G. Hartland and A. O. Govorov, *ACS Photonics*, 2017, **4**, 2759–2781.
68 L. Bursi, A. Calzolari, S. Corni and E. Molinari, *ACS Photonics*, 2016, **3**, 520–525.
69 L. Yuan, M. Lou, B. D. Clark, M. Lou, L. Zhou, S. Tian, C. R. Jacobson, P. Nordlander and N. J. Halas, *ACS Nano*, 2020, **14**, 12054–12063.
70 X. Chen, P. Liu and L. Jensen, *J. Phys. D. Appl. Phys.*, 2019, **52**, 363002.
71 P. V. Kumar, T. P. Rossi, M. Kuisma, P. Erhart and D. J. Norris, *Faraday Discuss.*, 2019, **214**, 189–197.
72 T. P. Rossi, P. Erhart and M. Kuisma, *ACS Nano*, 2020, **14**, 9963–9971.
73 C. hyuck Bae and K. S. Lim, *J. Alloys Compd.*, 2019, **793**, 410–417.
74 A. O. Govorov, H. Zhang and Y. K. Gun'Ko, *J. Phys. Chem. C*, 2013, **117**, 16616–16631.
75 J. Codrington, N. Eldabagh, K. Fernando and J. J. Foley, *ACS Photonics*, 2017, **4**, 552–559.
76 L. V. Besteiro, P. Yu, Z. Wang, A. W. Holleitner, G. V. Hartland, G. P. Wiederrecht and A. O.

Govorov, *Nano Today*, 2019, **27**, 120–145.
77 J. R. M. Saavedra, A. Asenjo-Garcia and F. J. García De Abajo, *ACS Photonics*, 2016, **3**, 1637–1646.
78 L. Ranno, S. D. Forno and J. Lischner, *npj Comput. Mater.*, 2018, **4**, 1–7.
79 S. Dal Forno, L. Ranno and J. Lischner, *J. Phys. Chem. C*, 2018, **122**, 8517–8527.
80 F. Ladstädter, U. Hohenester, P. Puschnig and C. Ambrosch-Draxl, *Phys. Rev. B*, 2004, **70**, 235125.
81 D. J. Masiello, *Int. J. Quantum Chem.*, 2014, **114**, 1413–1420.
82 J. Jiang, A. Abi Mansour and P. J. Ortoleva, *J. Chem. Phys.*, 2017, **147**, 054102.
83 A. S. Jermyn, G. Tagliabue, H. A. Atwater, W. A. Goddard, P. Narang and R. Sundararaman, *Phys. Rev. Mater.*, 2019, **3**, 075201.
84 A. Habib, F. Florio and R. Sundararaman, *J. Opt.*, 2018, **20**, 064001.
85 W. Chu, Q. Zheng, O. V. Prezhdo and J. Zhao, *J. Am. Chem. Soc.*, 2020, **142**, 3214–3221.
86 L. Yan, J. Xu, F. Wang and S. Meng, *J. Phys. Chem. Lett.*, 2018, **9**, 63–69.
87 J. Ma, Z. Wang and L. W. Wang, *Nat. Commun.*, 2015, **6**, 10107.
88 P. Narang, R. Sundararaman and H. A. Atwater, *Nanophotonics*, 2016, **5**, 96–111.
89 N. J. Halas, *Faraday Discuss.*, 2019, **214**, 13–33.
90 A. Martucci, M. De Nuntis, A. Ribaudo, M. Guglielmi, S. Padovani, F. Enrichi, G. Mattei, P. Mazzoldi, C. Sada, E. Trave, G. Battaglin, F. Gonella, E. Borsella, M. Falconieri, M. Patrini and J. Fick, *Appl. Phys. A*, 2005, **80**, 557–563.
91 W. C. Wang, B. Zhou, S. H. Xu, Z. M. Yang and Q. Y. Zhang, *Prog. Mater. Sci.*, 2019, **101**, 90–171.
92 H. Fares, H. Elhouichet, B. Gelloz and M. Férid, *J. Appl. Phys.*, 2015, **117**, 193102.
93 M. Mattarelli, M. Montagna, K. Vishnubhatla, A. Chiasera, M. Ferrari and G. C. Righini, *Phys. Rev. B*, 2007, **75**, 125102.
94 T. Cesca, B. Kalinic, C. Maurizio, N. Michieli, C. Scian and G. Mattei, *RSC Adv.*, 2016, **6**, 99376–99384.
95 C. Maurizio, E. Trave, G. Perotto, V. Bello, D. Pasqualini, P. Mazzoldi, G. Battaglin, T. Cesca, C. Scian and G. Mattei, *Phys. Rev. B*, 2011, **83**, 195430.
96 X. Zhang, X. Li, D. Zhang, N. Q. Su, W. Yang, H. O. Everitt and J. Liu, *Nat. Commun.*, 2017, **8**, 14542.
97 T. Avanesian, G. S. Gusmao and P. Christopher, *J. Catal.*, 2016, **343**, 86–96.
98 X. Su, J. Xu, B. Liang, H. Duan, B. Hou and Y. Huang, *J. Energy Chem.*, 2016, **25**, 553–565.
99 H. Lee, Z. H. Liao, P. W. Hsu, Y. C. Wu, M. C. Cheng, J. H. Wang and M. F. Luo, *Phys. Chem. Chem. Phys.*, 2018, **20**, 11260–11272.
100 D. Kim, H. Nam, Y. H. Cho, B. C. Yeo, S. H. Cho, J. P. Ahn, K. Y. Lee, S. Y. Lee and S. S. Han, *ACS Catal.*, 2019, **9**, 8702–8711.
101 X. Wang, H. Wang, N. Maeda and A. Baiker, *Catalysts*, 2019, **9**, 937.
102 Z. Konuspayeva, P. Afanasiev, T. S. Nguyen, L. Di Felice, F. Morfin, N. T. Nguyen, J. Nelayah, C. Ricolleau, Z. Y. Li, J. Yuan, G. Berhault and L. Piccolo, *Phys. Chem. Chem. Phys.*, 2015, **17**, 28112–28120.
103 R. Camposeco, M. Hinojosa-Reyes, S. Castillo, N. Nava and R. Zanella, *Environ. Sci. Pollut. Res.*, 2020, **28**, 10734–10748.

List of publications

List of publications related to this thesis:

- M. Vanzan, T. Cesca, B. Kalinic, C. Maurizio, G. Mattei and S. Corni; "Lanthanide Ions Sensitization by Small Noble Metal Nanoclusters". *ACS Photonics*, **2021**, 8, 1364–1376.
- M. Vanzan, M. Marsili and S. Corni; "Study of the rate-determining step of Rh catalysed CO2 reduction: Insight on the hydrogen assisted molecular dissociation". *Catalyst*, **2021**, 11, 538.
- M. Vanzan, G. Gil, D. Castaldo, P. Nordlander and S. Corni; "Energy transfer to molecular adsorbates by transient hot-electron tunnelling". *In preparation.*
- M. Vanzan, R. M. Jones, R. D'Agosta, S. Corni, and F. Baletto; "Exploring AuRh nanoalloys: a computational perspective on synthesis and physical properties". *ChemPhysChem*, accepted.

List of other publications:

- M. Vanzan and S. Corni; "Role of Organic Ligands Orientation on the Geometrical and Optical Properties of $Au_{25}(SCH_3)_{18}^0$". *J. Phys. Chem. A*, **2018**, 122, 6864−6872. This is a publication predating my PhD, related to the topic of my master's degree thesis.
- M. Vanzan, M. Rosa and S. Corni; "Atomistic insight into the aggregation of $[Au_{25}(SR)_{18}]^q$ nanoclusters". *Nanoscale Advances*, **2020**, 2, 2842. This is mostly related to the topic of my master's degree thesis, that has been expanded and concluded during the initial part of the PhD.
- M. Vanzan, M. Marsili, and S. Corni; "Theoretical approaches for the description of plasmon-generated hot-carriers phenomena". *In preparation.*
- A. Longato, M. Vanzan, S. Corni and A. Martucci; "Optical hydrogen sensing of Au and Pt doped tungsten oxide thin film prepared by sol-gel deposition – an experimental and computational study". *In preparation.*
- E. Coccia, G. Dall'Osto, M. Marsili, M. Vanzan, P. Grobas Illobre, M. Stener, D. Toffoli and S. Corni "Multiscale modelling of charge injection in rhodium nanocubes for CO_2 hydrogenation". *In preparation.*
- T. N. Nguyên Lê, M. Vanzan and S. Corni; "Effect of nanostructure morphology on adsorption of H_2S on ZnO(1010) nanotube surface using DFT calculations". *In preparation*.

The list of authors for the *in preparation* papers may be subject to changes.

Chapter 1. Lanthanide Ions Sensitization by Small Noble Metal Nanoclusters

This chapter aims to study the physics underlying the photo-stimulated energy exchanges occurring between metallic clusters and lanthanide ions when they are inserted in a silica matrix.

Here I investigated the way this mechanism takes place, providing solid evidences this effect can be frame within the antenna-lanthanide paradigm, a model commonly adopted to investigate the photophysical properties of organic complexes of lanthanide ions.

To reach this goal, I first contribute to design the model systems and the calculations setup. Then I autonomously applied linear-response Time Dependent Density Functional Theory calculations on the model systems which consist of a set of pure and alloyed noble metal nanoclusters, varying in sizes and composition, and then compared the computational outcomes with the energy level of the reference lanthanide ion, namely Er^{3+}. Such calculations also accounted for the presence of the dielectric environment, while explicitly considers the presence of matrix defects.

The extensive analysis I carried out as described in this chapter are coherent with the experimental data available in the literature; therefore I stressed the proposed theoretical framework and contribute to suggest new possible experimental measures aimed to make qualitative predictions on the energy transfer capabilities of small Ag aggregates towards Er^{3+}. Thanks to the collaboration of Prof. G. Mattei and Prof. T. Cesca from the NanoStructures Group of the Department of Physics and Astronomy of University of Padova, with whom I had regular discussions during my PhD, we were able to validate these predictions and to empirically sustain the proposed antenna-lanthanide paradigm, as testified by the close connections between the experimental and theoretical outcomes here included. Once confirmed the theoretical predictions, I finally summarized all the results in the form of a manuscript, which became the bearing structure of the final article. Such draft was first improved thanks to the support of the other co-authors and then further enriched by the discussions emerged from the referees comments, which replies were drafted by myself.

The results of this work are here reported in the form of published article, together with corresponding supporting information, reprinted with permission from ACS Photonics 2021, 8, 1364−1376.

ACS Photonics

pubs.acs.org/journal/apchd5

Article

Lanthanide Ions Sensitization by Small Noble Metal Nanoclusters

Mirko Vanzan, Tiziana Cesca,* Boris Kalinic, Chiara Maurizio, Giovanni Mattei, and Stefano Corni*

Cite This: *ACS Photonics* 2021, 8, 1364–1376

Read Online

ACCESS | Metrics & More | Article Recommendations | Supporting Information

ABSTRACT: Rare-earth ions sensitization is, nowadays, a relevant topic in modern technologies. Noble metal nanoclusters can effectively sensitize lanthanide photoluminecence (PL) via excitation energy transfer (EET). Recent experimental works reported how this process strongly depends on the nanoclusters size and composition, however, a comprehensive understanding of this phenomenon is still lacking. Inspired by the current paradigm on the lanthanide−antenna complexes, where light is absorbed by the organic ligand, which then converts to a triplet and transfers the excitation to the lanthanide, we propose it also applies to sensitization by metal clusters. To prove this, we studied the optoelectronic features of several M_N nanoclusters (M = Au, Ag, Au/Ag mix; N = 12, 20, and 58) at the Time Dependent Density Functional Theory (TDDFT) level, including, via simplified models, the silica matrix and its possible defects, and make considerations on the role these features can have on the EET toward Er^{3+} ions. Our analysis suggests that PL enhancement is generally more effective when N = 12 and M = Ag or Au/Ag mix, while the worst cases are obtained when M = Au and N = 58. These findings are coherent with prior experimental data and with novel measures that are here presented for the first time. Notably, we recover that the matrix defects can actively take part in the EET and, in some cases, could be (counterintuitively) beneficial for the process efficiency. Globally, this theoretical framework gives a comprensive rationale that can guide the design of new effective rare-earth ion sensitizers based on metal clusters.

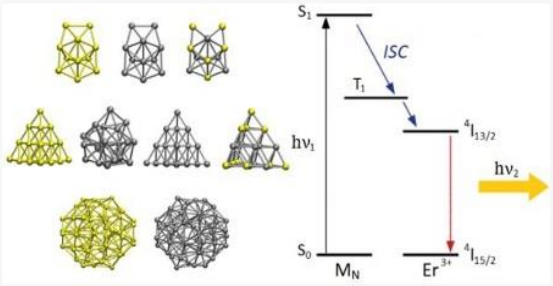

KEYWORDS: *photoluminescence, nanophotonics, energy transfer, lanthanide, nanoclusters, metal nanoclusters, rare-earth sensitization*

In the past years, the study of the optical activity of rare-earth ions has become a relevant topic in the scientific community.[1,2] The reason for such widespread interest resides in the sharp and stable emission that these ions present in the visible and near-IR spectral regions. This peculiar capability makes them fundamental actors in optoelectronic applications such as chemical sensors,[3] waveguides,[4] fiber lasers,[5] and light-emitting diodes (LEDs).[6] A key-role in modern technologies is played by Er^{3+} ions since they present a major emission band, corresponding to the $^4I_{13/2} \rightarrow {}^4I_{15/2}$ transition at 1.54 μm, which is exactly where standard silica glasses have their absorption minimum. For this reason, these ions can be effectively employed in applications such as optical fibers and nanocomposite glasses.[7,8] However, erbium ions suffer from two main problems: they have a poor excitation cross-section ($\sigma \approx 10^{-21}$ cm^2) and they are usually affected by important quenching processes, even at low concentrations.[9,10] As a consequence, the Er^{3+} photoluminescent (PL) emission is suppressed and the devices performances decrease. From the early 2000s, many efforts were spent in order to increase the emission quantum yield of erbium ions embedded in silica glasses, especially by including in the system sensitizers such as other rare-earth ions,[11,12] silicon nanocrystals,[13,14] plasmonic systems,[15,16] or metallic nanoclusters (NCs).[16−20] The latter approach seems to be particularly promising since it was proved that even a small amount of metallic atoms, upon aggregation, can increase the Er^{3+} PL by a factor of 10 or more.[19,21−24] Given the ultrasmall dimensions of these structures (less than 2 nm), the PL enhancement cannot be related to the plasmonic enhancement of the incoming electric field. The mechanism was demonstrated to be a nonradiative, short-range process between the metallic clusters and the Er^{3+} ions.[25,26] A possible explanation of this phenomenon can be given by considering the presence of excitation energy transfer (EET) processes that can take place from the metallic aggregates to the Er^{3+} ions. Such a mechanism is well-known in the organic chemistry community as the "antenna−lanthanide" effect.[27] When an organic−lanthanide complex interacts with a proper electromagnetic field, the beam can be first absorbed by the organic "antenna", which generates a localized singlet excited state. Then by intersystem crossing, this singlet excited state might turn into a less energetic and long-living triplet state that can couple with one of the lanthanide excited states. If the coupling is strong enough, the excitation can be transferred to the lanthanide ion, which in

Received: December 11, 2020
Published: May 3, 2021

https://doi.org/10.1021/acsphotonics.0c01884
ACS Photonics 2021, 8, 1364−1376

turn relaxes to a radiative level and then emits at its peculiar wavelength.[28] This results in an enhanced emission by the lanthanide atoms, stimulated by the absorption of the antenna. Such paradigm can be applied to the NC-erbium case, considering the NC as the antenna. It is indeed well-known that, once excited, ultrasmall noble-metal systems can undergo a singlet−triplet intersystem crossing due to the strong spin−orbit coupling arising from the high mass of the metal atoms.[29−34] However, different NCs enhance the Er^{3+} PL in different ways. This can be seen, for example, by the PL emission results for NCs with $N \approx 10-15$ atoms reported in Figure 1.

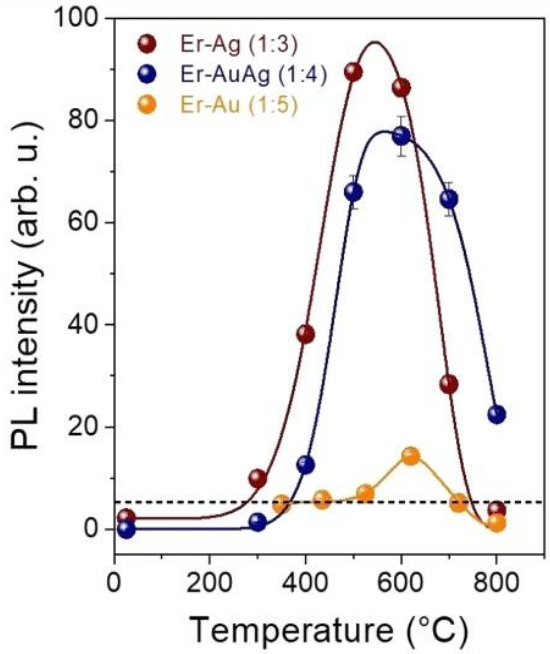

Figure 1. PL intensity of the $Er^{3+4}I_{13/2} \rightarrow {}^4I_{15/2}$ transition as a function of samples annealing temperature of various Er-NC coimplanted silica samples, thermally treated in a N_2 atmosphere. Au, Ag, and AuAg refer to NCs composed of gold, silver, and gold/silver alloy, respectively.[19,23,35] Ratio within rounded brackets refers to the relative Er-metal implantation fluence in the sample (the Er implantation fluence was about 7×10^{14} at/cm^2). The solid lines are to be used as a guide for the eye. The black dashed line indicates the PL emission intensity of the reference sample (Er-implanted silica sample, annealed at 800 °C for 1 h in a N_2 atmosphere). The PL measurements have been taken with excitation at 488 nm, resonant with the ${}^4I_{15/2} \rightarrow {}^4F_{7/2}$ Er^{3+} transition.

Taking into account nanosystems composed of Ag and Au, the main experimental findings coming from PL measurements can be summarized in the following points:

- Ag-based[24,35] and Au/Ag alloy-based NCs[23] can enhance Er^{3+}PL more effectively than Au NCs (see Figure 1).[19,22,25,26]
- In the case of Au_N, structures composed by $N = 10-15$ atoms enhance the lanthanide PL more effectively than larger or smaller aggregates.[19,36] The optimal size tends to increase (to $N = 20-25$) when higher Au fluence is used, with a lower estimated enhancement factor.[22]
- Small Au_N aggregates ($N = 5-10$) can increase the PL more effectively if the samples are annealed in a reducing atmosphere, compared to the samples annealed in an inert atmosphere.[37] The opposite occurs instead for Au_N aggregates, with $N = 20-25$ atoms, for which annealing treatments in a reducing atmosphere, in the temperature region of maximum efficiency (around 600 °C), give rise to a lower Er^{3+} PL enhancement with respect to treatments in an inert atmosphere.[22]

The aim of this work is to understand how the features of the NC antenna can affect the EET capabilities and thus the global Er^{3+} PL enhancement. In particular, we want to verify if the aforementioned experimental evidence can be rationalized in an antenna−lanthanide theoretical framework. To do that, we applied Density Functional Theory (DFT) and Time Dependent Density Functional Theory (TDDFT) on various noble-metal NCs, which differ in size, shape, and chemical nature. Although the complex interplay between the SiO_2 matrix and the NCs is not expected to produce size-controlled NCs,[38,39] we selected specific shapes from the available optimized ones in vacuum. Their structures are reported in Figure 2. The effect of the dielectric silica matrix was modeled in the computational setup, as well as the possible presence of matrix defects.

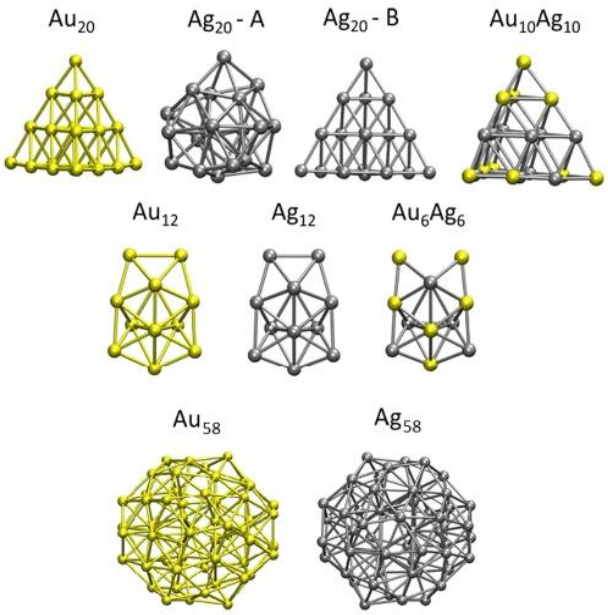

Figure 2. Graphical representation of the investigated nanoclusters. Au atoms are colored in yellow and Ag in gray.

Through these calculations we were able to compare the first triplet excited state (T_1) energy levels of the nanostructures with the emitting ${}^4I_{13/2}$ level of Er^{3+} and to make qualitative considerations on the effectiveness of the T_1 to ${}^4I_{13/2}$ EET process.[30] Additionally, we investigated the role the NCs optical activity can have on the excited states populations and, thus, on the EET rate. Moreover, the impact the excited state geometry relaxation can have on the EET yield and thus on the whole PL enhancement is discussed. Notwithstanding the complexity of the experimental systems compared to the computational setup, our calculations return a coherent theoretical framework and provide a rational for the available literature data within the antenna-lanthanide paradigm. Remarkably, our theoretical approach also allowed us to predict the effect a reducing atmosphere annealing could have

https://doi.org/10.1021/acsphotonics.0c01884
ACS Photonics 2021, 8, 1364−1376

on erbium-doped silica samples, sensitized by small Ag_N aggregates (N = 10−15). Such a prediction was then validated against novel experimental results that are here presented for the first time.

■ COMPUTATIONAL METHODS

Nanoclusters' Geometries and Modeling of Defects. We investigated the T_1 energy level distribution of various noble metal nanostructures considering three main families of NCs: M_{12}, M_{20}, and M_{58} with M = Au, Ag, or a mix of these elements. The structures we considered were chosen on the basis of the information we have on the nanocluster's size under typical experimental conditions, where the sizes for M_N can be divided in three main groups, namely, N = 10−15, 20−25, and 50−60.[19,22,24−26,35−37] Therefore, to properly model such structures, we chose a representative cluster within each of these size ranges. The initial geometries of these systems were adapted from the available literature data. Unfortunately, the precise equilibrium structures of these systems are generally unknown. Most of the available data indeed refers to capped structures in which the metal kernel is protected by organic ligands.[40,41] Therefore, we decided to adopt the experimentally determined structure when available, while relying on previous ab initio calculations in the other cases. Notice that the chosen nanostructure sizes are not always the ones most stable in vacuum, which indeed are typically M_{13}, M_{19}, and M_{55} (even if there are some exceptions, such as Au_{20}).[42,43] However, given the complex nature of the system, an atomistic insight on the NCs geometries within the experimental setups is not feasible. We thus have to rely on Extended X-ray Absorption Fine Structure Spectroscopy (EXAFS) and X-ray Absorption Near-Edge Structure (XANES) measurements, whose uncertainty in the estimation of the number of the atoms owned by a nanocluster can reach up to the 20−25%.[36] Therefore, given the arbitrariness in the choice of some model structures within this interval, we accounted for the specific geometries reported in Figure 2 based on the following reasons: the sizes are compatible with the experimental data, the structures were proved to be energetically stable by previous DFT calculations, and they are constituted by even numbers of atoms, which makes them closed-shell systems and thus computationally more affordable. Moreover, we considered the specific 1:1 alloy composition to investigate the property of systems whose composition is intermediate between the pure metal clusters, in line with experimental mixed clusters having formula Au_xAg_{1-x}, x = 0.6 ± 0.1[23] (see Supporting Information for more details). We further explored a 1:4 composition for a specific case, analyzing the tetrahedral Au_4Ag_{16} nanocluster that was previously discussed in the literature.[44] In such a structure indeed, there are no Au−Au covalent bonds, and this gives them particular electron transfer properties, as we discuss in the Supporting Information.[44] Regarding the M_{12} case, we proceeded by selecting the most stable isomer of Ag_{12} reported in ref 45 and modified the atom nature to obtain Au_{12}. To build the 1:1 Au_6Ag_6 alloy, we adapted the Ag_{12} geometry following the spatial arrangement of the atoms presented in ref 46. Regarding M_{20}, we took the starting geometries from Nhat and Tai[47] who extensively analyzed the relative stability of several M_{20} isomers. From this work we extracted the Au_{20} and Ag_{20}-A structures as the most stable isomers obtained from their calculations. In the case of tetrahedral Au_{20}, this structure was experimentally proven to be the most stable in the gas phase.[43] In order to analyze the effect the cluster geometries can have on the PL rate, we studied the energy level distribution of a silver nanostructure having an Au_{20}-like tetrahedral shape. This model was named Ag_{20}-B. The $Au_{10}Ag_{10}$ nanoalloy geometry was based on the lowest energy isomer presented in ref 48. Finally, the M_{58} clusters were obtained by adapting the Au_{58} equilibrium structure presented in ref 49. All the aforementioned NCs are pictured in Figure 2. We also considered the presence of matrix defects. To keep the model as simple as possible, we modeled this defect using an $H_3SiO_4^-$ anion that was placed at 3.5 Å from the NC and was left free to move during the geometry optimization. To explore how sensitive our nanosystems are to the defects, we placed the anion in two different orientations, one with the unsaturated Si−O bond pointing toward a NC face and one with the unsaturated Si−O bond pointing toward a NC edge, see insets of Figures 3 and 5 as examples. Finally, since some of the chosen M_{12} nanostructures do not represent the lowest energy isomer in the gas phase, which have indeed a planar structure,[42,50] we thus extended our analysis to M_{12} planar structures, investigating also the relative cluster stabilities on the basis of the cohesive energy. The results are available in the Supporting Information.

Computational Details. M_{12} and M_{20} structures were optimized using the hybrid functional B3LYP, together with the LANL2DZ relativistic corrected pseudopotentials and basis sets[51] for the metal atoms, and the 6-31+G* basis set for the atoms modeling the defect. The reliability of this computational level was previously validated in other studies on small metal-based NCs.[52−55] Because of convergency issues connected to the ab initio optimization of M_{58} systems, they were optimized using the semiempirical PM7 approach, whose accuracy in determining the geometries of metallic nanoclusters was recently tested.[56] The T_1 energy levels and the bright excitations were computed at the equilibrium geometries in a linear response TDDFT framework, using the aforementioned exchange-correlation functional and basis set. To test the capability of the PM7 technique in calculating optimized structures with proper excited state level locations, we repeated the same procedure for the smaller clusters. The results are summarized in the Supporting Information, page S7. CAM-B3LYP exchange-correlation functional was also employed to test how the calculation level can affect the geometries and the location of the T_1 levels for the M_{12} cases. Geometry optimization of T_1 excited states was performed by imposing a spin multiplicity of 3 to the ground state electronic structures. All calculations were carried out using the Gaussian 09 package.[57] UV−vis spectra convolution was performed with GaussSum03,[58] using a width at half-maximum of 0.12 eV. In all calculations, the silica matrix was accounted using the IEFPCM solvation model.[59] The static dielectric constant and the refractive index were set to 3.9 and 1.46, respectively, which are the common values used for SiO_2.[60]

■ EXPERIMENTAL METHODS

Ion Implantation and Nanoclusters Formation. Er−Ag coimplanted samples were produced by sequential ion beam implantation of Er and Ag into pure silica slabs (Herasil by Haereus). In order to obtain an almost flat concentration profile of the implanted species, a three-energy implantation scheme was adopted both for Er and Ag and the implantation energies were set in order to get the complete overlap of the

https://doi.org/10.1021/acsphotonics.0c01884
ACS Photonics 2021, 8, 1364−1376

implantation profiles in the coimplanted samples. As the first step, Er was implanted into a pristine silica slab (at 50, 100, and 190 keV) at a total fluence of 8.5×10^{14} at/cm^2 (measured by Rutherford backscattering spectrometry, RBS). An almost flat concentration profile, about 70 nm thick, centered 60 nm below the slab surface, was obtained. The Er-doped silica slab was then annealed at 800 °C for 1 h in a N_2 atmosphere to recover the implantation damage and to restore the Er−O octahedral coordination, necessary for the Er^{3+} luminescence activation. A piece of this slab was used as the reference sample (named Er800). Subsequently, Ag was implanted into the Er-doped slab (at 45, 80, and 140 keV) at a total fluence of 2.5×10^{15} at/cm^2 (measured by RBS), corresponding to an [Er]/[Ag] concentration ratio of 1/3. At last, the Er−Ag coimplanted slab was divided in two, and two sets of samples were produced by making isochronal (1 h) thermal annealing treatments at incremental temperatures in the range 300−800 °C in inert (N_2) and reducing (Ar + H_2) atmospheres. The thermal treatments are necessary to further recover the implantation damage and induce the Er^{3+} luminescence activation and to promote the formation of Ag_N clusters in the silica matrix.

Photoluminescence Measurements. Photoluminescence (PL) measurements were performed at room temperature by exciting the samples with a multiline Ar laser, mechanically chopped at 6 Hz. Different laser lines can be selected by interference filters. In this case, the 488 nm line was used to get the resonant excitation of the Er^{3+} ions in the samples (in resonance with the $^4I_{15/2} \rightarrow {}^4F_{7/2}$ Er^{3+} absorption transition). The PL emission was spectrally selected by a single-grating monochromator and detected by a N_2-cooled photomultiplier tube (Hamamatsu R5509−72) coupled with a lock-in amplifier.

RESULTS AND DISCUSSION

In this section we will present the main results coming from our calculations. We divided this section in four parts. At first we will show the results obtained for the M_{12} (M = Au, Ag, Au/Ag alloy) NCs, focusing on the analysis of T_1 energy level distributions and on the absorption features. Then we will present and discuss the data obtained for the M_{20} (M = Au, Ag, Au/Ag alloy) systems. After that, we will briefly discuss the results obtained for the M_{58} (M = Au, Ag) structures, and last, we will cover the role the excited state geometry relaxation can have on the EET process.

Since we are trying to interpret the experimental findings in a unique and coherent theoretical framework, we have to take into account the conditions in which the experiments were conducted. Most of the measurements we will refer to were conducted on Er^{3+}-doped silica glasses where the NCs were incorporated by ion implantation. Therefore, we decided to include in our calculations the effect of the SiO_2 environment through an implicit model.[59] With this approach, we were able to account for the effect of the matrix by considering our systems surrounded by a continuum, homogeneous, and isotropic dielectric material, whose dielectric constant and refractive index are the ones of pure silica.[60] Furthermore, since the ion beam can damage the structure of the dielectric matrix, we extended our calculations to systems where matrix defects are included in the form of an explicit $H_3SiO_4^-$ anion, whose dangling bond points toward the nanosystem. This anion represents the minimum defect unit with which a NC can interact and modify its EET capabilities. We will now refer to the calculations performed on the metal NC itself with the name PURE, while we will refer to the calculations that explicitly include the defect with the names FACE and TOP if the Si−O dangling bond of the anion points toward a nanocluster's face or top vertex, respectively. See the Computational Methods for more details. These two defect locations are local energy minima, but we did not characterize the global energy minimum for the defect position. In fact, we chose the TOP and FACE configurations as limit cases for the defected system (where the defect is interacting with either the least coordinated, TOP, or the most coordinated, FACE, metal atom in the cluster). As such, when both defects yield the same T_1 energy trend compared to the PURE structure, it is reasonable to assume that this trend is representative of what may happen in the defective silica matrix as well.

M_{12} (M = Au, Ag, Au/Ag Alloy). The T_1 energy level distribution of the three M_{12} structures are pictured in Figure 3, while their numerical values are reported in Table 1. From these data we can see how the silver-based NCs have the lowest T_1 levels, with their energies spreading from 0.89 to 0.99 eV in the case of PURE and TOP defected forms, respectively. On the contrary, Au_{12} have the highest T_1 levels, whose energies go from 1.17 eV (PURE case) to 1.41 eV (FACE case). The alloy presents an intermediate profile, with the T_1 energies going from 0.95 to 1.16 eV for the PURE and FACE forms, respectively. Such different behaviors arise only from the different chemical nature of the systems, since the starting coordinates adopted during the geometry optimization procedure were the same (see the Computational Methods for details). This trend suggests that gold structures not only have the most energetic T_1 levels, but also that they are more sensitive to the presence of matrix defects. Indeed, by comparing the T_1 energies of PURE and the defected forms, we recover a PURE to FACE blueshift of about 0.24, 0.07, and 0.21 eV for Au_{12}, Ag_{12}, and Au_6Ag_6, respectively; while comparing the PURE to TOP levels, we recover 0.14, 0.10, and 0.11 eV blueshifts for Au_{12}, Ag_{12}, and Au_6Ag_6, respectively. The total energy differences between the FACE and TOP isomers

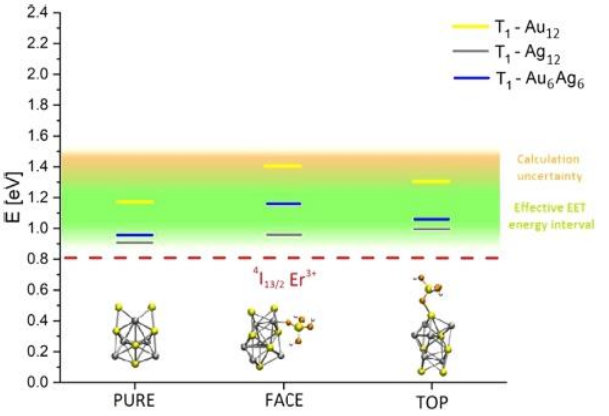

Figure 3. T_1 level distribution of the M_{12} structures. The label PURE indicates results for the bare NCs, while FACE and TOP refer to systems where the matrix defect points to a NCs face and top vertex, respectively. Red line represents the energy of $^4I_{13/2}$ Er^{3+} emitting level (0.81 eV).[61] The green band indicates the region where the EET process is more effective,[62] while the orange band extends this region, taking into account the uncertainty coming from the chosen calculation level.[63] Insets represent the optimized structures of Au_6Ag_6 aggregates.

https://doi.org/10.1021/acsphotonics.0c01884
ACS Photonics 2021, 8, 1364−1376

are very small (always lower than 0.18 eV), meaning that, in realistic conditions, there would be a comparable number of face and edge defected NCs. In this stage of the analysis we further investigated the role the atoms arrangement can have on the Au_6Ag_6 nanoalloy by swapping Au and Ag atoms both in the pure and defected structures. The swapped NCs are less stable and have more distorted geometries compared to the original; more details are available in the Supporting Information.

As mentioned, the three M_{12} structures were obtained, adapting the same starting coordinates, which are the ones presented in ref 45, for Ag_{12}. In order to explore how the aggregate geometry can affect the T_1 levels distributions, we performed the calculations on the two known most stable isomers of Au_{12} and Au_6Ag_6 NCs, which will be now called Au_{12}-B and Au_6Ag_6-B.[46,50] Those structures are profoundly different compared to the ones analyzed until this point, since they are characterized by planar geometries. Our calculations show that Au_{12}-B has its T_1 levels located at 0.75 eV, while Au_6Ag_6-B has it located at 1.02 eV. This indicates that the geometry has a prominent role in determining the electronic properties and thus EET features of the systems, which can be dramatically different considering two different isomers. In particular, Au_{12}-B T_1 level has an energy that is even lower than the Er^{3+} acceptor level, making the EET theoretically forbidden. Despite the fact that these species are the lowest-energy configurations in vacuo, as confirmed by the cohesive energy analysis reported in the Supporting Information, they may not be the most stable geometries in a silica implanted sample, since the matrix surface energy can have a pivotal role in determining the most stable NC geometries.

Because of the planar geometries, these NCs would have a larger exposed surface and would require a higher amount of free energy to be hosted by the matrix compared to the three-dimensional isomers. Considering the surface tension of pure silica[64] and the relative stabilities of the NCs, we estimated that Au_{12}-B and Au_6Ag_6-B would require extra free energy with respect to their analyzed three-dimensional counterpart of about 0.22 and 0.55 eV, respectively, making their presence less probable in the experimental samples. More details are available in the Supporting Information.

From the photophysics of lanthanide complexes, we know that there is an optimal energy difference between the antenna T_1 level and the acceptor level. This difference is strongly system-dependent and cannot be accurately determined a priori. However, there are some empirical rules that are commonly adopted to design highly luminescent antenna–lanthanide complexes. In particular, much evidence suggests that the energy difference between the donor and the acceptor levels has to be smaller than 0.43 eV (3500 cm^{-1}),[28] but greater than 0.23 eV (1850 cm^{-1}), otherwise, the back-energy transfer process would successfully compete with the direct EET.[62] Thus, considering the $^4I_{13/2}$ of Er^{3+} as the accepting (and emitting) level, whose energy in SiO_2 is about 0.81 eV (1.54 μm),[61] our optimal interval spreads from 1.04 to 1.24 eV. This interval is represented by the green band lines in Figure 3. In this fashion, it can be stated that Au_{12} and the 1:1 Au/Ag nanoalloy have the best T_1 energies, in the latter case especially when defects are accounted for. This result, however, may suffer from the uncertainty given by the B3LYP exchange-correlation functional in determining the energies of the triplet states. Indeed, despite this functional being one of the best performers in this sense, it tends to underestimate[63] the energies of the excited states of about 0.24 eV, with a mean absolute error of about 0.34 eV.[65] Such uncertainty is represented by the orange band in Figure 3. Considering this shift, the cases involving Ag_{12} NCs would now become highly performing since their T_1 falls within the EET optimal energy region and can effectively couple with the $^4I_{13/2}$ Er^{3+} state. In the theoretical framework we are testing, the incoming radiation is first absorbed by the NC antenna and then transferred to the lanthanide. In this view, the EET rate strongly depends on the population of T_1 that, in turn, is directly connected to the population of the optically active excited states. In particular, we can expect that the more the NC absorbs, the more populated would be its T_1 level and the more effective would be the EET process. Searching for a further mechanism that may explain the better sensitizer performances of Ag compared to Au, we investigated the optical absorption of the investigated M_{12} aggregates by calculating their UV–vis spectra (reported in Figure 4). No

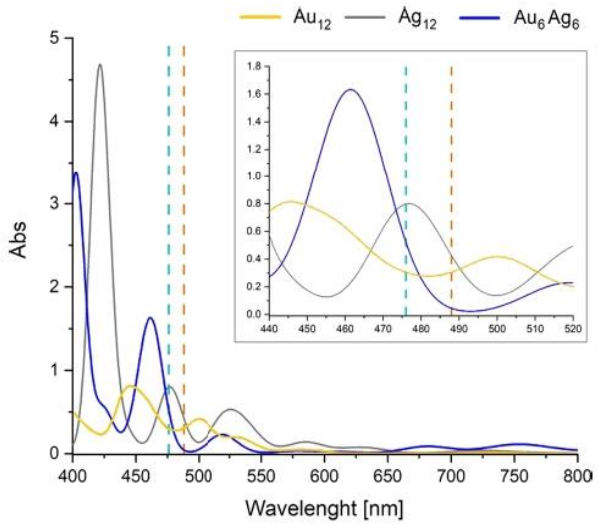

Figure 4. TDDFT-computed absorption spectra for the investigated M_{12} NCs. The inset shows a zoom over the 440–520 nm region. Light-blue and orange dashed lines represent the out-of-resonance (476 nm) and in-resonance (488 nm) wavelengths, respectively, which are commonly adopted to excite the systems in the experimental setups.[19,22−26]

relative normalization was performed in order to highlight the differences in terms of absorption intensities. We want to focus our comparison to the wavelength at which experimental measurements were done. The available experimental data recovered on Er^{3+}-doped glasses were obtained with two main exciting wavelengths: the in-resonance λ = 488 nm (resonant with the $^4I_{15/2} \rightarrow {}^4F_{7/2}$ Er^{3+} transition) and the out-of-resonance λ = 476 nm radiations.[19,22−26] We thus focus our analysis in this specific wavelengths interval, highlighted by the dashed orange and the light-blue lines in Figure 4. By looking at the energy interval of interest (around 476 and 488 nm), we can see how Ag_{12} presents a very intense peak, with its maximum located at 478 nm. Gold NCs seem to absorb less and more uniformly in this region, while the nanoalloy is active at lower wavelengths. The role of matrix defects was studied on the optimized NC-$H_3SiO_4^-$ TOP geometries. The absorption tendencies are similar to the ones reported in Figure 4 but for the absorption intensities, which are here suppressed by the

https://doi.org/10.1021/acsphotonics.0c01884
ACS Photonics 2021, 8, 1364−1376

presence of charge-transfer states between the anion and the NCs. See Supporting Information for more details.

Since the $H_3SiO_4^-$ anion is a charged species, there could take place some charge transfer phenomena between the defect and the NCs, which could affect the excited states electronic structure.

This was confirmed by an estimation of the nanocluster's partial charges on the basis of Mulliken population analysis reported in the Supporting Information. Therefore, to explore how such charge transfer effects can modify the energy levels distribution, we performed additional calculations using the long-range corrected CAM-B3LYP functional on the M_{12} PURE and TOP cases. We applied this method both on the B3LYP and on the CAM-B3LYP optimized geometries. Despite the presence of electronic displacement among the NCs and the $H_3SiO_4^-$ anion demonstrated by the Mulliken population analysis, using such an exchange-correlation functional affects the bare and defected NCs in a similar, negligible way; T_1 blueshifts by 0.03 eV (PURE Au_{12} case) to 0.11 eV (TOP Au_6Ag_6 case). These results are reported in the Supporting Information. To summarize, we found that, among the M_{12} systems, the Au_{12} and the Au/Ag nanoalloy have the best T_1 to $^4I_{13/2}$ Er^{3+} energy match. However, when the B3LYP underestimation of T_1 levels is taken into account, Ag_{12} resulted in the best performing system in this sense. Moreover, Ag_{12} presents the highest absorption intensity in the excitation window of interest, followed by the gold-based system and the nanoalloy.

M_{20} (M = Au, Ag, Au/Ag Alloy). The T_1 energy level distribution of the analyzed M_{20} structures is reported in Figure 5. All energies are reported in Table 1. In all the cases, Ag_{20}-A

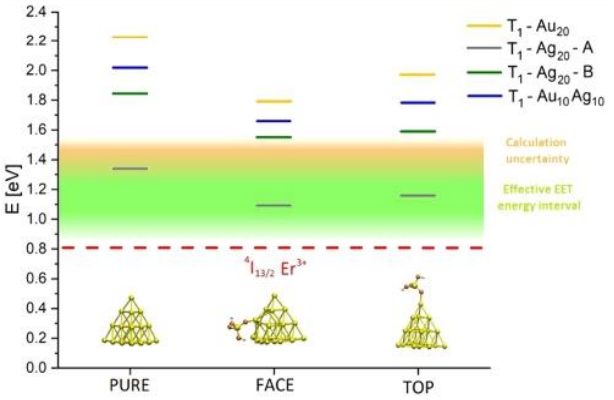

Figure 5. T_1 level distribution of the M_{20} structures. The label PURE indicates results for the bare NCs, while FACE and TOP refer to systems where the matrix defect points to a NCs face and top vertex, respectively. Red line represents the energy of the $^4I_{13/2}$ Er^{3+} emitting level (0.81 eV).[61] The green band indicates the region where the EET process is more effective,[62] while the orange band extends this region, taking into account the uncertainty coming from the chosen calculation level.[63] Inset pics represent the optimized structures of Au_{20} aggregates.

(which is the most stable form of Ag_{20} structures[47]) presents the lowest T_1 levels. These levels span from 1.09 eV in the case of FACE defect, to 1.33 eV in the case of PURE cluster. The tetrahedral Au_{20} system shows the highest T_1 levels, with energies going from 1.76 eV (FACE case) to 2.23 eV (PURE case). The other two nanostructures behave in a mixed way, as expected. It is indeed reasonable (but not trivial) to expect that the Au/Ag alloy and the Ag_{20} NC with a gold-like tetrahedral geometry (Ag_{20}-B) would have combined Au_{20}/Ag_{20}-A electronic properties. This indicates that, beyond the chemical nature, the geometry of the aggregates has a prominent role in determining the energy levels distribution and thus the EET capabilities (the Ag_{20}-B T_1 levels are more energetic compared to Ag_{20}-A of 0.43 to 0.52 eV). However, not all possible geometries are equiprobable. We recovered that the Ag_{20}-B form is less stable than Ag_{20}-A of about 0.69 eV, indicating that in realistic conditions there would be a higher amount of Ag_{20}-A than Ag_{20}-B.

Another interesting aspect that arises from Figure 5 is related to the T_1 sensitivity toward the presence of matrix defects. If we compare the PURE and the defected cases (especially the FACE one), it is notable how here the presence of defects tends to decrease the energy of the T_1 level and that the magnitude of these downshifts is system-dependent. For example, while in Ag_{20}-A the T_1 redshift between PURE and FACE is about 0.24 eV, in Au_{20}, this value is 0.44 eV. For Ag_{20}-B, the PURE to FACE T_1 energy difference is 0.33 eV, still larger than for Ag_{20}-A. The same trend can be recovered for the PURE versus TOP defected case, where the T_1 energy differences are 0.27, 0.19, and 0.25 eV for Au_{20}, Ag_{20}-A, and Ag_{20}-B, respectively. This indicates that, in general, the T_1 levels of Ag_{20} aggregates are less sensitive to the presence of matrix defects compared to the gold-based structure. The alloy behaves in an intermediate way (PURE vs FACE redshift of 0.37 eV and PURE vs TOP redshift of 0.24 eV), even when Ag and Au atoms are swapped and when the composition is changed from a 1:1 to a 1:4 Au/Ag ratio (see Supporting Information for detailed discussions). The fact that the same downshift trend is recovered for both defected cases indicates that this tendency does not depend on the location of the defect. Considering as the optimal energy interval for the EET the one represented by the green band in Figure 5, it can be stated that Ag_{20}-A always has the best T_1 energies, especially when defects are accounted, and this remains valid even if the underestimation (assumed to be of about 0.24 eV) given by the adopted XC-functional is taken into account.[63] As in the M_{12} case, we calculated the UV−vis absorption spectra of the investigated systems and reported them in Figure 6. Within the wavelength of interest, Ag_{20}-B has the highest absorption rate, followed by the $Au_{10}Ag_{10}$ alloy. This means that these two species would have the greatest excited states population and, thus, would have more chance to transfer the excitation to the Er^{3+} ions. Ag_{20}-A and Au_{20} have similar absorption properties. Given the different features among Ag_{20}-A and Ag_{20}-B, the geometry seems to play a major role. Considering only four model NCs is not enough to assess how the absorption cross-section depends on the system nature and geometry. In fact, given the experimental methods adopted to study such systems,[19,22−26] in a real sample there would be several NC isomers whose population depends on the relative stability. Therefore, even if in these calculations gold seems a worse absorber than silver and the gold−silver alloy in the wavelength region considered, the theoretical results are not clear enough to conclude that this evidence can motivate the experimental observation of larger PL enhancement given by silver and alloyed NCs.[22−24] To assess the role of matrix defects, we performed the same calculations on the optimized NC-$H_3SiO_4^-$ TOP geometries. The absorption tendencies are similar to the ones reported in Figure 6, although here we notice a general decrease in the absorbance intensities. This is

https://doi.org/10.1021/acsphotonics.0c01884
ACS Photonics 2021, 8, 1364−1376

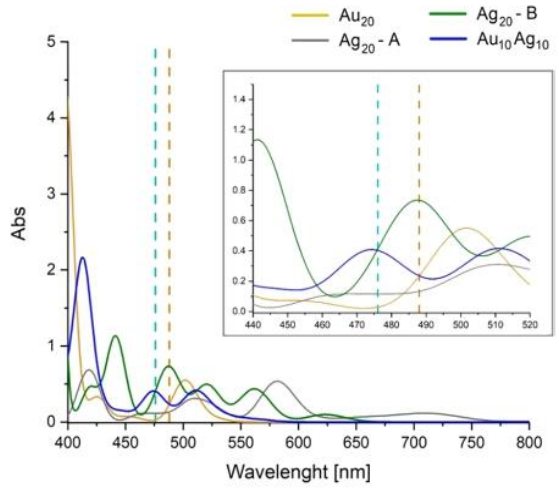

Figure 6. TDDFT-computed absorption spectra for the investigated M_{20} NCs. The inset shows a zoom over the 440−520 nm region. Light-blue and orange dashed lines represent the out-of-resonance (476 nm) and in-resonance (488 nm) wavelengths, respectively, which are commonly adopted to excite the systems in the experimental setups.[19,22−26]

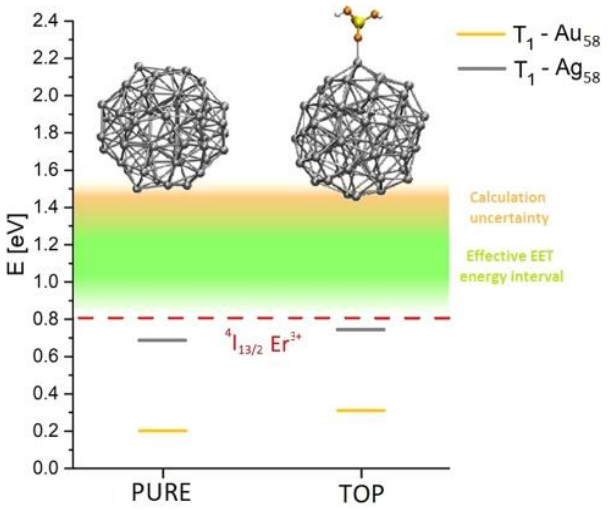

Figure 7. T_1 level distribution of the investigated M_{58} structures. The label PURE indicates results for the bare NCs, while TOP refers to a system where there is one matrix defect unit pointing toward a NCs edge. Red line represents the energy of $^4I_{13/2}$ Er^{3+} emitting level (0.81 eV).[61] The green band indicates the region where the EET process is more effective,[62] while the orange band extends this region taking into account the uncertainty coming from the chosen calculation level.[63] Inset pics represent the optimized structures of the Ag_{58} aggregates.

related to the presence of charge-transfer states between the anion and the NCs, which quench the optical absorption. More details are available in the Supporting Information.

To summarize the findings presented in this paragraph, we found that, for M_{20} aggregates, silver-based systems have the best T_1 to $^4I_{13/2}$ Er^{3+} energy match. They may also exhibit an enhancement of the absorption cross-section in the relevant excitation window. Despite the nonoptimal T_1 levels distribution, the 1:1 Au/Ag alloy presents a remarkable absorption cross-section in the spectral region of interest. Finally, the gold-based structure resulted to have the worst energy level alignment toward the Er^{3+} accepting level and to be very sensitive to the presence of matrix defects; moreover, it has no intense absorption in the investigated wavelength region. However, such findings do not account for the hydrostatic effects the matrix has toward the NCs structures. The silica environment indeed naturally compresses the NCs geometries, shortening the bond lengths and affecting the electronic structures. In most cases such compression effect reflects into a slight T_1 level blueshift (as expected from the "particle in a box" model); however, in the case of Au_{20} the T_1 energy levels can be red-shifted by tenth of eV, thus, favoring the EET mechanism. A more extensive discussion on this point is given in the Comparison with Experiments section.

M_{58} (M = Au, Ag). The third group of NCs we investigated is the M_{58} (M = Au, Ag) family. Unlike the previous cases, here we did not perform evaluations on the alloy since there are no studies that investigate the equilibrium geometry of such large alloyed structure, and anyway, there are no experimental data on such systems to compare with. The calculated T_1 levels for Au_{58} and Ag_{58} are pictured in Figure 7. Here the only defected form we could analyze is the TOP one since the spherical-like symmetry that characterizes the M_{58} does not allow to obtain a defined FACE configuration. Indeed, during the optimization procedure, the $H_3SiO_4^-$ anion naturally moves in order to generate a bond with a metal atom. As visible from Figure 7, all the calculated T_1 levels sit below the Er^{3+} emitting level and this makes the EET process forbidden. However, accounting for the possible T_1 levels underestimation given by the computational setup (see the discussion reported in the paragraph dedicated to M_{12}), the best match with the $^4I_{13/2}$ level seems to be given by the silver-based structure that presents T_1 levels at 0.69 and 0.74 eV for the PURE and TOP forms, respectively. If we consider an underestimation of about 0.24 eV, such energies increase to 0.93 and 0.98 eV, respectively, giving a nonzero probability of direct EET to the $^4I_{13/2}$ Er^{3+} level (0.81 eV), which would compete with the back-EET process. On the contrary, Au_{58} structure presents low-lying energy states whose energies are 0.20 and 0.33 eV for the PURE and TOP forms, respectively. Even accounting for errors introduced by the computational setup, these levels are too low to give an effective EET. Given the poor T_1 energy match and the complexity of the systems, we decided not to calculate the absorption spectrum of these species. Finally, we would like to remark that the computational protocol adopted in determining the M_{58} equilibrium structures was based on PM7 semiempirical algorithm rather than a DFT calculation. The minimum structures thus could be different from the DFT optimized ones and the optical properties can be affected by these structural differences. This is the case for silver and defected clusters, as we discuss in the Supporting Information. However, despite the numerical differences, the physical considerations on the lower photoluminescence enhancing capabilities still remain valid at least for the bare Au_{58} and Ag_{58} clusters.

Role of the Relaxation of the Excited States Geometry. In the previous paragraphs, we discussed the results obtained through the application of linear-response TDDFT calculations on the DFT ground state optimized structures of the various noble-metal aggregates. Thus, the data we presented refer to vertical transitions. However, the contribution the excited states geometrical relaxation can have on the relative alignment of energy levels could be pivotal in understanding the different features the NCs have in the EET mechanism. The theoretical framework we are exploring

https://doi.org/10.1021/acsphotonics.0c01884
ACS Photonics 2021, 8, 1364−1376

(the antenna−lanthanide paradigm) is based on the assumption that the EET occurs from the NCs T_1 levels to the Er^{3+} emitting level, due to the fact that triplet states are long-living states and therefore have more chance to transfer the excitation to the lanthanide. However, since these excited states can have a relatively long lifetime, their geometry can relax to the energy minimum before decaying to the ground state. In this view, the EET could take place at any time, from the moment the excited T_1 level is populated through intersystem crossing to the moment the NC reaches its T_1 excited state optimized geometry. When the EET occurs, the system relaxes instantaneously to the ground state, preserving the excited state geometrical configuration. This means that there is an energy interval in which the EET can occur, which goes from the energy of the $T_1 \rightarrow S_0$ transition calculated at the geometry of the ground state S_0, to the energy of the $T_1 \rightarrow S_0$ transition, calculated at the equilibrium geometry of the excited state T_1. We will now refer to these quantities as $\Delta E(q_{S_0})$ and $\Delta E(q_{T_1})$, where q_{S_0} and q_{T_1} indicate the equilibrium geometries of the ground state and of the first excited triplet state, respectively (see scheme in Figure 8). $\Delta E(q_{S_0})$ is exactly the

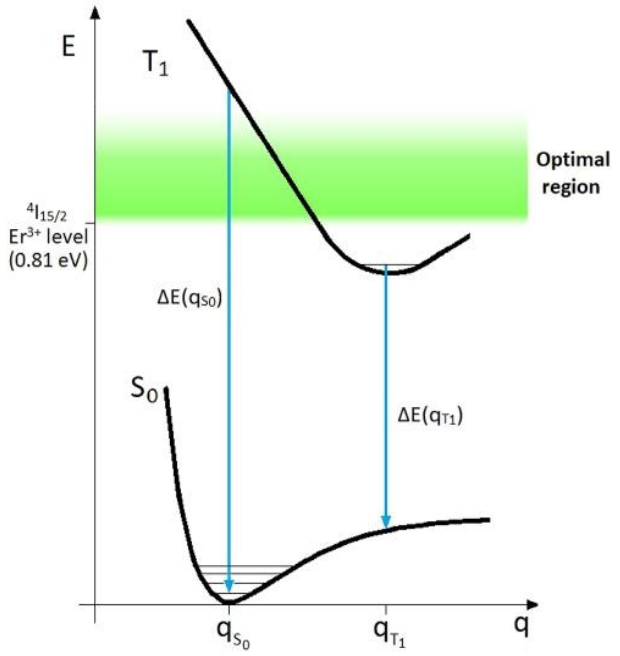

Figure 8. Qualitative representation of the T_1 and S_0 potential energy surfaces (black lines) with respect to the generic NCs geometry q. The green band represents a region where the EET process is more effective.

excitation energy that comes from the linear-response TDDFT calculations since it refers to the vertical transition computed assuming the geometry of the ground state. Then, we computed the T_1 equilibrium geometries for the M_{12} and M_{20} clusters and calculated the $\Delta E(q_{T_1})$ through a self-consistent field calculation, by imposing the proper spin multiplicity. $\Delta E(q_{S_0})$ and $\Delta E(q_{T_1})$ are collected in Table 1. We could not perform these calculations for the M_{58} cases because of the issues described in the Computational Methods.

In Table 1 we highlighted in bold the energies at which the EET could be effective, according to the criteria previously

Table 1. $\Delta E(q_{S_0})$ and $\Delta E(q_{T_1})$ for the M_{12} and M_{20} NCs[a]

cluster	geometry	$\Delta E(q_{S0})$ (eV)	$\Delta E(q_{T1})$ (eV)
Au_{12}	PURE	**1.17**	0.52
	FACE	1.41	0.26
	TOP	1.31	0.29
Ag_{12}	PURE	**0.89**	0.54
	FACE	**0.96**	0.53
	TOP	**0.99**	0.26
Au_6Ag_6	PURE	**0.95**	0.46
	FACE	**1.16**	0.37
	TOP	**1.06**	0.26
Au_{20}	PURE	2.23	0.18
	FACE	1.79	1.26
	TOP	1.96	1.32
Ag_{20}-A	PURE	1.33	**0.81**
	FACE	**1.09**	**0.83**
	TOP	**1.14**	**0.84**
Ag_{20}-B	PURE	1.85	1.37
	FACE	1.52	0.57
	TOP	1.60	0.14
$Au_{10}Ag_{10}$	PURE	2.03	0.12
	FACE	1.66	0.69
	TOP	1.79	**1.09**

[a]Bold cells indicate the configurations where ΔE can lead to an effective EET process to the $^4I_{15/2}$ Er^{3+} level. In Figure 8 we schematized the role of the involved quantities.

discussed (see the paragraph dedicated to M_{12} results). In this treatment, we omitted a precise discussion on the effect the back-EET could have on the effectiveness of the EET process since it would certainly have a minor contribution compared to the one given by the excited state relaxation. Indeed, while the back-EET just decreases the probability of having an effective direct EET from the antenna to the lanthanide, the excited state relaxation can even suppress it. The data reported in Table 1 reveal that, if accounted for, the excited state relaxation can have a prominent role in these systems. Passing from q_{S_0} to q_{T_1} the energy difference always reduces as it should, but the decrement is strongly system-dependent. In particular, it can be seen how in all M_{12} NCs cases, when the equilibrium geometry of the first triplet excited state is reached, $\Delta E(q_{T_1})$ never allows the EET since its value is smaller than the $^4I_{13/2} \rightarrow {}^4I_{15/2}$ Er^{3+} transition.

This means that with such small metal aggregates, the EET can effectively occur within a specific time frame from the moment the NCs reach its T_1 level. On the other hand, M_{20} presents different cases. Ag_{20}-A always has its $\Delta E(q_{T_1})$ in a region where the EET is possible, even if its probability is compromised by the competition of the back-EET process ($\Delta E(q_{T_1}) \approx {}^4I_{13/2}$). On the contrary, Au_{20} cluster never reaches an effective $\Delta E(q_{T_1})$ value, and thus has smaller EET rates. Considering the PURE form, its excited state energy falls way below the lanthanide accepting level ($\Delta E(q_{T_1})$ = 0.18 eV), meaning that the bare Au_{20}NC are capable to transfer its excitation only within a short time frame during the relaxation.

On the other hand, the defected forms present $\Delta E(q_{T_1})$ larger than the threshold assumed as reference for an effective EET process (1.24 eV). However, as reported in Table 1, the difference among the $\Delta E(q_{T_1})$ and this reference value is

https://doi.org/10.1021/acsphotonics.0c01884
ACS Photonics 2021, 8, 1364−1376

minute, indicating a small but non-negligible EET probability. Due to this minute difference, such probability is certainly larger than the one calculated for EET acting the unrelaxed defected NC to lanthanide. Therefore, in this case, the presence of defects can enhance the EET yield upon geometry relaxation. The other M_{20} systems mostly behave like the PURE Au_{20}, with the exceptions of PURE Ag_{20}-B, whose case is more similar to the defected Au_{20} clusters, and of TOP $Au_{10}Ag_{10}$ form, where the relaxation brings the $\Delta E(q_{T_1})$ within the interval assumed for an effective EET. Globally, this analysis revealed that the intracluster dynamics associated with excited state relaxation can have an important effect on EET probability. In particular, we notice that, on average, relaxed M_{12} systems have less probability to transfer the excitation to the lanthanide compared to the M_{20} cases, even if they start from a proper $\Delta E(q_{S_0})$ energy. This is not always true in the case of M_{20} systems where the relaxation can sometimes bring the system within the eligible T_1 to $^4I_{13/2}$ transition range or in a closer region.

We can extend such observations to the M_{58} case by accounting that excited state relaxation always decreases the $T_1 \rightarrow S_0$ energy. As shown in Figure 7, for both the M_{58} structures, the T_1 levels sit below the Er^{3+} accepting level, and thus, the starting $\Delta E(q_{S_0})$ is already inadequate to give an effective EET to the lanthanide. If we account for the triplet state relaxation, the new $\Delta E(q_{T_1})$ would be smaller and thus the EET process would be even less likely.

COMPARISON WITH EXPERIMENTS

In this section, we will discuss the experimental results obtained on the enhanced lanthanide PL, in the perspective of the antenna−lanthanide paradigm. The computational results presented so far allowed to qualitatively determine the different performances the various NCs can have with respect to the Er^{3+} sensitization. On the basis of the various discussions reported in the previous sections, we can define four major criteria that a NC should meet in order to efficiently sensitize the lanthanide ions (the higher number of criteria met, the better the efficiency is expected to be):

1. Adequate T_1 (q_{S_0}) to $^4I_{13/2}$ energy alignment.
2. During the relaxation, the $T_1(q)$ level has to cross the optimal EET region.
3. Adequate $T_1(q_{T_1})$ to $^4I_{13/2}$ energy alignment.
4. High absorption cross-section in the wavelength region of interest.

Indeed, an ideal NC antenna should have a proper T_1 to $^4I_{13/2}$ energy match in all stages of the excited states relaxation (first three criteria), as well as a high excited state population (fourth criterion). To summarize our findings, we classified in Table 2 the performance that analyzed M_{12} and M_{20} NCs have on the basis of these criteria. To ease the discussion, here we did not consider the role the back-EET can have on the process yield; we accounted for the features that affect the mere direct EET. As shown in Table 2, Ag and Au/Ag based NCs better match the criteria than the ones based on pure Au, both for the T_1 alignment and the absorbance rate. Regarding the differences among the NCs sizes, it can be noticed how the major difference resides in the T_1 energy location. If the relaxation is not accounted for, M_{12} presents the best levels alignment. However, when this effect is considered, none of the relaxed M_{12} structures are able to support the EET, while many of the M_{20} could instead. Thus, the best performing NC size cannot be easily determined a priori. However, as shown in Table 2, M_{12} systems generally match slightly better the four criteria compared to the corresponding M_{20} structures. This is particularly apparent for Au, while for Ag and the mixed clusters, M_{12} and M_{20} have globally comparable results.

Table 2. Classification of the NCs Performances with Respect to the Requirements Specified in the Main Text[a]

cluster	proper $T_1(q_{S_0}) - {}^4I_{13/2}$ alignment	T_1 relaxation cross optimal EET region	proper $T_1(q_{T_1}) - {}^4I_{13/2}$ alignment	high absorbance
Au_{12}	+	+++	−	++
Au_{20}	−	+	++*	+
Ag_{12}	+++	+++	−	+++
Ag_{20}-A	++	+++	+++	+
Ag_{20}-B	−	++	+*	+++
Au_6Ag_6	+++	+++	−	+
$Au_{10}Ag_{10}$	−	+++	+	++

[a]We give one plus symbol for each of the NCs configurations (PURE, FACE, and TOP) that satisfy the requirement. * indicates that the relaxed T_1 energy is located close to the optimal EET region upper limit (within 0.1 eV).

Before proceeding to the comparison with the experimental findings, we would like to underline that our theoretical approach is not expected to give quantitative prediction on these systems. In most of the experimental literature studies we are going to discuss, the metal ions were first incorporated by ion implantation and then, by controlling the annealing conditions, they nucleated and grew forming the NCs. Unfortunately, such complex conditions prevent an atomistic determination of the NCs sizes and geometries. For example, their characterization by Extended X-ray Absorption Fine Structure Spectroscopy (EXAFS) measurements generically assumed an average 3D compact shape. Obviously, this analysis cannot capture the high variety of geometrical configurations present in a realistic setup and return only a glimpse of the average effect this multitude of structures produce. Relying on the structural information given by EXAFS, our model NCs turn out to be representative of the mean NCs structures generated in the experiments, as shown by the geometrical comparison available in the Supporting Information. Even if such similarities do not ensure any correspondence between optoelectronic features of our model systems and the structure in the experimental system, our theoretical approach can explain many of the experimental findings and is able to predict new features on small Ag NCs which was experimentally observed for the first time. Thus, despite the limitations of our theoretical modeling, the resulting interpretation can be considered as a guide to further design effective NCs-lanthanide sensitizers.

Before starting to systematically present the comparisons, we would like to mention that we also performed an analysis aimed to investigate the effect the hydrostatic pressure of the dielectric matrix can have on the EET rates, by analyzing the T_1 energy of the various NCs when the mean bond lengths were shortened to exactly fit the experimental data. Such analysis reveals that in general, all compressed clusters' T_1 levels are slightly blue-shifted compared to the originals by a few hundredths of eV; therefore, this effect can be reasonably neglected. However, Au_{20} resulted to be more sensitive to the compression, since upon a proper rescaling of the mean bond

https://doi.org/10.1021/acsphotonics.0c01884
ACS Photonics 2021, 8, 1364−1376

length (matching the compression factor of the Au_{12} NCs), we found an energy redshift that brings the T_1 level to 1.85 eV, a value that is much closer to the optimal EET region.

Chemical Nature of the Clusters. The first point that arises from our results is that the excited states population and the optical absorption cross-section of the NCs strongly depend on the chemical nature of the system. In particular, we found that gold-based structures generally have worse levels alignments with respect to the Er^{3+} accepting level compared to Ag and the Au/Ag alloy systems. Moreover, we recall that the excited states relaxations of Ag structures preserve its ability to perform effective EET, as reported in Table 1. These effects combined can explain why in the experiments a larger PL enhancement is measured in the case of Ag and Au/Ag alloy compared to Au. As an example of these results, in Figure 1, we reported the trend as a function of the annealing temperature in a N_2 atmosphere of the Er^{3+} PL emission of three sets of Er-doped silica samples containing metallic nanoclusters of Au (orange dots), AuAg (blue dots), and Ag (red dots), incorporated by ion implantation.[19,23,35] The legend shows the ratio of the Er/metal implantation fluence. At 600 °C (where the strongest PL emission is detected, featuring clusters with N = 10−15 atoms, as revealed by EXAFS),[23,36] the Er^{3+} PL enhancement factor is about 17 for Ag, 15 for the Au/Ag alloy and 3 for the Au, as visible from Figure 1.[66] This trend agrees with the presented simulations. Considering clusters of a larger size, in ref 22, the authors reported the PL results of Er/Au coimplanted samples, for which EXAFS measurements revealed the presence of Au clusters of 25 atoms.[22,36] The maximum PL enhancement factor was 6. Such moderate enhancement can be explained considering the role the defects have in determining the electronic properties of the systems. As discussed in the Role of the Relaxation of the Excited States Geometry paragraph, Au_{20} defected systems are affected by an excited states relaxation that decreases the $T_1 \rightarrow S_0$ energy gap, bringing it into a region where the EET probability is small but non-negligible and thus increasing the whole EET rate. Notice that, in this view, matrix defects play a major role in determining the EET probability toward Er^{3+} ions.

In ref 24, the PL results of Er/Ag coimplanted samples were reported and a much stronger maximum PL enhancement factor of 25 was demonstrated. This value is even larger than the factor 17 obtained for the samples in Figure 1, in agreement with the results of the simulations presented here which indicate the Ag_{20}-A as the most effective configuration for the EET (the implantation fluency ratio adopted in Figure 1 should provide $N \approx 10-15$ atoms, while the one used in ref 24 should generate larger aggregates of $N \approx 20-25$ atoms, based on Au results). Moreover, in a work by Eichelbaum et al., it was found that the Eu^{3+} PL can be effectively enhanced by 250× when small silver aggregates are present, while in the presence of gold aggregates the enhancement factor is only about 5.[21] We remark that this large difference is also motivated by the different concentrations that could be achieved for the two metals in the silica matrix (370 ppm for Ag vs 50 ppm for gold). Yet, also taking this concentration ratio into account, silver turns out to intrinsically be a better sensitizer compared to gold, in line with our computational findings.

Size Dependence of the Enhancement. Regarding the size dependence, in the case of Au clusters, in ref 19 it was reported a detailed study of the Er^{3+} PL emission of samples implanted with Au at different fluences and thermally treated in a N_2 atmosphere, which demonstrated an increase (and a shift toward higher temperatures) in the maximum PL enhancement for decreasing Au implantation fluences and thus for a decreasing average size of the Au clusters, as measured by EXAFS.[36] This trend is consistent with our computational findings, which show a shift of the T_1 level toward the optimal band for EET going from Au_{20} to Au_{12} (see Figures 5 and 3). Moreover, this agrees with the considerations made above on Table 2. Conversely, in the case of larger clusters, it was demonstrated experimentally that for sizes in the range of 50−60 atoms the enhancement is suppressed.[22−24] Again, this is in line with the simulation results reported for the M_{58} clusters (Figure 7). It is worth underlining that the proposed mechanism may also be relevant for systems involving different lanthanides, such as the case of Dy^{3+} ions. In a work by Jiménez et al. it was noticed how the presence of silver nanoparticles with the diameter of about 2 nm can suppress the Dy^{3+} emission ($^4F_{9/2} \rightarrow {}^6H_{15/2}$ at 484 nm and the $^4F_{9/2} \rightarrow {}^6H_{13/2}$ at 574 nm transitions) as the nanoparticle concentration increases.[67] The main reason was identified to be an "ion-to-particle excitation energy transfer operating via surface plasmons in the nanoscale metal." In addition to such effect, we propose that due to the large size of the silver nanoparticles, the antenna T_1 levels are too low in energy to support an effective particle-to-ion EET. Thus, the antenna−lanthanide effect cannot take place, and the Dy^{3+} emission does not benefit from it.

Role of the Excitation Wavelength. Connected to the optical absorption cross-section of the various NCs, the computational results also provide a possible justification of why lower experimental excitation wavelengths give higher Er^{3+}PL enhancing factor.[22] As shown in Figures 4 and 6, the lower the excitation wavelength is the more intense the optical absorption peaks are. Thus, the more energetic is the incoming radiation, the higher is the NCs excited states population and the more excitations can be transferred to the lanthanide, resulting in an enhanced PL.

Effect of Annealing in a Reducing Atmosphere. Notably, the theoretical framework we are proposing allows to explain and predict the effect a reducing atmosphere annealing can have on the lanthanide PL. It was observed in ref 37 that small Au_N aggregates (N = 5−10) can increase the Er^{3+} PL more effectively when the samples are annealed in a reducing atmosphere compared to the ones annealed in an inert atmosphere.[37] We can explain this effect as follows. Reducing atmosphere can significantly decrease the number of defects in the matrix by reducing the dangling bonds of silica. Based on the computational results presented for the Au_{12} clusters, decreasing the number of defects would reduce the spread of the energy band in which the T_1 levels can be located, focusing the T_1 potential energy surface within the region where the EET to Er^{3+} is more effective (see the PURE Au_{12} system, data in Table 1). In the same way we can explain why the PL enhancement is reduced in Au_N systems (N = 20−25) when annealed in a reducing atmosphere.[22] As discussed, the presence of defects plays a beneficial role in determining the Au_{20} PL capabilities. When the sample is annealed in a reducing atmosphere, there are bonds saturations that prevent such beneficial role to take place. Finally, the same framework can be used to interpret the results of new PL measurements performed on Er−Ag coimplanted silica samples thermally treated in reducing atmosphere. In Figure 9 we report the

https://doi.org/10.1021/acsphotonics.0c01884
ACS Photonics 2021, 8, 1364−1376

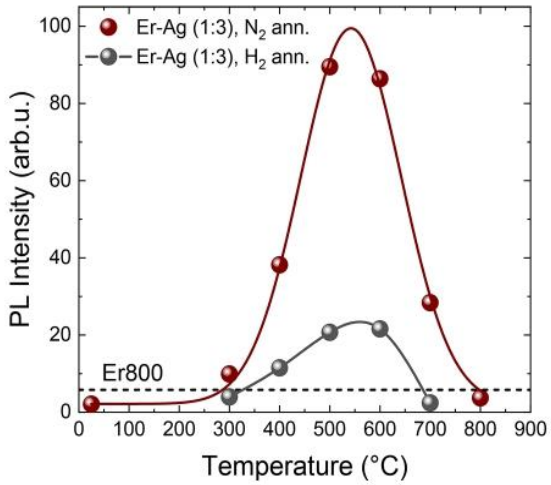

Figure 9. PL intensity at 1540 nm as a function of the annealing temperature of Er−Ag coimplanted silica samples. Red dots indicate the results of the samples annealed in inert (N_2) atmosphere. Gray dots are the results of the samples annealed in reducing (Ar + H_2) atmosphere. The solid lines are to be used as a guide for the eye. The black dashed line indicates the PL emission intensity of the reference sample (Er800). The PL measurements have been taken with resonant excitation at 488 nm.

trend, as a function of the annealing temperature, of the Er^{3+} PL emission of the samples annealed in inert atmosphere (N_2, red dots) and reducing atmosphere (Ar + H_2, gray dots). Details on the experimental conditions used to produce the samples and perform PL measurements are reported in the Experimental Methods. The implantation conditions are the same of the samples reported in Figure 1.

A maximum PL enhancement factor of 4 is obtained when the reducing atmosphere is used with respect to the factor 17 obtained for annealing in inert atmosphere. Considering the computational results shown in Figure 3 and Table 1, we can observe that, differently from the Au_{12} case, the Ag_{12} PURE system has a T_1 level located very close to the bottom edge of the effective EET energy region. Here the back-energy transfer can be highly competitive with the direct process. Thus, even the small T_1 level increase given by the defects can have a favorable impact leading to PL enhancement. In this case thus a passivation of the defects has a detrimental effect on the effectiveness of EET, decreasing the PL enhancement, as shown in Figure 9. As a final comment, it has to be noted that in principle the size of the NCs may be slightly different in the two annealing atmospheres, as evidenced in ref 22, due to the different effective diffusion coefficient of the metal atoms as a function of the annealing atmosphere. This could explain the larger sensitivity of the PL results on the passivation of the surface defects compared to what can be qualitatively predict by the calculations.

CONCLUSIONS

In this work we investigated lanthanide (Er^{3+}) sensitization by metal nanoclusters in light of the antenna−lanthanide paradigm (used so far for lanthanide sensitization by organic ligands). We thus considered the enhanced lanthanide emission as a consequence of an energy transfer process that involves the nanoclusters first excited triplet state (which is the longest living excited state) and the lanthanide-emitting level. To test this hypothesis, we studied the energy levels distribution and the absorption properties of several model nanoclusters which vary in size, geometry, and composition by means of TDDFT. In these calculations the presence of matrix defects was accounted through a simple model. We focused on silica-matrix implanted Er^{3+} ions, because of the widespread technological interest of this system and the availability of experimental data.[16,18,22−24] Given a nanostructure, we defined different aspects that can regulate the performance of the energy transfer process, namely, the level alignment with the Er^{3+} accepting level and its dependency on the excited states relaxation and the optical absorption cross-section. Our calculations suggest that the enhancement is generally more effective when the nanoclusters are composed by Ag atoms or by a mixture of Au and Ag atoms, while the worst performances were obtained by Au-based structures. Moreover, the 12 atoms structures resulted to satisfy the aforementioned criteria more effectively than larger NCs, presenting, in particular, a more adequate T_1 energy alignment. All these considerations are in line with the available experimental data. We were further able to rationalize the nonobvious effect a reducing atmosphere annealing can have on these systems. We indeed proposed that such reducing atmosphere can saturate the matrix dangling bonds, with the effect of decreasing the number of defects. In turn, defects may be detrimental or beneficial for PL, depending on the exact system considered (chemical composition and size). This can explain why reducing annealing conditions enhance the Er^{3+} emission yield when sensitized by small Au nanoclusters, while they are detrimental in the case of Ag NCs, as confirmed by novel experimental measures reported here for the first time. The same considerations applied to the case of Au_{20} revealed that the silica-matrix defects can actively take part in the EET mechanism by modifying the NCs excited states distribution, and, in some cases, are beneficial for the whole process yield. Globally, our theoretical approach was able to qualitatively rationalize the experimental findings, by using the unifying character of the antenna−lanthanide paradigm. As such, this approach can be taken as a guide to design new and more effective rare-earth ions sensitizers based on metal clusters.

ASSOCIATED CONTENT

Supporting Information

The Supporting Information is available free of charge at https://pubs.acs.org/doi/10.1021/acsphotonics.0c01884.

Energy levels distribution of swapped structures; Calculations on M_{12} structural isomers; Investigation of the Au_4Ag_{16} nanoalloy; Cohesive energy analysis; TDDFT calculations on PM7 optimized structures; Absorption spectra of defected systems; Mulliken population analysis; Results obtained with CAM-B3LYP functional; Geometrical comparison with the experimental data (PDF)

AUTHOR INFORMATION

Corresponding Authors

Stefano Corni − *Department of Chemical Sciences, University of Padova, 35131 Padova, Italy; CNR Institute of Nanoscience, 41125 Modena, Italy;* orcid.org/0000-0001-6707-108X; Email: stefano.corni@unipd.it

Tiziana Cesca − *Department of Physics and Astronomy, University of Padova, 35131 Padova, Italy;* orcid.org/0000-0002-7102-6860; Email: tiziana.cesca@unipd.it

Authors

Mirko Vanzan − *Department of Chemical Sciences, University of Padova, 35131 Padova, Italy;* orcid.org/0000-0003-3521-8045

Boris Kalinic − *Department of Physics and Astronomy, University of Padova, 35131 Padova, Italy;* orcid.org/0000-0003-1750-4929

Chiara Maurizio − *Department of Physics and Astronomy, University of Padova, 35131 Padova, Italy;* orcid.org/0000-0002-0517-1314

Giovanni Mattei − *Department of Physics and Astronomy, University of Padova, 35131 Padova, Italy*

Complete contact information is available at: https://pubs.acs.org/10.1021/acsphotonics.0c01884

Author Contributions

The manuscript was written through contributions of all authors. All authors have given approval to the final version of the manuscript.

Notes

The authors declare no competing financial interest.

■ ACKNOWLEDGMENTS

M.V. and S.C. thank MIUR-FARE for funding under the Grant Plasmochem.

■ REFERENCES

(1) Bünzli, J. C. G.; Piguet, C. Taking Advantage of Luminescent Lanthanide Ions. *Chem. Soc. Rev.* **2005**, *34* (12), 1048−1077.

(2) Eliseeva, S. V.; Bünzli, J. C. G. Lanthanide Luminescence for Functional Materials and Bio-Sciences. *Chem. Soc. Rev.* **2010**, *39* (1), 189−227.

(3) Binnemans, K. Lanthanide-Based Luminescent Hybrid Materials. *Chem. Rev.* **2009**, *109* (9), 4283−4374.

(4) Martucci, A.; De Nuntis, M.; Ribaudo, A.; Guglielmi, M.; Padovani, S.; Enrichi, F.; Mattei, G.; Mazzoldi, P.; Sada, C.; Trave, E.; Battaglin, G.; Gonella, F.; Borsella, E.; Falconieri, M.; Patrini, M.; Fick, J. Silver-Sensitized Erbium-Doped Ion-Exchanged Sol-Gel Waveguides. *Appl. Phys. A: Mater. Sci. Process.* **2005**, *80* (3), 557−563.

(5) Wang, W. C.; Zhou, B.; Xu, S. H.; Yang, Z. M.; Zhang, Q. Y. Recent Advances in Soft Optical Glass Fiber and Fiber Lasers. *Prog. Mater. Sci.* **2019**, *101*, 90−171.

(6) Qiao, J.; Zhao, J.; Liu, Q.; Xia, Z. Recent Advances in Solid-State LED Phosphors with Thermally Stable Luminescence. *J. Rare Earths* **2019**, *37* (6), 565−572.

(7) Becker, P. C.; Olsson, N. A.; Simpson, J. R. Erbium-Doped Fiber Amplifiers: Photonic Crystal Fibers. *Materials Science*; Springer, 1999, Vol. *102*, pp 203−218, DOI: 10.1007/978-1-4020-6326-8_6.

(8) Saglamyurek, E.; Jin, J.; Verma, V. B.; Shaw, M. D.; Marsili, F.; Nam, S. W.; Oblak, D.; Tittel, W. Quantum Storage of Entangled Telecom-Wavelength Photons in an Erbium-Doped Optical Fibre. *Nat. Photonics* **2015**, *9* (2), 83−87.

(9) Polman, A. Erbium as a Probe of Everything? *Phys. B* **2001**, *300*, 78−90.

(10) Snoeks, E.; Kik, P. G.; Polman, A. Concentration Quenching in Erbium Implanted Alkali Silicate Glasses. *Opt. Mater.* **1996**, *5*, 159−167.

(11) Hehlen, M. P.; Cockroft, N. J.; Gosnell, T.; Bruce, A. J. Spectroscopic Properties Of- and-Doped Soda-Lime Silicate and Aluminosilicate Glasses. *Phys. Rev. B: Condens. Matter Mater. Phys.* **1997**, *56* (15), 9302−9318.

(12) Strohhöfer, C.; Polman, A. Absorption and Emission Spectroscopy in Er^{3+} - Yb^{3+} Doped Aluminum Oxide Waveguides. *Opt. Mater.* **2003**, *21*, 705−712.

(13) Kik, P. G.; Brongersma, M. L.; Polman, A. Strong Exciton-Erbium Coupling in Si Nanocrystal-Doped SiO_2. *Appl. Phys. Lett.* **2000**, *76* (17), 2325−2327.

(14) Pacifici, D.; Franzò, G.; Priolo, F.; Iacona, F.; Dal Negro, L. Modeling and Perspectives of the Si Nanocrystals-Er Interaction for Optical Amplification. *Phys. Rev. B: Condens. Matter Mater. Phys.* **2003**, *67*, 245301.

(15) Michieli, N.; Kalinic, B.; Scian, C.; Cesca, T.; Mattei, G. Emission Rate Modification and Quantum Efficiency Enhancement of Er^{3+} Emitters by Near-Field Coupling with Nanohole Arrays. *ACS Photonics* **2018**, *5* (6), 2189−2199.

(16) Fares, H.; Elhouichet, H.; Gelloz, B.; Férid, M. Surface Plasmon Resonance Induced Er^{3+} Photoluminescence Enhancement in Tellurite Glass. *J. Appl. Phys.* **2015**, *117*, 193102.

(17) Trave, E.; Mattei, G.; Mazzoldi, P.; Pellegrini, G.; Scian, C.; Maurizio, C.; Battaglin, G. Sub-Nanometric Metallic Au Clusters as Efficient Er^{3+} Sensitizers in Silica. *Appl. Phys. Lett.* **2006**, *89*, 151121.

(18) Mattarelli, M.; Montagna, M.; Vishnubhatla, K.; Chiasera, A.; Ferrari, M.; Righini, G. C. Mechanisms of Ag to Er Energy Transfer in Silicate Glasses: A Photoluminescence Study. *Phys. Rev. B: Condens. Matter Mater. Phys.* **2007**, *75*, 125102.

(19) Cesca, T.; Kalinic, B.; Maurizio, C.; Scian, C.; Battaglin, G.; Mazzoldi, P.; Mattei, G. Interatomic Coupling of Au Molecular Clusters and Er^{3+} Ions in Silica. *ACS Photonics* **2015**, *2*, 96−104.

(20) Cesca, T.; Maurizio, C.; Kalinic, B.; Perotto, G.; Mazzoldi, P.; Trave, E.; Battaglin, G.; Mattei, G. Implantation Damage Effects on the Er^{3+} Luminescence in Silica. *Opt. Express* **2012**, *20* (15), 16639.

(21) Eichelbaum, M.; Rademann, K. Plasmonic Enhancement or Energy Transfer? On the Luminescence of Gold-, Silver-, and Lanthanide-Doped Silicate Glasses and Its Potential for Light-Emitting Devices. *Adv. Funct. Mater.* **2009**, *19* (13), 2045−2052.

(22) Maurizio, C.; Trave, E.; Perotto, G.; Bello, V.; Pasqualini, D.; Mazzoldi, P.; Battaglin, G.; Cesca, T.; Scian, C.; Mattei, G. Enhancement of the Er^{3+} Luminescence in Er-Doped Silica by Few-Atom Metal Aggregates. *Phys. Rev. B: Condens. Matter Mater. Phys.* **2011**, *83*, 195430.

(23) Cesca, T.; Kalinic, B.; Michieli, N.; Maurizio, C.; Trapananti, A.; Scian, C.; Battaglin, G.; Mazzoldi, P.; Mattei, G. Au-Ag Nanoalloy Molecule-like Clusters for Enhanced Quantum Efficiency Emission of Er^{3+} Ions in Silica. *Phys. Chem. Chem. Phys.* **2015**, *17* (42), 28262−28269.

(24) Trave, E.; Back, M.; Cattaruzza, E.; Gonella, F.; Enrichi, F.; Cesca, T.; Kalinic, B.; Scian, C.; Bello, V.; Maurizio, C.; Mattei, G. Control of Silver Clustering for Broadband Er^{3+} Luminescence Sensitization in Er and Ag Co-Implanted Silica. *J. Lumin.* **2018**, *197*, 104−111.

(25) Cesca, T.; Kalinic, B.; Michieli, N.; Maurizio, C.; Scian, C.; Devaraju, G.; Battaglin, G.; Mazzoldi, P.; Mattei, G. Energy-Transfer from Ultra-Small Au Nanoclusters to Er^{3+} Ions: A Short-Range Mechanism. *Phys. Chem. Chem. Phys.* **2014**, *16* (29), 15158−15163.

(26) Cesca, T.; Kalinic, B.; Maurizio, C.; Scian, C.; Battaglin, G.; Mazzoldi, P.; Mattei, G. Near-Infrared Room Temperature Luminescence of Few-Atom Au Aggregates in Silica: A Path for the Energy-Transfer to Er^{3+} Ions. *Nanoscale* **2014**, *6* (3), 1716−1724.

(27) Hasegawa, Y.; Kitagawa, Y.; Nakanishi, T. Effective Photosensitized, Electrosensitized, and Mechanosensitized Luminescence of Lanthanide Complexes. *NPG Asia Mater.* **2018**, *10* (4), 52−70.

(28) Bunzli, J. C. G.; Eliseeva, S. V. *Basics of Lanthanide Photophysics*; EPFL, 2010, DOI: 10.1007/4243.

(29) Kawawaki, T.; Negishi, Y.; Kawasaki, H. Photo/Electrocatalysis and Photosensitization Using Metal Nanoclusters for Green Energy and Medical Applications. *Nanoscale Adv.* **2020**, *2* (1), 17−36.

(30) The direct T_1 to $^4I_{13/2}$ EET is not the only process that can populate the Er^{3+} emitting level. There can be other competitive mechanisms (e.g., direct Er^{3+} light absorption, EET from a NC singlet excited state, etc.) that populate the higher energy states of the lanthanide that further relax to the emitting level. However, since T_1 is the longest-living antenna excited state, EET would mainly start from this level.[28] Thus, to rationalize the EET process, it is reasonable to

start analyzing the energy of NCs T_1 state with respect to the $^4I_{13/2}$ Er^{3+} emitting level.

(31) Velázquez, J. J.; Tikhomirov, V. K.; Chibotaru, L. F.; Cuong, N. T.; Kuznetsov, A. S.; Rodríguez, V. D.; Nguyen, M. T.; Moshchalkov, V. V. Energy Level Diagram and Kinetics of Luminescence of Ag Nanoclusters Dispersed in a Glass Host. *Opt. Express* **2012**, *20* (12), 13582−13591.

(32) Kuznetsov, A. S.; Velázquez, J. J.; Tikhomirov, V. K.; Mendez-Ramos, J.; Moshchalkov, V. V. Quantum Yield of Luminescence of Ag Nanoclusters Dispersed within Transparent Bulk Glass vs. Glass Composition and Temperature. *Appl. Phys. Lett.* **2012**, *101*, 251106.

(33) Cuong, N. T.; Tikhomirov, V. K.; Chibotaru, L. F.; Stesmans, A.; Rodríguez, V. D.; Nguyen, M. T.; Moshchalkov, V. V. Experiment and Theoretical Modeling of the Luminescence of Silver Nanoclusters Dispersed in Oxyfluoride Glass. *J. Chem. Phys.* **2012**, *136*, 174108.

(34) Marian, C. M. Spin-Orbit Coupling and Intersystem Crossing in Molecules. *Comput. Mol. Sci.* **2012**, *2*, 187−203.

(35) Kalinic, B.; Cesca, T.; Scian, C.; Michieli, N.; Balasa, I. G.; Trave, E.; Mattei, G. Emission Efficiency Enhancement of Er^{3+} Ions in Silica by Near-Field Coupling With Plasmonic and Pre-Plasmonic Nanostructures. *Phys. Status Solidi A* **2018**, *215*, 1700437.

(36) Maurizio, C.; Cesca, T.; Perotto, G.; Kalinic, B.; Michieli, N.; Scian, C.; Joly, Y.; Battaglin, G.; Mazzoldi, P.; Mattei, G. Core-Shell-like Au Sub-Nanometer Clusters in Er-Implanted Silica. *Nanoscale* **2015**, *7* (19), 8968−8977.

(37) Cesca, T.; Kalinic, B.; Maurizio, C.; Michieli, N.; Scian, C.; Mattei, G. Amplified Sensitization of Er^{3+}Luminescence in Silica by AuNquantum Clusters upon Annealing in a Reducing Atmosphere. *RSC Adv.* **2016**, *6* (101), 99376−99384.

(38) Kang, X.; Li, Y.; Zhu, M.; Jin, R. Atomically Precise Alloy Nanoclusters: Syntheses, Structures, and Properties. *Chem. Soc. Rev.* **2020**, *49* (17), 6443−6514.

(39) Jin, R. Atomically Precise Metal Nanoclusters: Stable Sizes and Optical Properties. *Nanoscale* **2015**, *7* (5), 1549−1565.

(40) Lu, Y.; Chen, W. Sub-Nanometre Sized Metal Clusters: From Synthetic Challenges to the Unique Property Discoveries. *Chem. Soc. Rev.* **2012**, *41* (9), 3594−3623.

(41) Chakraborty, I.; Pradeep, T. Atomically Precise Clusters of Noble Metals: Emerging Link between Atoms and Nanoparticles. *Chem. Rev.* **2017**, *117* (12), 8208−8271.

(42) Baletto, F. Structural Properties of Sub-Nanometer Metallic Clusters. *J. Phys.: Condens. Matter* **2019**, *31*, 113001.

(43) Li, J.; Li, X.; Zhai, H. J.; Wang, L. S. Au_{20}: A Tetrahedral Cluster. *Science* **2003**, *299* (5608), 864−867.

(44) Baletto, F.; Ferrando, R. Doped Golden Fullerene Cages. *Phys. Chem. Chem. Phys.* **2015**, *17* (42), 28256−28261.

(45) McKee, M. L.; Samokhvalov, A. Density Functional Study of Neutral and Charged Silver Clusters Ag_n with n = 2−22. Evolution of Properties and Structure. *J. Phys. Chem. A* **2017**, *121* (26), 5018−5028.

(46) Hong, L.; Wang, H.; Cheng, J.; Huang, X.; Sai, L.; Zhao, J. Atomic Structures and Electronic Properties of Small Au-Ag Binary Clusters: Effects of Size and Composition. *Comput. Theor. Chem.* **2012**, *993*, 36−44.

(47) Nhat, P. V.; Tai, T. B. Electronic Structure of Coinage Metal Clusters M_{20} (M = Cu, Ag, Au) from Density Functional Calculations and the Phenomenological Shell Model. *Chem. Phys. Lett.* **2018**, *706*, 127−132.

(48) Takenaka, M.; Hashimoto, Y.; Iwasa, T.; Taketsugu, T.; Seniutinas, G.; Balčytis, A.; Juodkazis, S.; Nishijima, Y. First Principles Calculations Toward Understanding SERS of 2,2′-Bipyridyl Adsorbed on Au, Ag, and Au-Ag Nanoalloy. *J. Comput. Chem.* **2019**, *40* (8), 925−932.

(49) Ouyang, R.; Xie, Y.; Jiang, D. E. Global Minimization of Gold Clusters by Combining Neural Network Potentials and the Basin-Hopping Method. *Nanoscale* **2015**, *7* (36), 14817−14821.

(50) Chaves, A. S.; Piotrowski, M. J.; Da Silva, J. L. F. Evolution of the Structural, Energetic, and Electronic Properties of the 3d, 4d, and 5d Transition-Metal Clusters (30 TM_n Systems for n = 2−15): A Density Functional Theory Investigation. *Phys. Chem. Chem. Phys.* **2017**, *19* (23), 15484−15502.

(51) Hay, P. J.; Wadt, W. R. Ab Initio Effective Core Potentials for Molecular Calculations. Potentials for the Transition Metal Atoms Sc to Hg. *J. Chem. Phys.* **1985**, *82* (1), 270−283.

(52) Lugo, G.; Schwanen, V.; Fresch, B.; Remacle, F. Charge Redistribution Effects on the UV-Vis Spectra of Small Ligated Gold Clusters: A Computational Study. *J. Phys. Chem. C* **2015**, *119* (20), 10969−10980.

(53) Azarias, C.; Adamo, C.; Perrier, A. Modeling the Photosensitizing Properties of Thiolate-Protected Gold Nanoclusters. *Phys. Chem. Chem. Phys.* **2016**, *18* (11), 7737−7750.

(54) Agrachev, M.; Antonello, S.; Dainese, T.; Gascón, J. A.; Pan, F.; Rissanen, K.; Ruzzi, M.; Venzo, A.; Zoleo, A.; Maran, F. A Magnetic Look into the Protecting Layer of Au_{25} Clusters. *Chem. Sci.* **2016**, *7*, 6910−6918.

(55) Vanzan, M.; Corni, S. Role of Organic Ligands Orientation on the Geometrical and Optical Properties of $Au_{25}(SCH_3)_{18}^0$. *J. Phys. Chem. A* **2018**, *122* (34), 6864−6872.

(56) Mato, J.; Guidez, E. B. Accuracy of the PM6 and PM7 Methods on Bare and Thiolate-Protected Gold Nanoclusters. *J. Phys. Chem. A* **2020**, *124* (13), 2601−2615.

(57) Frisch, M. J.; Trucks, G. W.; Schlegel, H. B.; Scuseria, G. E.; Robb, M. A.; Cheeseman, J. R.; Scalmani, G.; Barone, V.; Petersson, G. A.; Nakatsuji, H.; Li, X.; Caricato, M.; Marenich, A.; Bloino, J.; Janesko, B. G.; Gomperts, R.; Mennucci, B.; Hratchian, H. P.; Ortiz, J. V.; Izma, A. F.; Fox, D. J., et al. *Gaussian 09*, Revision B.01; Gaussian, Inc: Wallingford, CT, 2010.

(58) O'Boyle, N. M.; Tenderholt, A. L.; Langner, K. M. Cclib: A Library for Package-Independent Computational Chemistry Algorithms. *J. Comput. Chem.* **2008**, *29*, 839−845.

(59) Tomasi, J.; Mennucci, B.; Cammi, R. Quantum Mechanical Continuum Solvation Models. *Chem. Rev.* **2005**, *105* (8), 2999−3093.

(60) Lide, D. R.; Haynes, W. M. M.; Baysinger, G.; Berger, L. I.; Kehiaian, H. V.; Roth, D. L.; Zwillinger, D.; Frenkel, M.; Goldberg, R. N. *CRC Handbook of Chemistry and Physics*; CRC Press, 2010.

(61) Polman, A. Erbium Implanted Thin Film Photonic Materials. *J. Appl. Phys.* **1997**, *82* (1), 1−39.

(62) Latva, M.; Takalo, H.; Mukkala, V. M.; Matachescu, C.; Rodríguez-Ubis, J. C.; Kankare, J. Correlation between the Lowest Triplet State Energy Level of the Ligand and Lanthanide(III) Luminescence Quantum Yield. *J. Lumin.* **1997**, *75* (2), 149−169.

(63) Leang, S. S.; Zahariev, F.; Gordon, M. S. Benchmarking the Performance of Time-Dependent Density Functional Methods. *J. Chem. Phys.* **2012**, *136*, 104101.

(64) Boyd, K.; Ebendorff-Heidepriem, H.; Monro, T. M.; Munch, J. Surface Tension and Viscosity Measurement of Optical Glasses Using a Scanning CO_2 Laser. *Opt. Mater. Express* **2012**, *2* (8), 1101−1110.

(65) Such estimations were obtained through calculations performed on a wide set of organic molecules whose chemical nature is different compared to the present metal NCs. However, as far as we know, an extensive TDDFT benchmark study on the excited state properties of metal-based nanostructures is lacking to date, and using the existing benchmark is the best option.

(66) For the Ag case, preliminary EXAFS measurements give n = 8 atoms and a distance d_{Ag-Ag} = 2.73 Å.

(67) Jiménez, J. A. Influence of Ag Nanoparticles on the Luminescence Dynamics of Dy^{3+} Ions in Glass: The "Plasmonic Diluent" Effect. *Phys. Chem. Chem. Phys.* **2013**, *15* (40), 17587−17594.

https://doi.org/10.1021/acsphotonics.0c01884
ACS Photonics 2021, 8, 1364−1376

Supporting Information

Lanthanide ions sensitization by small noble metal nanoclusters

Mirko Vanzan,[†] Tiziana Cesca,[‡,*] Boris Kalinic, [‡] Chiara Maurizio, [‡] Giovanni Mattei[‡] and Stefano Corni[†,¶,*]

[†]Department of Chemical Sciences, University of Padova, Via Marzolo 1, 35131 Padova, Italy.
[‡]Department of Physics and Astronomy, University of Padova, Via Marzolo 8, 35131 Padova, Italy.
[¶] CNR Institute of Nanoscience, via Campi 213/A, 41125, Modena, Italy
* Emails: tiziana.cesca@unipd.it; stefano.corni@unipd.it

Calculations on swapped nanoalloys

In order to explore how the atoms disposition can affect the properties of the analysed nanoalloys, we computed the energy level distributions of Au_6Ag_6 and $Au_{10}Ag_{10}$ and nanoclusters, optimized with a swapped atoms arrangement. Obviously, these analyses cannot assure that the adopted nanostructures are the ones present in the experimental systems, even because in the experimental samples there are plenty of different structures. However, through these calculations we can estimate how much the atoms rearrangement can affect the T_1 levels distribution. As visible from Figures S1 and S2, the new distributions (green lines) differ from the ones reported in the main text (blue lines) of about 0.2-0.5 eV. Thus, the atoms disposition can heavily influence the EET performance of the structures. Focusing on the Au_6Ag_6 system, the new levels have a higher energy and are thus more adapt to support an effective energy transfer to the lanthanide. This means that in this case the presence of nanoalloys isomers can enhance the EET yield and thus increase the Er^{3+} photoluminescence intensity. Regarding $Au_{10}Ag_{10}$, the observation reported in the main text still remain valid since T_1 levels continue to be located between the gold and silver cases. All these considerations have to be rationalized by taking into account that in both cases the swapped structures resulted to be less stable than the original ones, as indicated by the positive free energy differences included in Figures S1 and S2. Therefore, the presence of such structures is less probable than the original ones in the experimental systems.

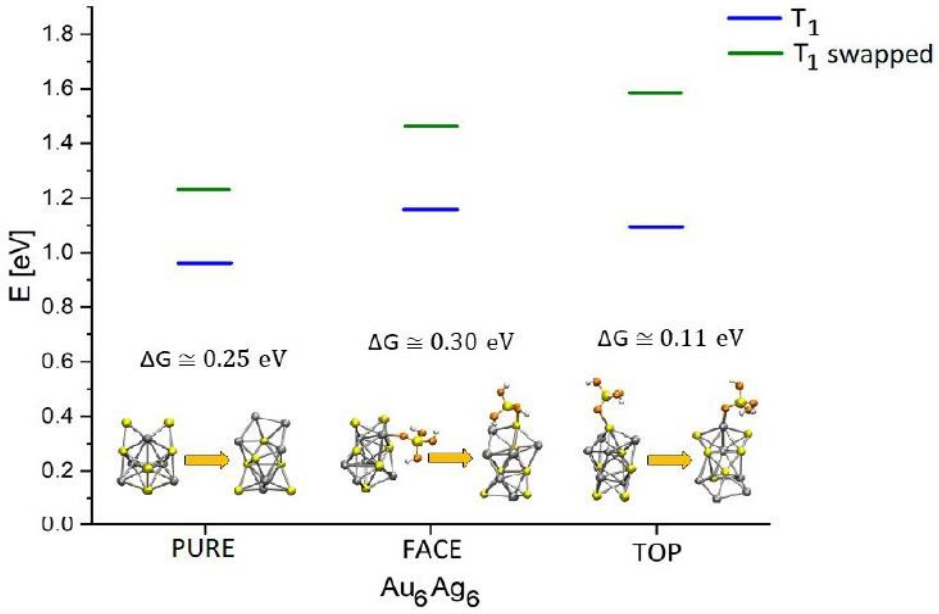

Figure S1. T_1 level distribution of the Au_6Ag_6 original (blue lines) and swapped (green lines) structures. The label PURE indicates results for the naked NCs, while FACE and TOP refer to systems where the matrix defect points to a NCs face and edge respectively. ΔG indicates the free energy differences between swapped and original structures. Insets pics represent the optimized structures of the aggregates.

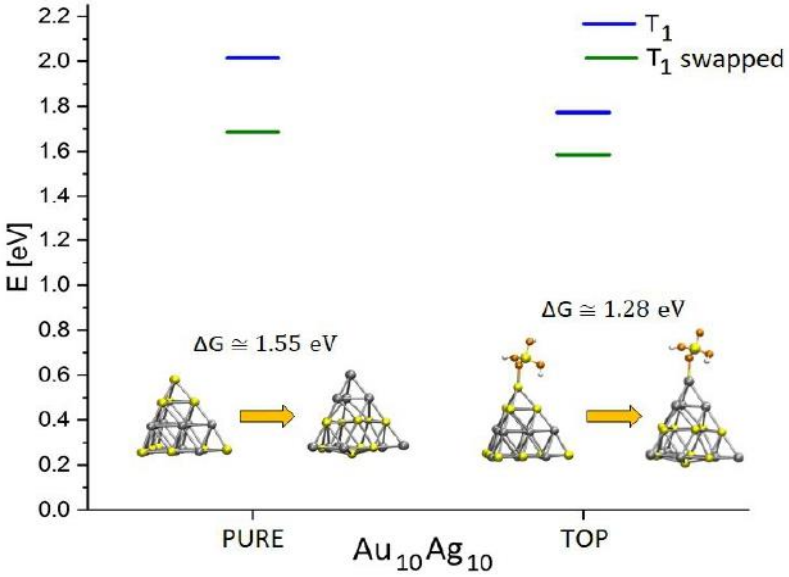

Figure S2. T_1 level distribution of the $Au_{10}Ag_{10}$ original (blue lines) and swapped (green lines) structures. The label PURE indicates results for the naked NCs, while TOP refers to systems where the matrix defect points to a NCs edge. ΔG indicates the free energy difference between swapped and original structures. Insets pics represent the optimized structures of the aggregates.

Energy level distribution of planar M_{12} nanoclusters

As mentioned in the main text, the analyzed Au_{12} and Au_6Ag_6 structures are not the most stable NCs isomers in vacuo. Indeed, some recent studies highlighted how the stable structures of these systems in vacuo have planar geometries[1,2] and this is further confirmed by our cohesive energy analysis (see next paragraph). However, there is no guarantee these structures are the most stable NCs isomers in silica as well. This because, in spite of their intrinsic stability, these planar configurations have got a larger surface area and thus, would require a higher free energy cost to be hosted in the matrix compared to a three-dimensional system. In this view, the surface tension of the matrix can have major effects in determining the most stable geometries. Given a surface tension for pure silica[3] of about 0.3 N/m, we recovered that even if the planar structures are more stable in terms of internal energy, the whole free energy balance suggests a lower stability than their three-dimensional counterpart. In particular, the free energy differences with respect to the three-dimensional systems are about 0.22 eV for Au_{12} and 0.55 eV for Au_6Ag_6, making the presence of the planar isomers less probable in the experimental systems.

Notwithstanding this result, we explored how much the T_1 levels distributions of the non-defected planar structures differ from the ones reported in the main text. We recovered the planar versions of Au_{12} and Au_6Ag_6 from ref.[2,4] and called them Au_{12}-B and Au_6Ag_6-B respectively. As visible from Figure S3, TDDFT calculations performed on the optimized structures revealed that Au_{12}-B T_1 level is located at 0.75 eV, while Au_6Ag_6-B has it at 1.02 eV. Both results are different compared to Au_{12} and Au_6Ag_6 T_1 levels which are placed at 1.17 eV and 0.95 eV respectively (see Table 1 of the main text). This confirms that the geometry has a prominent role in determining the electronic properties and thus EET features of the systems, which can be dramatically different considering two different isomers. In this case for example, Au_{12}-B system should not be able to give an effective EET to Er^{3+}, since its T_1 energy is located below the acceptor level.

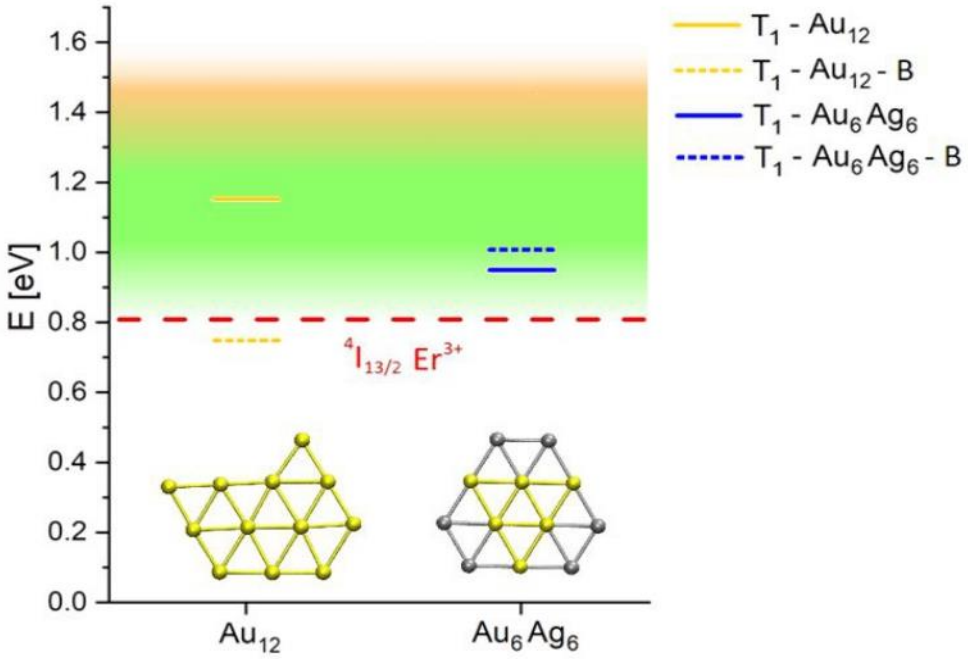

Figure S3. T_1 level distribution of the three-dimensional (full lines) and planar (dashed lines) Au_{12} and Au_6Ag_6 nanostructures. Red line represents the energy of $^4I_{13/2}$ Er^{3+} emitting level (0.81 eV).[5] Green band indicates the region where the EET process is more effective[6], while orange band extend this region taking into account the uncertainty coming from the chosen calculation level.[7] Insets pics represent the optimized structures of the planar NCs.

Investigation of the Au_4Ag_{16} nanoalloy

As mentioned in the main text, we further extended the study of the optical properties of nanoalloys by using a different metal composition. We therefore explored the Au_4Ag_{16} system, due to its interesting electronic features.[8] It was indeed proved that the lowest energy isomer of this alloy presents the gold atoms located in the vertex of a tetrahedron and this undercoordination, together with the absence of direct Au-Au bonds, give to this nanoalloy unique properties in terms of electronic structure.[8] A stick-and-ball model representation of this cluster is pictured in Figure S4. The TDDFT calculation performed on the nanocluster optimized at the B3LYP/LANL2DZ level, predicts a T_1 energy of about 1.92 eV for the bare nanocluster and of 1.62 eV for both the FACE and

TOP defected form. These results are coherent with the data coming from the other M_{20} nanosystems and locate this system right in between the Ag_{20}-B and the $Au_{10}Ag_{10}$ systems, as expected based on the Au:Ag composition. It is particularly interesting to highlight that being isolated and undercoordinated, the gold atoms tend to drain charges form the silver atoms. An estimation based on Mulliken charges analysis reveals that in Au_4Ag_{16} every gold atom has a partial charge of about -0.73 e while in $Au_{10}Ag_{10}$ this value drops to -0.42 e. This suggests this cluster could be a good candidate for further experimental investigation regarding energy and charge transfer properties.

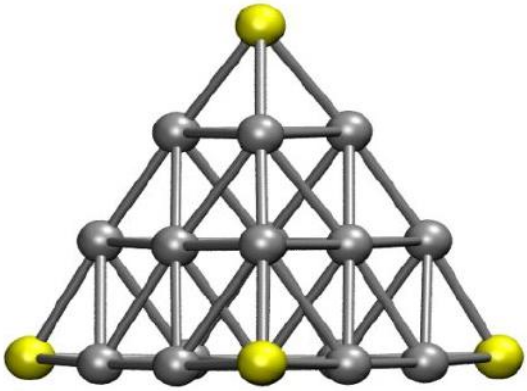

Figure S4. Graphical representation of the investigated Au_4Ag_{16} nanocluster. Au atoms are coloured in yellow and Ag in grey

Cohesive energy analysis

To properly compare the relative stability of the various nanostructures, we calculated the cohesive energies for all the bare structures investigated in this work. Such property indeed can estimate the average bond strength within a particular geometry.

Given a generic Au_nAg_m nanocluster, we define its cohesive energy as follows[9]:

$$E_{cohesive} = \frac{(n \cdot E^{Au}_{free\ atom} + m \cdot E^{Ag}_{free\ atom}) - E_{cluster}}{n+m} \qquad (S1)$$

Where n and m are the numbers of gold and silver atoms of the cluster, while $E^{Au}_{free\ atom}$ and $E^{Ag}_{free\ atom}$ are the energies of one isolated gold and silver atom, respectively. Such formula can be applied to both alloy and monometallic systems, considering the latter as a particular case where either n or m is null. We summarized the calculated cohesive energy in Table S1.

Cluster	E coh [eV]
Au_{12}	1.534
Au_{12} - B	1.579
Au_{20}	1.735
Au_{58}	2.422
Ag_{12}	1.278
Ag_{20} - A	1.423
Ag_{20} - B	1.388
Ag_{58}	1.961
$Au_{10}Ag_{10}$	1.707
Au_6Ag_6	1.512
Au_6Ag_6 - B	1.522
Au_4Ag_{16}	1.566

Table S1. Calculated cohesive energy for all investigated bare nanostructures.

As visible from these data, the larger the nanoclusters the higher the cohesive energy, as expected. Moreover, it can be seen how the energy differences between M_{12} isomers are not very large (0.045 eV at most, in the case of Au_{12}) and therefore, by including the presence of the silica environment, the stability order can easily be switched as stated in the previous paragraph.

TDDFT calculations on PM7 optimized structures

To estimate the equilibrium structure of M_{58} nanostructures, we chose to apply the semi-empirical PM7 methodology. Such approach was recently demonstrated to perform well in determining the geometries of small Au-based nanostructures.[10] To assure that such methodology properly performs even in the case of silver-based and defected systems, we calculated the optical response of our structures optimized at the PM7 level. The results are summarized in Table S2. As visible from the collected data, the PM7 optimization gives geometries whose TDDFT estimated T_1 levels are comparable with the DFT-optimized one only in the case of bare Au nanosystems, where the maximum energy difference among the two methods is -0.12 eV. When silver is considered, however, the results are sensibly different.

Cluster	T_1 opt B3LYP [eV]	T_1 opt PM7 [eV]	T_1 difference [eV]
Configuration PURE			
Au_{12}	1.17	1.06	-0.11
Ag_{12}	0.89	1.22	0.33
Au_6Ag_6	0.95	1.13	0.18
Au_{20}	2.23	2.11	-0.12
Ag_{20} - A	1.33	1.93*	0.60
Ag_{20} - B	1.85	1.93*	0.08
$Au_{10}Ag_{10}$	2.03	1.89	-0.14
Configuration TOP			
Au_{12}	1.31	0.471	-0.839
Ag_{12}	0.99	0.165	-0.825
Au_6Ag_6	1.06	0.234	-0.826
Au_{20}	1.96	–	
Ag_{20} - A	1.14	0.289	-0.851
Ag_{20} - B	1.6	–	
$Au_{10}Ag_{10}$	1.79	–	

Table S2. TDDFT calculated T_1 energy level for structures which optimized geometries were computed at the DFT-B3LYP level and at the PM7 level. Missing data ("–") mean that the algorithm could not converge to an energy minimum. * The PM7 algorithm returns the same equilibrium structures for these two nanoclusters.

In the case of Ag_{20} for example, the PM7 technique predicts the same (tetrahedral) equilibrium geometry both for clusters Ag_{20} -A and Ag_{20} -B, which is then reflected in the identical optical response of these systems. Remarkably, for silver nanostructures we notice as a general trend an overestimation of the T_1 level compared to the full ab-initio calculations. This means that the Ag_{58} T_1 level could be located at even lower energy values than what we report in the main text, and this still provides the same explanation of a reduced enhancement when such clusters are employed in experiments.

When defects are present, the predicted T_1 location is different even in the case of Au_{12}. Furthermore, most of the M_{20} defected minimum structure could not be computed since during the optimization procedure the defects are pushed far-apart from the clusters and did not reach an energy minimum. Therefore, the results obtained with such approach for clusters in the presence of defects are less solid than for bare clusters.

Absorption spectra of defected systems

As discussed in the main text, the presence of defects can significantly modify the T_1 levels distribution. We thus explored if the presence of defects can also affect the optical properties of the studied systems. To do that, we computed the absorption spectra of the optimized NCs TOP geometries, i.e. the structures where the $H_3SiO_4^-$ anion points toward a NCs edge. Qualitatively, the recovered absorption tendencies are quite similar to the ones reported in Figures 4 and 6 of the main text, although there are some minor differences that worth to be highlighted. Regarding the defected M_{12} family, comparing the spectra of Figure S5 with the ones of Figure 4, some peaks resulted to be suppressed while some others emerged (see the inset picture of Figure S5) and we notice a general absorption intensity loss.

Comparing the M_{20} spectra of Figure S6 with the ones of Figure 6, we notice how the absorption intensities are lightly suppressed when defects are taken into account, especially for NCs composed by a single species i.e., Au and Ag-based structures. The nanoalloy optical activity instead, is much more similar to the ones of reported in Figure 6, indicating that this structure is less affected by the presence of defects.

Since the NCs generally absorb less radiation in these conditions, we can state that the presence of defects would decrease the NCs excited state population and thus limit the EET yield. Further investigations revealed that these absorption losses are connected to the presence of charge-transfer states between the anion and the NCs, which decrease the whole optical activity.

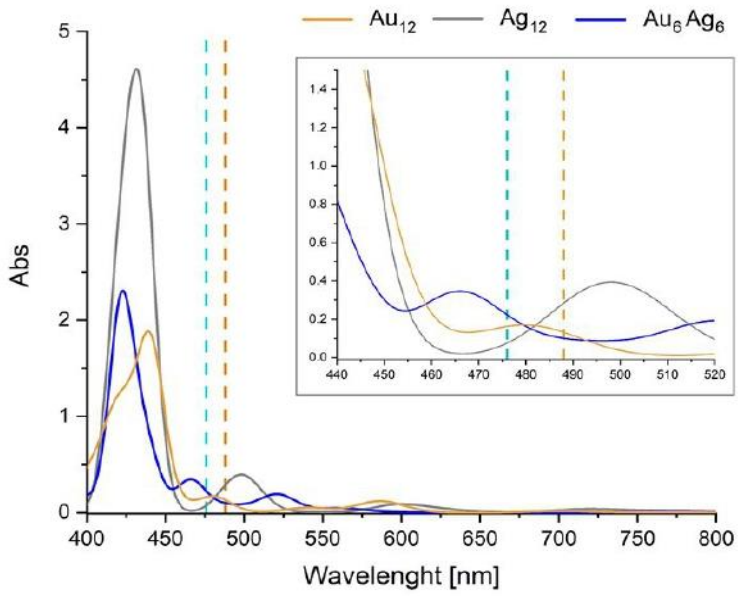

Figure S5. TDDFT-computed absorption spectra for the investigated M_{12} NCs with the defect placed on one edge. The inset shows a zoom over the 440-520 nm region. Light-blue and orange dashed lines represent the out-of-resonance (476 nm) and in-resonance (488 nm) wavelengths respectively, which are commonly adopted to excite the systems in the experimental setups.[11–15]

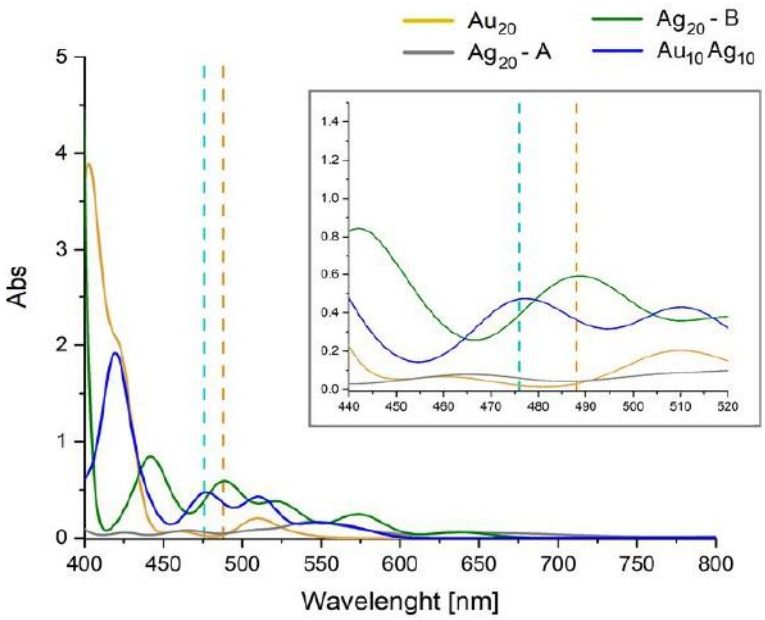

Figure S6. TDDFT-computed absorption spectra for the investigated M_{20} NCs with the defect placed on one edge. The inset shows a zoom over the 440-520 nm region. Light-blue and orange dashed lines represent the out-of-resonance (476 nm) and in-resonance (488 nm) wavelengths respectively, which are commonly adopted to excite the systems in the experimental setups.[11–15]

Mulliken population analysis

As mentioned in the main text, when we account for the presence of charged defects interacting with the metal nanoclusters, there could be the formation of net charge flow which can modify the electronic structure and the optical response of the systems. In order to quantify the magnitude of this internal charge transfer process, we calculated how much the extra charge coming from the defected anion is delocalized on the cluster by computing the Mulliken charges of the metal atoms. As visible from Table S3 there is a net charge transfer from the defect to the clusters. In particular, gold-based nanostructures tend to accumulate a higher charge than other systems. If we consider for example the case of Au_{20}, it can reach a net charge of about -0.81 e (FACE case), meaning that more than the 80% of the extra electron coming from the $H_3SiO_4^-$ defect is delocalized on the nanocluster. This is not anymore true if we consider the silver and alloy counterparts which indeed sustain smaller charges.

	Charge on nanoclusters [e]	
Cluster	**FACE**	**TOP**
Au_{12}	-0.64	-0.56
Au_{20}	-0.81	-0.44
Ag_{12}	-0.05	-0.08
Ag_{20} - A	-0.28	-0.10
Ag_{20} - B	-0.40	-0.15
Au_6Ag_6	-0.25	-0.46
$Au_{10}Ag_{10}$	-0.31	-0.34
Au_4Ag_{16}	-0.31	-0.33

Table S3. Net charges owned by the various nanostructures (in unit of e), for the FACE and TOP configurations.

Changing the functional: CAM-B3LYP results

As mentioned in the "Absorption spectra of defected systems" paragraph, we noticed that when the defects are taken into account, charge transfer states are generated, and their presence affects the optical capabilities of the structures (see the discussion on Figure S5 and S6). We thus investigated if the presence of charge-transfer states can also affect the T_1 energy levels distribution of the NCs. We analyzed the M_{12} PURE and TOP cases, using the long-range corrected CAM-B3LYP functional for the TDDFT calculations. Such exchange-correlation functional is indeed more adapt to simulate systems where charge transfer can take place. As shown in Figures S7, using this functional on the B3LYP optimized geometries (see Au_{12} – MIX, dashed line), modifies the electronic structure of naked and defected NCs in a similar way, moving the T_1 levels to higher energies. This levels blueshift goes from 0.03 eV (in the case of PURE Au_{12}) to 0.11 eV (in the case of TOP Au_6Ag_6). These changes are relatively small and do not modify the considerations reported in the main text. Regarding the CAM-B3LYP optimized geometries, TDDFT calculations predict a general redshift of the T_1 level but, even in this case, the entities of the shifts are still quite small (within 0.1 eV). Finally,

we would like to highlight that CAM-B3LYP is known to slightly overestimate the T_1 levels, which can thus be eventually more comparable to the ones recovered with B3LYP.[7] Therefore, even if possible charge transfer states are taken into account, the results on the T_1 levels distribution do not change much and thus the discussion reported in the main text still remains valid.

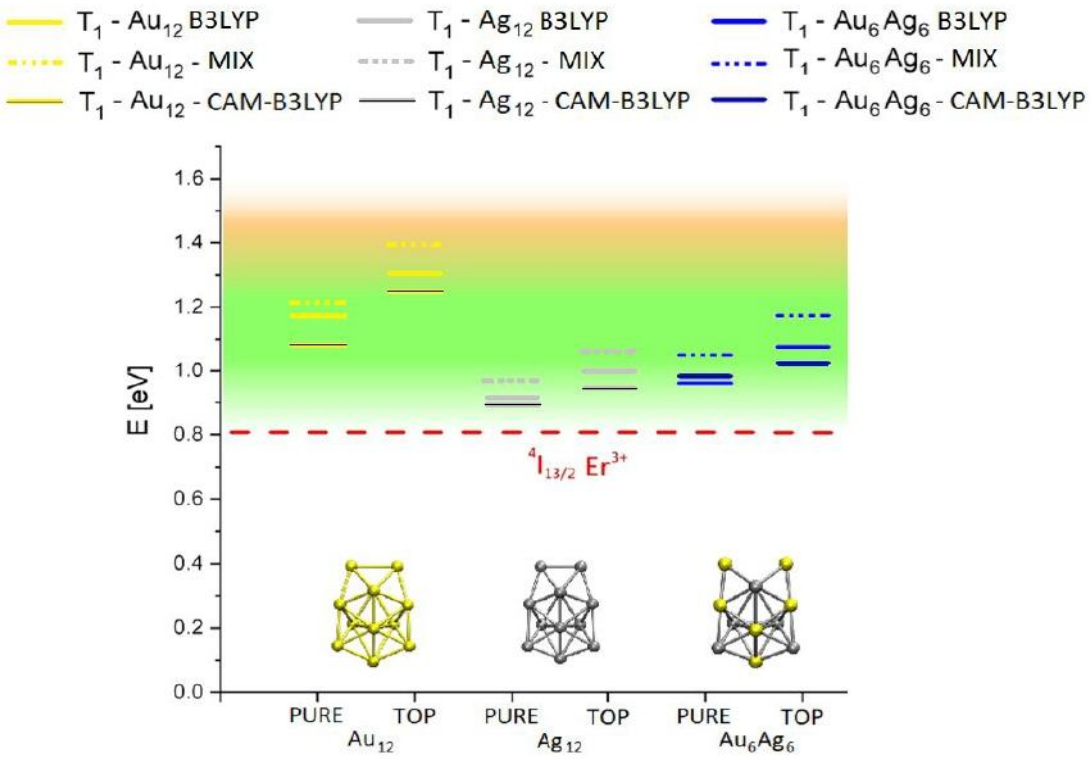

Figure S7. T_1 level distribution of the M_{12} structures, calculated at the B3LYP level on B3LYP optimized geometries (full lines), CAM-B3LYP level on B3LYP optimized geometries (named MIX, dashed lines) and CAM-B3LYP level on CAM-B3LYP optimized geometries (black striped lines). The label PURE indicates results for the naked NCs, while FACE and TOP refer to systems where the matrix defect points to a NCs face and edge respectively. Red line represents the energy of $^4I_{13/2}$ Er^{3+} emitting level (0.81 eV).[5] Green band indicates the region where the EET process is more effective[6], while orange band extends this region taking into account the uncertainty coming from the chosen calculation level.[7] Insets pics represent the optimized structures of the PURE NCs at the B3LYP level.

Geometrical parameters analysis

The high variety of cluster dimensions and stoichiometries present in realistic conditions prevent us to precisely compare our model nanostructures with the ones present in the experiments. However, at least for some NCs, there are a few experimental studies reporting mean geometrical parameters. In particular, in a few works mean bond lengths and coordination numbers are explored by Extended X-ray Absorption Fine Structure (EXAFS).[11,14] We therefore collected these data together with the data of the theoretical model counterpart and reported them in Table S4. The bond lengths analysis reveals that the simulated structures have longer bonds compared to the experimental structures. However, such overestimation is likely due to the adopted functional which usually tends to overestimate the bond length when metal atoms are accounted.[16]

Regarding the coordination number it can be seen how in the case of Au_N systems the values of the model are totally comparable with the ones recovered by EXAFS when N=10-15, while are slightly different when N=20-25. This difference can be ascribed to the high variety of conformations present in the experimental systems. Indeed, we are comparing a tetrahedral Au_{20} nanostructure with a value averaged over a multitude of Au_N (N=20-25) NCs, which is necessarily inaccurate as also confirmed by the high uncertainty associated to its value. In light of these evidences, our model and the experimental structures present comparable coordination numbers.

Regarding the nanoalloy, the coordination numbers are quite different between the model structure and the experiments, especially on the relative Ag-Ag and Au-Ag coordination numbers. This indicates that our model NC is not representative of the mean experimental structure, which instead is a 3:1 Au/Ag alloy.[14] However, considering the remarkable free energy stability compared to the analyzed isomers (see Figure S1 and S2) and considering that with our calculations we are able to fully understand the experimental findings on the Er^{3+} photoluminescence enhancement, we can

state that our model nanoalloy is representative at least for the opto-electronic properties of the experimental system, even if it does not satisfy the measured coordination numbers.

Au_N (N = 10-15)				Au_N (N = 20-25)			
Bond length *[Å]*		Coordination number		Bond length *[Å]*		Coordination number	
Calc (N=12)	*Exp [Å]*	*Calc (N=12)*	*Exp*	*Calc (N=20)*	*Exp [Å]*	*Calc*	*Exp*
2.86 ± 0.06	2.73 ± 0.02	4.7	4.2 ± 0.4	2.82 ± 0.09	2.76 ± 0.02	5.4	7.1 ± 1
Au_NAg_M (N + M = 10-15)							
Bond length *[Å]*		Coordination number					
Calc (N,M=6)	*Exp [Å]*	*Theo Au-Au*	*Exp Au-Au*	*Theo Ag-Ag*	*Exp Ag-Ag*	*Theo Au-Ag*	*Exp Au-Ag*
2.91 ± 0.08	2.75 ± 0.02	1.7	3.3±0.5	1.7	0±0.5	3.2	1.2±0.3

Table S4. Experimental and calculated mean geometrical parameters for the Au_N (N = 10-15; N = 20-25) and Au_NAg_M (N + M = 10-15) nanostructures. Experimental values obtained from ref.[11,14]

Bibliography

(1) Baletto, F. Structural Properties of Sub-Nanometer Metallic Clusters. *J. Phys. Condens. Matter* **2019**, *31*, 113001. https://doi.org/10.1088/1361-648X/aaf989.

(2) Chaves, A. S.; Piotrowski, M. J.; Da Silva, J. L. F. Evolution of the Structural, Energetic, and Electronic Properties of the 3d, 4d, and 5d Transition-Metal Clusters (30 TM_n Systems for n = 2-15): A Density Functional Theory Investigation. *Phys. Chem. Chem. Phys.* **2017**, *19* (23), 15484–15502. https://doi.org/10.1039/c7cp02240a.

(3) Boyd, K.; Ebendorff-Heidepriem, H.; Monro, T. M.; Munch, J. Surface Tension and Viscosity Measurement of Optical Glasses Using a Scanning CO_2 Laser. *Opt. Mater. Express* **2012**, *2* (8), 1101–1110. https://doi.org/10.1364/ome.2.001101.

(4) Hong, L.; Wang, H.; Cheng, J.; Huang, X.; Sai, L.; Zhao, J. Atomic Structures and Electronic Properties of Small Au-Ag Binary Clusters: Effects of Size and Composition. *Comput. Theor. Chem.* **2012**, *993*, 36–44. https://doi.org/10.1016/j.comptc.2012.05.027.

(5) Polman, A. Erbium Implanted Thin Film Photonic Materials. *J. Appl. Phys.* **1997**, *82* (1), 1–39. https://doi.org/10.1063/1.366265.

(6) Latva, M.; Takalob, H.; Mukkala, V. M.; Matachescu, C.; Rodríguez-Ubis, J. C.; Kankare, J. Correlation between the Lowest Triplet State Energy Level of the Ligand and Lanthanide(III) Luminescence Quantum Yield. *J. Lumin.* **1997**, *75* (2), 149–169. https://doi.org/10.1016/S0022-2313(97)00113-0.

(7) Leang, S. S.; Zahariev, F.; Gordon, M. S. Benchmarking the Performance of Time-Dependent Density Functional Methods. *J. Chem. Phys.* **2012**, *136*, 104101.

https://doi.org/10.1063/1.3689445.

(8) Baletto, F.; Ferrando, R. Doped Golden Fullerene Cages. *Phys. Chem. Chem. Phys.* **2015**, *17* (42), 28256–28261. https://doi.org/10.1039/c5cp01061f.

(9) McKee, M. L.; Samokhvalov, A. Density Functional Study of Neutral and Charged Silver Clusters Ag_n with n = 2-22. Evolution of Properties and Structure. *J. Phys. Chem. A* **2017**, *121* (26), 5018–5028. https://doi.org/10.1021/acs.jpca.7b03905.

(10) Mato, J.; Guidez, E. B. Accuracy of the PM6 and PM7 Methods on Bare and Thiolate-Protected Gold Nanoclusters. *J. Phys. Chem. A* **2020**, *124* (13), 2601–2615. https://doi.org/10.1021/acs.jpca.9b11474.

(11) Maurizio, C.; Trave, E.; Perotto, G.; Bello, V.; Pasqualini, D.; Mazzoldi, P.; Battaglin, G.; Cesca, T.; Scian, C.; Mattei, G. Enhancement of the Er^{3+} Luminescence in Er-Doped Silica by Few-Atom Metal Aggregates. *Phys. Rev. B* **2011**, *83*, 195430. https://doi.org/10.1103/PhysRevB.83.195430.

(12) Cesca, T.; Kalinic, B.; Maurizio, C.; Scian, C.; Battaglin, G.; Mazzoldi, P.; Mattei, G. Near-Infrared Room Temperature Luminescence of Few-Atom Au Aggregates in Silica: A Path for the Energy-Transfer to Er^{3+} Ions. *Nanoscale* **2014**, *6* (3), 1716–1724. https://doi.org/10.1039/c3nr04108e.

(13) Cesca, T.; Kalinic, B.; Michieli, N.; Maurizio, C.; Scian, C.; Devaraju, G.; Battaglin, G.; Mazzoldi, P.; Mattei, G. Energy-Transfer from Ultra-Small Au Nanoclusters to Er^{3+} Ions: A Short-Range Mechanism. *Phys. Chem. Chem. Phys.* **2014**, *16* (29), 15158–15163. https://doi.org/10.1039/c4cp01680g.

(14) Cesca, T.; Kalinic, B.; Michieli, N.; Maurizio, C.; Trapananti, A.; Scian, C.; Battaglin, G.; Mazzoldi, P.; Mattei, G. Au-Ag Nanoalloy Molecule-like Clusters for Enhanced Quantum Efficiency Emission of Er^{3+} Ions in Silica. *Phys. Chem. Chem. Phys.* **2015**, *17* (42), 28262–28269. https://doi.org/10.1039/c5cp01084e.

(15) Trave, E.; Back, M.; Cattaruzza, E.; Gonella, F.; Enrichi, F.; Cesca, T.; Kalinic, B.; Scian, C.; Bello, V.; Maurizio, C.; Mattei, G. Control of Silver Clustering for Broadband Er^{3+} Luminescence Sensitization in Er and Ag Co-Implanted Silica. *J. Lumin.* **2018**, *197*, 104–111. https://doi.org/10.1016/j.jlumin.2018.01.025.

(16) Häberlen, O. D.; Chung, S.-C.; Stener, M.; Rösch, N. From Clusters to Bulk: A Relativistic Density Functional Investigation on a Series of Gold Clusters Au_n, N=6,…,147. *J. Chem. Phys.* **1997**, *106* (12), 5189–5201. https://doi.org/10.1063/1.473518.

Chapter 2. Study of the rate-determining step of Rh catalysed CO_2 reduction: Insight on the hydrogen assisted molecular dissociation

This chapter is dedicated to analyse the dynamics and the energetics of the Rate Determining Step (RDS) of the rhodium catalysed carbon-dioxide reduction in presence of hydrogen, which was identified into the CO* conversion into CH* and O* through the formation of the CHO* species (* indicate the molecule is adsorbed on the catalyst surface). Aside from the intrinsic interest this reaction could have in the context e.g. of climate-change mitigation, CO_2 reduction resulted a notable prototype reaction to accurately investigate plasmon-driven photocatalysis, being the RDS of this reaction strongly influenced by the photophysical response of the catalyst. The work presented in this chapter aims to provide a solid ground for future investigation on plasmon-driven CO_2 reduction, exploring the Rh (100) catalysed RDS and focusing on the purely thermodynamic mechanism. This were done applying Density Functional Theory and Nudge Elastic Bands calculations on a system composed on a Rh (100) extended surface, on top of which the molecular species involved in the reaction were adsorbed and could properly interact.

The complete collection of the obtained results, as well as a critical analysis of the adopted methodologies are reported in this chapter in the form of published paper, reprinted with permission of Catalysts 2021, 11, 538. Besides contributing to the calculation design, I performed the calculations and the analysis, under the supervision of Dr. M. Marsili as well as Prof. S. Corni, and I drafted the article and wrote the responses to the reviewers comments.

Attached to the article I report the corresponding supplementary material, containing also a movie showing the precise dynamics of the Rh-catalysed CO_2 RDS. Such movie can be directly seen by scanning the QR code in the dedicated section.

catalysts

MDPI

Article

Study of the Rate-Determining Step of Rh Catalyzed CO_2 Reduction: Insight on the Hydrogen Assisted Molecular Dissociation

Mirko Vanzan [1], Margherita Marsili [1,*] and Stefano Corni [1,2,*]

[1] Department of Chemical Sciences, University of Padova, Via Marzolo 1, 35131 Padova, Italy; mirko.vanzan@phd.unipd.it
[2] Center S3, CNR Institute of Nanoscience, Via Campi 213/A, 41125 Modena, Italy
* Correspondence: margherita.marsili@unipd.it (M.M.); stefano.corni@unipd.it (S.C.); Tel.: +39-049-8275295 (S.C.)

Abstract: In the context of climate change mitigation, CO_2 methanation is an important option for the production of synthetic carbon-neutral fuels and for atmospheric CO_2 recycling. While being highly exothermic, this reaction is kinetically unfavorable, requiring a catalyst to be efficiently activated. Recently Rh nanoparticles gained attention as effective photocatalyst, but the rate-determining step of this reaction on Rh surface has not been characterized yet. In this work, Density Functional Theory and Nudged Elastic Band calculations were performed to study the Rh-catalyzed rate-determining step of the CO_2 methanation, which concerns the hydrogen assisted cleavage of the CO* molecule and subsequent formation of CH* and O* (* marks adsorbed species), passing through the CHO* key intermediate. The configurations of the various adsorbates on the Rh (100) surface were investigated and the reaction mechanism was studied exploiting different exchange-correlation functionals (PBE, RPBE) and the PBE+U technique. The methanation rate-determining step consists of two subprocesses which subsequently generate and dissociate the CHO* species. The energetics and the dynamics of such processes are extensively studied and described. Interestingly, PBE and PBE+U calculated activation barriers are in good agreement with the available experimental data, while RPBE largely overestimate the CHO* dissociation barrier.

Keywords: CO_2 reduction; CO_2 methanation; rhodium catalysts; Density Functional Theory; Nudged Elastic Band; energy landscape; energy barrier; reaction energy; rate-determining step

Citation: Vanzan, M.; Marsili, M.; Corni, S. Study of the Rate-Determining Step of Rh Catalyzed CO_2 Reduction: Insight on the Hydrogen Assisted Molecular Dissociation. *Catalysts* **2021**, *11*, 538. https://doi.org/10.3390/catal11050538

Academic Editor: C. Heath Turner

Received: 19 February 2021
Accepted: 16 April 2021
Published: 22 April 2021

1. Introduction

The last Intergovernmental Panel on Climate Change (IPCC) summary report addressed the prominent impact that human industrial activities are having on global climate conditions [1]. The enormous quantity of greenhouse gases that have been released into the atmosphere since the mid of the 20th century are causing a sharp increase in the global average temperature, with dramatic consequences on many ecosystems [1,2]. Reducing carbon emissions and mitigating the impact of climate change is thus a challenging and fundamental task. In particular, actions leading to the replacement of fossil fuels with other environmentally sustainable sources and to the decrease of CO_2 atmospheric concentration are especially needed. The effective production of synthetic carbon-neutral fuels from greenhouse gases could help addressing both these issues, making it possible at the same time to recycle atmospheric pollutants while providing a new source of fuels. In this context, CO_2 methanation represents a possible route toward the production of carbon-neutral fuels [3,4]. This process is represented by the following reaction:

$$CO_2 + 4H_2 \rightarrow CH_4 + 2H_2O \; \Delta H^0 = -165 \text{ kJ/mol (298 °K)} \quad (1)$$

The reaction enthalpy ΔH^0 value, reported in Equation (1), shows that this reaction is highly exothermic. However, the elementary steps connected to the eight-electron reduction present high kinetic barriers that make this process unfeasible without an effective catalyst [5,6]. Indeed in the last decade many efforts were spent in order to search for catalysts with high selectivity and stability, and low working temperatures [3–6]. In this context, a promising family of devices is represented by metal-based catalysts, in which an active metallic layer is deposited over a supporting material [5,7,8].

This configuration has made it possible to produce many catalysts based on transition metals (e.g., Ru, Rh, Pd, Cu, Ni, Co), resulting in them being very stable and selective, but requiring a large amount of energy to activate the methanation reaction (working temperature usually ranging between 250 and 500 °C) [3,4,6,8]. Recently, large improvements in the catalytic features of metallic devices have been achieved by exploiting the surface plasmon resonance in small metal nanoparticles [9–12]. In these works it was shown that upon activation of their plasmonic resonance, Rh-based catalysts showed almost 100% selectivity toward methane formation and extremely high production rates [10–12]. Such high catalytic performance was ascribed to the decreasing of the activation energy of the reaction rate-determining step (rds), which, on Rh surfaces is the hydrogen assisted dissociation of CO*, through the key intermediate CHO* in CH* and O* (* marks species adsorbed on the Rh surface) [10,13,14]. However, to the best of our knowledge, while the thermal process has been theoretically studied in the context of CO_2 hydrogenation on Ni, Cu, Co and Ru surfaces [13,15], in the case of Rh it has not been addressed yet.

Despite the exact reaction path for the Rh-catalyzed methanation still being debated and not fully understood [7], and that there is evidence indicating that the reaction could proceed through different pathways towards the generation of gaseous methane [6], there is a general agreement on some key steps that the reaction has to go through in order to produce methane. More precisely, in recent years, several studies have demonstrated that the first step for the Rh-catalyzed CO_2 reduction is the dissociative chemisorption of CO_2, leading to the formation of the CO* and O* species through a finite number of steps (* symbol indicates that the species is adsorbed on the catalyst surface) [6,7]. This process seems to be related to the rhodium surface itself, rather than to other factors (e.g., the supporting material), since it was observed on Rh crystals [16], foils [17,18], and on several supported systems [19–22] and was demonstrated to take place more easily on the Rh (100) surface rather than the Rh (111) one [23]. Furthermore, it seems that this step is made easier when H_2 is dissociatively adsorbed on the surface too [24,25]. Once formed, CO* can either desorb (leading to the formation of gaseous CO through the reverse water gas shift mechanism [26]) or interact with H* to generate intermediate complexes. The nature of these molecular species has not been uniquely identified, since there are many processes that can take place locally on the surface, leading to the generation of molecules like CHO*, H_2CO* or COH* [6,22]. Additionally, backward reactions with adsorbed free oxygen can occur leading to species such as $HCOO^-$*, $COOH^-$* or HCOOH* [20,27]. However, there is evidence to suggest that CHO* formation and dissociation are key processes in this reaction, and it has been suggested that the CHO* dissociation into CH* and O* through a C-O bond cleavage represents the rds of the whole methanation process [13,28–31].

In this work, we study and characterize the rds of CO_2 methanation reaction on the Rh (100) surface employing DFT and Climbing-Image Nudged Elastic Band (CI-NEB) calculations [32]. Different exchange-correlation (XC) functionals and methods (Perdew-Burke-Ernzerhof (PBE) [33], Revised Perdew-Burke-Ernzerhof (RPBE) [34] and PBE+U [35]) have been used to treat the electronic interactions, and their performances are compared. The equilibrium geometry and energetics of the clean Rh slab, adsorbed reactants, and products have been carefully investigated in the low coverage regime. From our calculations, the CHO* formation is a single-step process in which the reactive CO* and H* species diffuse and rotate on the rhodium surface, allowing the formation and relaxation of the CHO*. Instead, the CHO* dissociation seems to proceed in two main steps. In the first one, involving the largest barrier, the C–O bond is stretched and breaks, leading to the two

separated CH* and O* species. In the second step, O* diffuses on the surface reaching its equilibrium configuration, overcoming another lower energy barrier and relaxing the stress accumulated in the distortion of Rh outermost surface layer. While all methodologies and functionals agree on the general dynamics of the process, when using the RPBE functional CH* and O* stabilities are lowered by c.a. 0.35 eV with respect to PBE-based methods, and the CHO* dissociation energy barrier is greatly overestimated compared to experimental data. We relate the divergence among the methods to the different treatment of the interface region in the RPBE functional [34], which yields lower adsorption energies, a tendency that is stronger for the products than for the reactant. The paper is organized as follows: first the computational details of the work are provided, then the results of the geometry optimizations and the NEB simulations are presented and discussed, finally conclusions are drawn.

2. Results and Discussion

2.1. Clean Rh (100) Slab Characterization

To determine the geometrical structure of the catalyst and to compare the performance of the different xc functionals, the physical and geometrical features of the clean Rh (100) surface were studied. In particular, the slabs were characterized on the basis of their surface energies σ, work function φ, and surface lattice relaxation parameter d_{ij} %. These quantities were computed on the basis of the definition reported in Appendix A as Equations (A1)–(A3). The calculated data, together with theoretical and experimental results available in the literature, are collected in Table 1. Among all the available computational data, only those obtained with computational setups similar to the ones adopted in this work are reported here. As shown in Table 1, our PBE results are in good agreement with previous calculations. Differences on the absolute values of the analyzed parameters are very small and can be ascribed to the different codes used by the authors [36,37]. The difference of about 0.17 eV/atom with respect to the surface energy computed in ref. [36] can be related to the different method adopted in the surface energy calculation. Indeed, in ref. [36], the surface energy was obtained through the linear regression on the total energy of the slabs as a function of the number of layers of the slabs themselves.

Table 1. Surface relaxations $d_{1,2}$% and $d_{2,3}$%, work function φ and surface energies σ for the Rh (100) slab, relaxed with PBE and RPBE functionals, together with available theoretical and experimental literature data.

Method	$d_{1,2}$%	$d_{2,3}$%	φ	σ [eV/atom]
PBE	−4.1	0.7	5.11	1.09
RPBE	−1.6	0.3	4.97	0.96
PBE (ref. [36])	−4.1	0.5	5.12	1.26
PBEsol (ref. [36])	−3.6	0.8	5.38	1.34
PW91 (ref. [37])	−3.0	−0.1	4.91	0.99
Experiments (refs. [38–40])	-1.16 ± 1.6	0 ± 1.6	5.3 ± 0.15	1.12

Moreover, as can be seen from Table 1, PBE results agree well with experimental data apart from the relaxation of the outermost layer, which is overestimated by all the calculations, except for the RPBE one. It is worth noting that the 0.19 eV difference with the experimental work function is well within the range of the accuracy of DFT-PBE for this quantity [41]. Regarding RPBE results, all values are comparable with the other theoretical estimations, with the exception of $d_{1,2}$% , which interestingly is closer to the experimental data. This could suggest a better performance of RPBE in determining the physical properties of the Rh (100) slab. However, as mentioned in the computational details, RPBE predicts a larger (and less accurate) Rh bulk unit cell parameter. This is reflected in the larger denominator in Equation (A3) and the smaller relative surface layer relaxation. Globally, our analysis suggests that the two XC functionals give comparable results in determining the clean slab physical properties. The major difference resides in

the accuracy of determining the bulk Rh–Rh bond length which is more accurate using PBE rather than RPBE.

2.2. Description of the Adsorbates

As mentioned in Section 1, the key molecular species involved in the rds of CO_2 reduction are CO*, H*, CHO*, CH* and O*. We thus studied the equilibrium configuration of these species and the energetics of the various systems. Three possible adsorption sites, Bridge, Top and Hollow were considered. A visual representation of these sites on the Rh (100) surface is shown in Figure 1. For each adsorbate, the most stable configuration was identified, and the adsorption energies were calculated using the following expression:

$$E_{ads} = E_{slab+spec} - E_{slab} - E_{spec} \quad (2)$$

where $E_{slab+spec}$ is the total energy of the system composed on the slab and the adsorbed specie, E_{slab} is the energy of the slab itself, and E_{spec} is the energy of the free species. It is important to underline that given the 3×3 supercell dimension adopted for these calculations, our results refer to low ($\Theta = 1/9$ ML) adsorbate coverage of the surface. The adsorption energies of the investigated molecular species are collected in Table 2, while the most stable geometrical configurations of the different species, calculated at the PBE level, are shown in Figure 2.

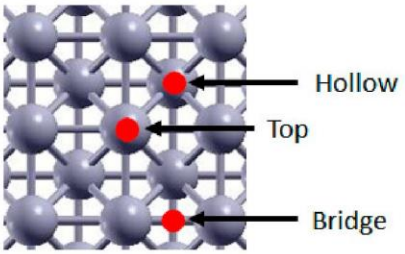

Figure 1. Rh (100) adsorption sites. Red spots indicate the site, Rh atoms are pictured in grey.

A first fundamental step of the methanation reaction is the generation of CO*. This adsorbed species has to satisfy two main requirements in order to represent a reliable intermediate for the reaction mechanisms namely thermodynamic stability and geometrical accessibility. The first requirement ensures that the molecular intermediate is more stable when adsorbed on the catalyst surface compared to the gas phase form, ensuring the stability of such species which would otherwise desorb, preventing further reaction steps. On the other hand, the geometrical accessibility is mandatory to allow interactions with co-adsorbed hydrogen atoms and thus to proceed towards the reaction products. As visible from the data collected in Table 2 and the picture in Figure 2 panel A, both these criteria are satisfied. Regardless of the calculation level, the adsorbed configurations are always more stable than the isolated systems, indicating that the adsorption of CO is an exothermic (and thus favorable) process. Moreover, within the relaxed geometry, the CO molecule is adsorbed perpendicularly to the surface, with the carbon interacting with the rhodium atoms and the oxygen pointing in the opposite direction. This suggests that the C atom can easily interact with hydrogen, because no steric hindrance is present along the directions parallel to the surface plane. From our analysis, the most stable configuration is obtained when CO is adsorbed on a Bridge site. The adsorption energies are close to the ones of the Top adsorbed geometries (maximum energy difference of about 70 meV), and this justifies the co-existence of these two configurations observed experimentally [42–44]. Despite the qualitative agreement between theory and experiments concerning the adsorption geometries, experimental values for CO adsorption energy range between $1.35 \div 1.45$ eV [43–47], while our DFT PBE calculations predict a much larger adsorption energy (ca. 2 eV), in agreement with previous theoretical results [48–51]. Indeed, despite PBE properly predicts properties like Rh bonds length and electronic

structures [52], it was shown that it overestimates the interaction among the Rh d-type orbitals and the 2π* level of CO, leading to an overestimation of the CO adsorption energy on rhodium surfaces [53,54]. To overcome this problem, on one hand, we employed the PBE+U method, which allowed us to properly shift the CO 2π* level in order to obtain more accurate results [55,56]; on the other hand, we used the RPBE functional, which was specifically designed for yielding more accurate adsorption energies compared to PBE functional [34] and has been demonstrated to give more reliable results in modeling the CO-metal interactions [52]. As shown in Table 2, the two methods yield a much better agreement with the experimental adsorption energy values. Interestingly, these results are not associated with significant geometrical changes; indeed, the computed C–O bond length for the Bridge adsorption sites are 1.17 Å and 1.18 Å for the PBE-based and RPBE calculations respectively, while the distance between C and Rh atoms resulted in be 2.02 Å and 2.07 Å for the PBE-based and RPBE calculations, respectively. All these data are coherent with previous calculations [49,51,52].

Table 2. Adsorption energies of the investigated species on the three possible adsorption sites (Bridge, Top and Hollow) of Rh (100) slab, calculated with the PBE, PBE+U and RPBE methods. Values within round parenthesis refers to the adsorption energies of the biatomic species, i.e., H_2 and O_2.

Species	Adsorption Site	Eads PBE [eV]	Eads PBE+U [eV]	Eads RPBE [eV]	Eads Experimental [eV]
CO	Bridge	−1.997	−1.413	−1.529	−1.40, ref. [43]
	Top	−1.929	−1.343	−1.483	
	Hollow	−1.864	−1.292	−1.420	
H	Bridge	−3.838 (−0.52)	−3.838 (−0.52)	−3.590 (−0.65)	(−0.52), ref. [57]
	Top	–	–	–	
	Hollow	−3.823 (−0.51)	−3.823 (−0.51)	−3.584 (−0.65)	
CHO	Bridge	−3.310	−3.394	−2.642	-
	Top	−2.991	−3.085	−2.333	
	Hollow	−3.310	−3.394	−2.642	
CH	Bridge	-	-	-	-
	Top	-	-	-	
	Hollow	−7.603	−7.582	−6.426	
O	Bridge	−6.206 (−4.29)	−6.509 (−4.45)	−5.153 (−2.41)	(−4.00), ref. [58]
	Top	-	-	-	
	Hollow	−6.325 (−4.53)	−6.647 (−4.75)	−5.370 (−3.04)	

The other reactant that must adsorb on the Rh surface is hydrogen. Previous investigations have shown that H_2 spontaneously dissociates and diffuses on the catalyst surface as soon as it is chemisorbed [57,59]. The adsorption energies reported in Table 2 indicate that the most stable adsorption sites for H* are Bridge and Hollow (the most stable geometry is shown in Figure 2 panel (B). These configurations are practically isoenergetic, as already reported in previous studies [60,61]. The energy of the Top configurations cannot be obtained since the chemisorbed H naturally falls into a Hollow site during the relaxation. The H-Rh distance is about 1.76 Å and 2.00 Å in Bridge and Hollow sites, respectively, for PBE and 1.79 Å and 2.02 Å for RPBE calculations. PBE and PBE+U results are identical as no Hubbard-U corrections to H atoms were applied.

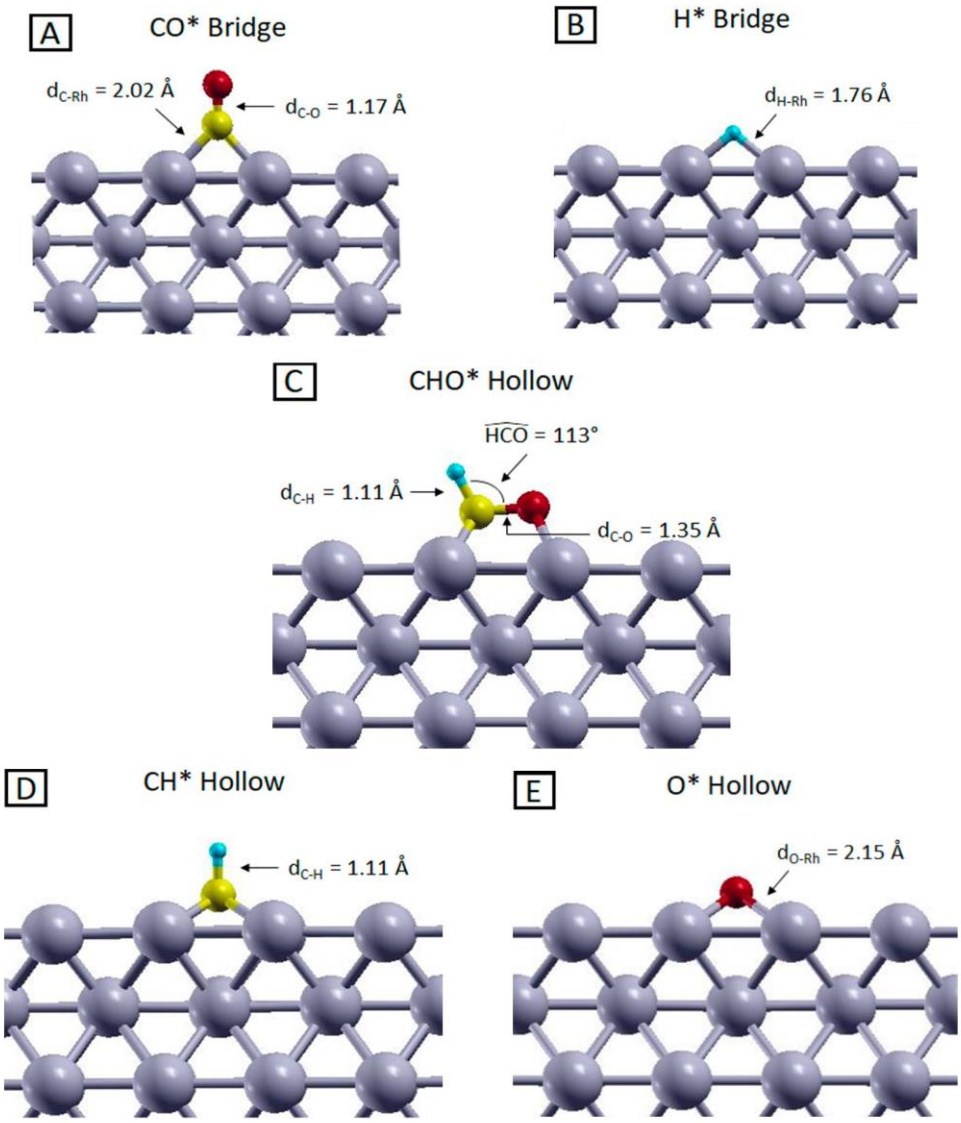

Figure 2. Side views of the most stable configurations of (**A**) CO, (**B**) H, (**C**) CHO, (**D**) CH and (**E**) O adsorbed on the Rh (100) surface, optimized at the PBE level. Yellow, red, light blue and grey represent C, O, H and Rh atoms, respectively.

Given the atomic nature of the adsorbed species, the values reported in Table 2, computed with respect to the total energy of the isolated hydrogen atom, cannot be directly compared with experimental data which refer to the H_2 dissociative chemisorption. To be able to compare directly with such experimental data and check the reliability of our results, we repeated the calculations for a slab with an H atom adsorbed on each side, this time computing the adsorption energy with respect to the total energy of the isolated H_2 molecule; the results are listed in parenthesis in Table 2. Additionally in this case, the favorite chemisorption sites are Bridge and Hollow with an adsorption energy calculated with PBE functional of about 0.52 eV, in line with what has previously been observed [57,60]. Using the RPBE functional gives an adsorption energy of about 0.65 eV, slightly larger than the PBE case, and in worse agreement with the experimental values.

The stability of the adsorbed CHO* complex, involved in the rds, compared to its gas-phase counterpart, is confirmed by the adsorption energies reported in Table 2. The most stable geometry, reported in Figure 2 panel C, was obtained starting from both Bridge and Hollow configurations, using all three computational methods. As shown in Figure 2 panel

C, the C–O bond is basically parallel to the surface, with a C–O distance, C–H bond length and an HCO angle of about 1.35 Å, 1.11 Å and 113°, respectively, with these being the same for PBE, PBE+U and RPBE calculations. Such adsorbate geometry can be viewed as a Hollow configuration since the atoms' coordinations are comparable to those of a fourfold Hollow site, as visible from Figure S2 in the Supplementary Materials. This configuration represents a reliable starting point to study the C–O bond cleavage, which can qualitatively occur without requiring a large amount of energy, because the proximity of the Rh surface atoms can partially stabilize the highly energetical intermediates that are generated during the bond dissociation. Since this molecular fragment is not stable in the gas phase (it would exist only as a radical species), no comparison with experimental data could be carried out. However, calculations performed on similar systems revealed the same geometrical configuration and an adsorption energy on the Rh (100) surface of about 3.62 eV, which is compatible with our results [30]. As shown in Table 2, the PBE-based and RPBE CHO* adsorption energies are very different, the latter being 0.75 eV less stable than the former. This effect is related to the way the molecule–slab interface regions are treated by the functionals [34,62] and is even more pronounced for the CH* and O* systems, which are the products of the CHO* dissociation. As presented in Table 2, CH* adsorption energy changes of about 1.18 eV changing the functional from PBE to RPBE. This indicates that the choice of the functional can affect the calculated stability of the adsorbed species, and this is reflected in the results of the NEB calculations that we will discuss in the next section. Despite these differences, all calculations provide as equilibrium structure for the CH* species the Hollow adsorbed configuration, with the C-H bond directed perpendicularly to the Rh surface, as visible form Figure 2 panel D. All other adsorption sites give unstable structures that naturally relax into the Hollow configuration during the geometry optimization. The prominent stability of this configuration compared to the other adsorption geometries can be related to the undercoordination of the C atom in the CH species, which needs to be saturated by the highest number of surface metal atoms, occurring in Hollow sites (4-fold coordination). Due to the intrinsic instability of the CH species, in the gas phase, it is not possible to compare the adsorption energies with experimental data. Moreover, most of the available computational results on the CH* specie refer to different Rh surfaces [63–65] or to systems where CH* is co-adsorbed with hydrogen atoms [61]. Despite these differences, these studies in any case indicate the Hollow configuration to be the most stable one and report geometrical parameters comparable with the computed C–H bond length of 1.10 Å and 1.11 Å for the PBE-based and RPBE calculations respectively, and C–Rh distance of 2.09 Å and 2.11 Å for the PBE-based and RPBE calculations respectively.

Additionally, in the case of O*, adsorption energies are strongly dependent on the choice of the XC functional. Here RPBE underbinds the O* species with respect to PBE of about 0.95 eV for the Hollow adsorption site and of 1.05 eV for the Bridge configuration. As happened in the previous cases, these adsorption energy differences seem to be uncorrelated with the adsorption sites stability trend and almost identical geometrical configurations were obtained in all the three calculations. The most stable adsorbed configuration for O* is on the Hollow site, as reported in previous theoretical studies [66–68]. The Bridge-to-Hollow energy difference ranges between 0.12 and 0.22 eV, depending on the calculation level. As reported in Figure 2 panel E, the O–Rh distance is 2.15 Å for the PBE-based calculations, while it increases to 2.20 Å for the RPBE calculation. This bond length difference is compatible with the lower affinity between oxygen and the rhodium surface using the RPBE functional compared to the PBE-based schemes. To be able to compare with the experimental data, as in the H* case, we repeated the calculations referring to O_2 dissociative chemisorption. As visible from the data in parenthesis in Table 2, the favorite chemisorption site is still the Hollow spot with an adsorption energy calculated with PBE functional of about 4.53 eV, which overestimates the available experimental data for dissociative chemisorption of about 0.53 eV [58,69]. On the other hand, changing the functional from PBE to RPBE decreases the adsorption energy to 3.04 eV, and strongly

underestimates the O_2 dissociative chemisorption energy (by 0.96 eV) with respect to the experiment.

Besides considerations on single molecule adsorption, we searched for the most stable co-adsorbate configurations for both the CO*/H* and CH*/O* pairs, which represent the initial and final stage of all our processes, respectively. Our analysis revealed that the less energetic conformation in the case of the CO*/H* pair can be obtained when these species are co-adsorbed in adjacent Bridge sites, as shown in the Supporting Movie (SM) and in Figure S2 attached as Supplementary Material. Regarding the CH*/O* pair, we found that the most stable configuration is the one where the two products species are located on the opposite corner of the square identified by four Hollow sites, as shown in the Supplementary Materials. This arrangement represents the target state of our reaction energy profile analysis.

2.3. Study of the Methanation Rate-Determining Step

As already mentioned, the rate-determining step of the Rh catalyzed CO_2 methanation reaction was identified in the CO* + H* → CH* + O* step through the formation of CHO* species [5,6,10,13,14]. Previous DFT simulations concerning the study of Ru (0001) catalyzed CO_2 reduction, showed that the CHO* formation and its dissociation have comparable energy barriers [13,29]. A kinetic study performed on top of such calculations points to the CHO* dissociation as the rds of the whole reduction process [13]. To the best of our knowledge, no theoretical studies are currently available concerning the CO_2 reduction over rhodium surfaces; what is known from the study of CH_3OH dehydrogenation on Rh (111) is that the CHO* formation has an energy barrier similar to that found on the Ru (0001) surface [13,29,70]. Therefore, we calculated the energy landscape of the whole process generating the CH*/O* co-adsorbed pair from CO* and H* through CHO*, at the PBE, PBE+U and RPBE levels. We will discuss in the next paragraph the effect of the different functionals, while we focus here on the reaction mechanism itself, studied at the PBE+U level. The calculated energy profile is shown in Figure 3.

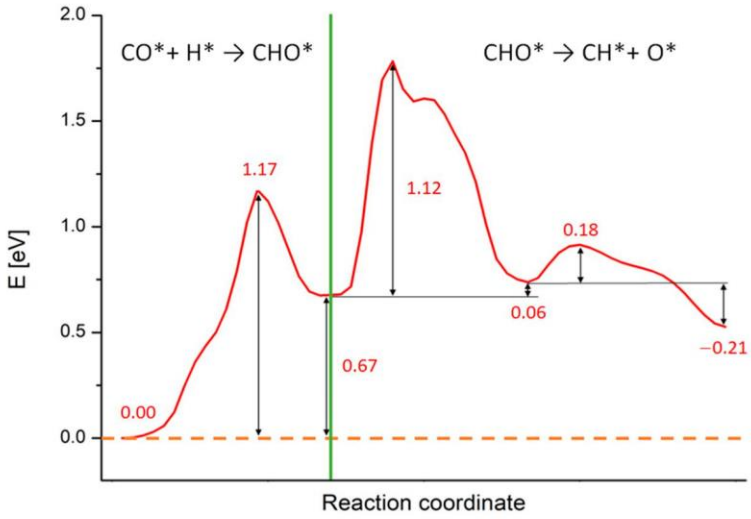

Figure 3. Reaction energy profiles for the whole CO* + H* → CH* + O* reaction on Rh (100) surface calculated at the PBE+U level. The numbers report the values of energy barriers and reaction energies in eV. The green line separates the two subprocesses in which we split the calculations: the CHO* generation starting from CO* and H and the CHO* dissociation in CH* and O*.

As noticeable, all processes are endothermic and require a certain amount of energy to occur. The green line in Figure 3 separates the two subprocesses in which we split the calculations: the CHO* generation starting from CO* and H*, occurring in a single-step, and the CHO* dissociation, occurring in two sub-steps. During the CHO* formation,

the species moves and rotate on the Rh (100) surface in order to generate CHO* and the Rh outermost layer gets slightly distorted. This step requires ca. 1.17 eV to take place, while the reaction energy is around 0.67 eV, as written in Figure 3. Such results compare well with simulations performed on Rh (111) and Ru (0001) surfaces (although different XC-functionals were used) [29,70]. A movie representing this first reaction step is available as SM, while the meaningful snapshots of the process are reported in Figure S2 in the Supplementary Material section. Differently from the simple landscape of this first process, the CHO* dissociation exhibits a more complex energy profile. We focus now on this process whose PB energy profile and related geometries are shown in Figure 4. The initial configuration of the dissociation is shown in Figure 2 panel C (side view) and in the inset A of Figure 4 (top view), while the final configuration is shown in inset C of Figure 4. The values of the energy profiles at the most relevant points of the reaction are explicitly indicated in Figure 4.

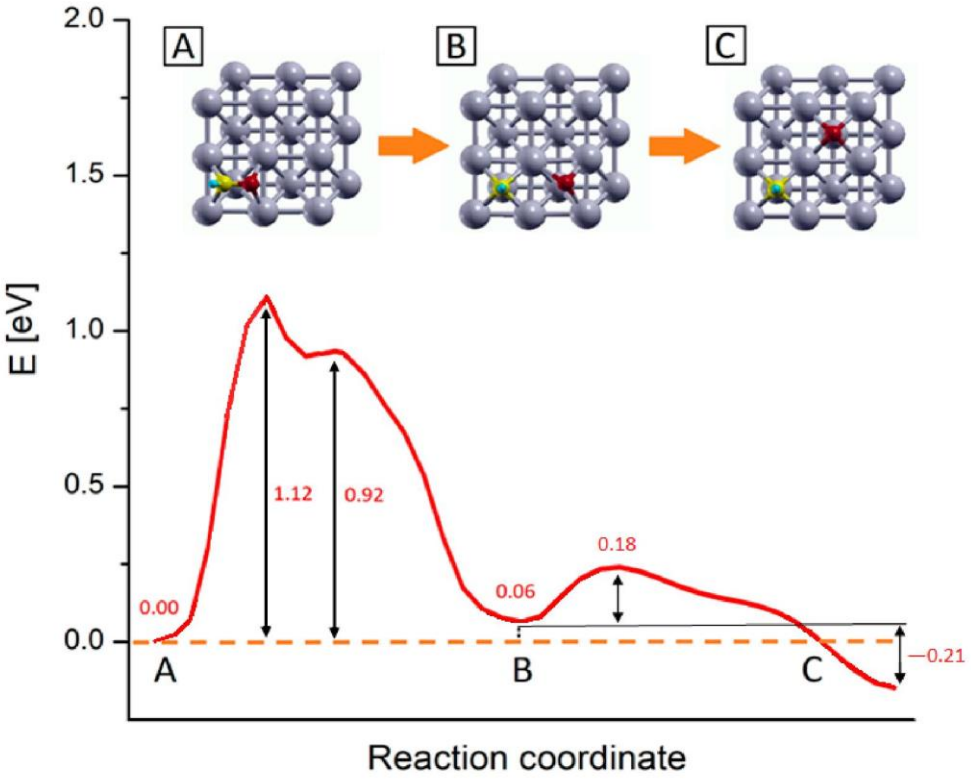

Figure 4. PBE+U computed reaction energy profiles for the CHO* → CH* + O* step on Rh (100) surface. The numbers report the values of energy barriers and reaction energies in eV. Inset pics represent the main step of the process: (**A**) CHO* most stable configuration, (**B**) configuration of dissociated species, and (**C**) equilibrium configuration of the dissociated species upon oxygen diffusion. Yellow, red, light blue and grey represent C, O, H and Rh atoms respectively.

Following the energy profiles, the whole reaction can be roughly divided into two subprocesses: the first one comprises the C-O bond dissociation and O* migration reaching a first local energy minimum corresponding to the configuration B in Figure 4; in the following step, the O* further migrates to reach the products most stable configuration (inset C). In the first subprocess, starting from the CHO* equilibrium configuration (inset A in Figure 4), there is an initial energy growth, corresponding to the elongation of the C–O bond and consequent adjustment of the outermost Rh layer, which actively takes part in this first dissociation step. After this initial growth, the profiles reach their absolute maximums, which correspond to a state where the CH* and O* species are separated but the system is highly unstable, as the two fragments are located into the same 2 × 2 Rh cell, in mixed

Bridge-Hollow sites. This configuration constitutes the transition state for the CHO* bond dissociation, as confirmed by the vibrational analysis which reveals the presence of an imaginary frequency associated with a normal mode pointing along the reaction coordinate. After this sharp maximum, the profiles exhibit a shoulder, corresponding to a configuration in which both species are in Bridge adsorption sites. This is a metastable configuration where the adsorbates are located in a relatively stable point but are not in their minimum energy configuration. In the following steps O* starts to migrate towards the Hollow site of the adjacent Rh 2 $\times$ 2 cell, while the CH* makes structural adjustments and falls into its energy minimum structure, a Hollow adsorption site, as previously discussed. Within this subprocess, the outermost Rh layer plays a primary role in supporting all structural changes. This can be noticed for example by looking at the inset B of Figure 4, where despite the whole system being in an energy minimum configuration, the Rh atoms of the outermost layer are still distorted, due to the long-range interactions acting among the two adsorbed species. In the second subprocess of the reaction, O* diffuses towards the Hollow site corresponding to its position in the target state (inset C of Figure 4), passing through a Bridge configuration. Once the final Hollow spot is reached, the interactions among the adsorbed species are minimized, the surface atoms can relax all the tension accumulated along these processes and the system reaches its global minimum. These two subprocesses can be viewed in the movie SM attached as Supplementary Material, while in Figure S2 the snapshots of the molecular configurations in the main points of interest are collected.

As shown in Figure 4, the process that requires more energy is the first dissociation of the C-O bond, with an activation energy barrier of about 1.12 eV to occur. These activation energy barriers are compatible with those of theoretical studies carried out on similar systems: in particular, Zhang et al. [29] estimated that CHO* dissociation can take place on Ru (100) with an activation barrier of about 1.48 eV, while Avanesian et al. [13] showed that on Rh (211), this step can occur with a free energy barrier of about 1.43 eV. At the same time, the computed barriers overestimate experimental values for the whole CO_2 methanation reaction that range from 0.7 to 1.0 eV depending on the support [16,19,71–73]. The energy barrier overestimation with respect to experiments can be linked to contributions arising from the presence of co-adsorbed species. Indeed, the calculated energy profiles refer to the dissociation of an isolate CHO* species without accounting for the presence of other co-absorbed species. However, it was proved that after the first dissociative adsorption of CO_2, the dissociated oxygen atoms remain absorbed on the surface and their presence reduces the activation barrier of the whole methanation reaction [19,66,73]. This explains at the same time why the methanation activation energy is lower for CO_2 than that of CO of about 0.15 $\div$ 0.35 eV, depending on the experimental conditions [16,19,21,73], and the overestimation of the reaction barrier presented in this work.

Considering the high similarities in the physico-chemical features between the systems, our calculations suggests that the Rh (100) catalyzed process occur as in the case of Ru (0001), being the energy landscapes profiles and the activation barriers comparable for CHO* formation and dissociation [13,29]. Taking into account the role of kinetics, it was found that on the Ru (0001), the slowest process is the CHO* dissociation, even if this step is less energetically demanding compared to the CHO* generation [13]. In analogy with these results, the CHO* cleavage could be the rds of the whole CO_2 reduction also in this case, although further investigation on the kinetics of this reaction exploiting, e.g., variational transition state theory [74], are needed to fully validate this hypothesis.

Finally, all the results presented here refer to systems in zero-absolute temperature conditions and do not include any entropic contribution. Indeed, previous studies concerning this reaction on similar systems showed entropic corrections to the free energy on the order of 0.1 eV at room temperature [13,28,29], smaller than the difference related to the use of various computational setups, as shown in the next section.

2.4. Comparison among Different Computational Techniques

To highlight the different performances given by the various computational techniques, we report in Figure 5 the calculated NEB profile for the whole process, where for a better comparison, the three profiles are aligned by setting the energy of the initial configuration to zero.

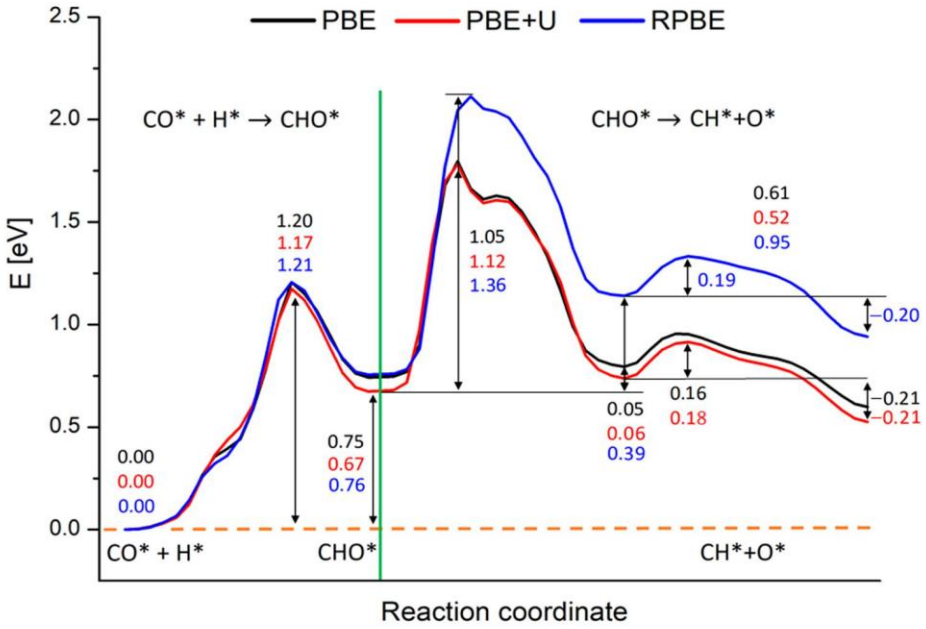

Figure 5. Reaction energy profiles for the whole CO* + H* → CH* + O* reaction on Rh (100) surface, involving CHO*. Black, red and blue lines represent the profiles calculated at the PBE, PBE+U and RPBE levels respectively. The numbers report the values of energy barriers and reaction energies in eV. The green line separates the two subprocesses in which we split the calculations: the CHO* generation starting from CO* and H and the CHO* dissociation in CH* and O*.

PBE, PBE+U and RPBE yield approximately the same results concerning the generation of CHO*. The activation energy is estimated in ca. 1.20 eV, while the reaction energy is around 0.75 eV for PBE and RPBE calculations, and 0.67 eV for the PBE+U one, as reported in Figure 5. At odds with these results, RPBE description of the CHO* dissociation step deviates strongly from the PBE and PBE+U ones. As is clearly visible from Figure 6, starting from a certain point along the reaction coordinate prior to the first maximum, the RPBE energy diagram is shifted to higher energies when compared to the PBE and PBE+U cases. This upshift slightly varies with the reaction coordinate until the minimum corresponding to configuration B is reached, while it is almost constant, ranging between 0.36 eV and 0.39 eV, during the second part of the process.

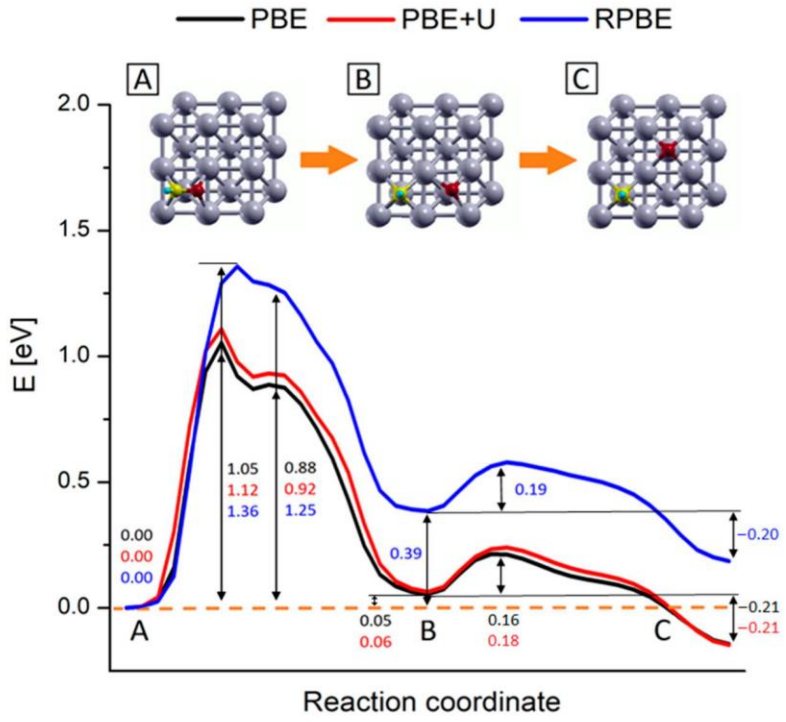

Figure 6. Reaction energy profiles for the CHO* → CH* + O* reaction on Rh (100) surface. Black, red and blue lines represent the profiles calculated at the PBE, PBE+U and RPBE levels respectively. The numbers report the values of energy barriers and reaction energies in eV. Inset pics represent the geometries of the main steps of the process: (A) CHO* most stable configuration, (B) configuration of dissociated species and (C) equilibrium configuration of the dissociated species upon oxygen diffusion. Yellow, red, light blue and grey represent C, O, H and Rh atoms respectively.

To understand the nature of such energy difference, we decomposed the energetics of the system on the basis of energy data coming from simpler systems. As shown in Figure 7, we were able to decompose the system energetics in three main contributions: the adsorption energies of single CHO*, CH*, O* species, the energy of the free CHO, CH and O (and thus the CH–O bond strength), and the CH*–O*co-adsorption energy. The latter can be recovered on the basis of the dissociated CH*/O* system (the last image of NEB calculation) and the isolated ones. More details on these calculations can be found in the Supplementary Material.

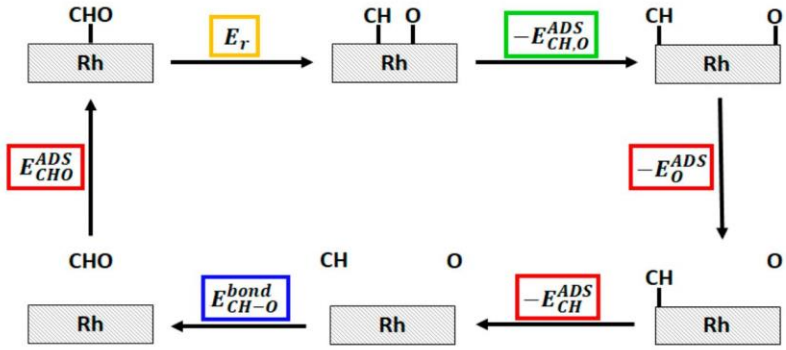

Figure 7. Hess cycle of the decomposition of the CHO* → CH* + O* reaction energy E_r (highlighted in yellow). The three main contribution, namely the adsorption energies (E^{ADS}) of CHO*, CH* and O*, the CH–O bond strength in the free CHO species (E^{bond}_{CH-O}), and the CH*–O*co-adsorption energy ($E^{ADS}_{CH,O}$) are highlighted in red, blue and green respectively.

The analysis shows that, in line with the data reported in Table 2, the main difference between PBE and RPBE functionals can be ascribed to the way the free species and the adsorbed species energetics are modeled, while a minor contribution is given by the estimation of the co-adsorption energy. As shown in Table 2, RPBE has a tendency toward lower binding energies with respect to PBE schemes, and this tendency is particularly strong for CH* and O* where the PBE to RPBE adsorption energy differences are about twice the CHO* PBE to RPBE adsorption energy difference. These considerations can motivate the shift observed in the NEB profiles and indeed it can be noticed that the profiles in Figure 4 begin to diverge once the C–O bond is split, i.e., when the substrate-adsorbate interaction increases.

3. Materials and Methods

All simulations were carried out at the DFT level using a plane-waves basis set, as implemented in Quantum Espresso version 6.5. [75] The Perdew-Burke-Ernzerhof (PBE) [33] and the Revised Perdew-Burke-Ernzerhof (RPBE) [34] exchange-correlation (XC) functionals were employed to describe the electron-electron interactions. PBE+U calculations were also performed on systems containing C and O atoms, using as corrective parameter U = 0.65 eV both for C and O species. By using this U value, in line with the one adopted in similar previous calculations [55,56], the computed CO adsorption energies on Rh (100) surface match the experimental data. As the main process in this reaction concerned the generation and cleavage of covalent bonds, we did not include any dispersion corrections. The energy cut-off for the plane waves expansion was set to 1080 eV and 820 eV for PBE and RPBE calculations respectively. Core-electrons were modeled with the XC-compatible Optimized Norm-Conserving Vanderbilt (ONCV) pseudopotentials. Bulk calculations for the Rh crystals were performed on a face centered cubic (fcc) cell, using an $18 \times 18 \times 18$ k-point mesh, yielding an equilibrium lattice constant of 3.833 Å and 3.922 Å for the PBE and RPBE calculations respectively, in close agreement (especially in the case of PBE) with the experimental value [76] extrapolated at 0 °K of 3.797 Å. The PBE and RPBE calculated bulk cell parameters were used to build the 8-layers Rh (100) slabs which represent the catalyst surface. Building the supercells, a 20 Å vacuum layer was added along the direction orthogonal to the surface in order to avoid any interaction between consecutive replicas. Keeping the two inner layers fixed at their ideal bulk positions, all the remaining atomic positions were relaxed until the residual forces were lower than 10^{-4} eV/Å, with a convergence threshold on the ground state total energy of 10^{-9} eV. All relaxation runs were carried out using the Broyden–Fletcher–Goldfarb–Shanno (BFGS) quasi-Newton algorithm [77].

Geometry optimizations involving adsorbed species were performed on single molecules adsorbed on a 3×3 eight-layer-thick supercell. This supercell dimension was chosen in order to avoid spurious interactions among molecules belonging to nearby unit cells within the same surface. The calculations on these systems were performed using a $6 \times 6 \times 1$ k-point mesh, the same Brillouin zone sampling of the converged bulk calculations ensuring adsorption energies accurate up to ± 0.01 eV. Dipole corrections were applied along the direction orthogonal to the slab surface to prevent artifacts related to the presence of an artificial net electric field in the case of asymmetric slabs [78]. Calculations on the adsorbed species in gas phase were carried out by fully relaxing the respective geometries within fcc cells with a 40 Å lattice parameter. The study of the methanation rds was conducted using the Climbing Image Nudged Elastic Band technique (CI-NEB) [32]. Transition state geometries and energy barriers for the process were obtained by imposing a convergence threshold on the forces of 0.05 eV/A. The CI-NEB simulations was split into two separate calculations, namely the formation of the intermediate CHO* and its dissociation. The former calculation was conducted using 20 images, while the latter exploited a total of 40 images. Transition states were identified as the maxima in the NEB energy profile in analogy with previous study concerning CO_2 reduction over various metal surfaces [13,29]. Furthermore, to confirm the nature of the transition state associated

with the rate-determining step, we performed vibrational frequency and normal mode calculations on the geometry corresponding to the maximum of the rds NEB profile, by computing the Hessian matrix on the solely atoms of the adsorbate, while the atoms of the slab were kept fixed [75]. The starting point of the CHO* generation simulation was the most stable co-adsorbed CO*/H* configuration, while the final image was the relaxed CHO* complex adsorbed on the Rh (100) surface. CHO* dissociation calculations started from this last image and ended in the configuration in which the complex was dissociated, and the CH* and O* relative positions minimized the total energy of the system.

4. Conclusions

In conclusion, we studied the rate-determining step of the rhodium catalyzed CO_2 reduction, which is the hydrogen-assisted CO* dissociation through formation and subsequent dissociation of the CHO* intermediate [4,5,13,15]. In the present work, this reaction step was studied by means of DFT and CI-NEB techniques on the Rh (100) surface. Within this framework, the PBE, RBPE XC functionals and PBE+U methods were employed. Overall, all the methods predicted the same energetics for the CHO* generation from CO* and H*, which was found to be a single step process. On the contrary, the CHO* dissociation was found to be happening in two separate steps: first the elongation and breaking of the C–O bond, and second the migration of the O* species to its equilibrium site, with the concomitant relaxation of surface tension. Although finding the same process and geometries, RPBE results differ from PBE based ones when taking a closer look at the energies which are involved in the CHO* $\rightarrow$ CH* + O* step: the products being less stable by ~0.35 eV and the C–O bond break energy barrier strongly overestimated for RPBE. The origin of this difference resides in the way RPBE was designed in order to correct the adsorption energetics of LDA and PBE functionals [34,62]. The tendency of RPBE to underbind with respect to PBE is especially enhanced in the case of the product species. For example, our results show that RPBE strongly underbinds the O* species with respect to experimental data, largely overcorrecting PBE overbinding. The larger underbinding in the O* and CH* species compared to CHO* explains both the deviation of the RPBE profile with respect to the PBE based one in the moment the C–O bond breaks and the product species are formed, and the subsequent almost rigid shift of the profile. A similar picture to that found on Ru (0001) concerning the energetics of the two subprocesses was found, suggesting the CHO* cleavage as the rate-determining step of the whole Rh-catalyzed methanation reaction.

Supplementary Materials: The following are available online at https://www.mdpi.com/article/10.3390/catal11050538/s1, Video SM: CI-NEB calculated mechanism for the CHO* generation and dissociation; Text: details on the calculations of the interaction energy among co-adsorbed species, snapshots of the meaningful involved in the PBE+U calculated NEB trajectory.

Author Contributions: Conceptualization, M.V., M.M. and S.C.; investigation, M.V. and M.M.; writing—original draft preparation, M.V. and M.M.; writing—review and editing, M.V., M.M. and S.C.; supervision, M.M. and S.C.; project administration, S.C.; funding acquisition, S.C. All authors have read and agreed to the published version of the manuscript.

Funding: M.M. and S.C. acknowledge funding from the ERC under the grant ERC-CoG-681285 TAME Plasmons. M.V. and S.C. also acknowledge funding from MIUR under the grant R164LZWZ4A MIUR-FARE Plasmo-Chem.

Data Availability Statement: All relevant data are contained in the present manuscript. Other inherent data are available on request from the corresponding author.

Acknowledgments: The authors acknowledge CINECA (Bologna, Italy), the Leibniz Supercomputing Centre (Munich, Germany) and the CRESCO/ENEAGRID High Performance Computing (Rome, Italy) infrastructure and its staff for computational resources and technical support.

Conflicts of Interest: The authors declare no conflict of interest.

Appendix A

The precise structure and the physical features of the rhodium surface strongly depends on the computational technique adopted in the calculations. To compare the performance of the different xc functionals, we define three main quantities that characterize the catalyst properties, namely the surface energies σ, work function φ, and surface lattice relaxation parameter d_{ij} %. These quantities are defined as follow:

- σ is the energy required to build a surface starting from an infinite bulk crystal:

$$\sigma = \frac{E_{slab} - n\varepsilon_{bulk}}{2} \quad \text{(A1)}$$

  where E_{slab} is the total energy of the n-layer slab and ε_{bulk} is the energy per atom of the infinite bulk. In this case, $n = 8$. The $\frac{1}{2}$ factor accounts for the presence of two symmetric surfaces for each slab.
- φ represents the energy required for extracting an electron from the system:

$$\varphi = V_{vacuum} - \varepsilon_{Fermi} \quad \text{(A2)}$$

  where V_{vacuum} is the electrostatic potential calculated at the center of vacuum region and ε_{Fermi} is the Fermi energy of the slab.
- d_{ij} %: quantifies how much the superficial layers of the slab move with respect to their ideal position in the bulk crystal structure:

$$d_{ij}\% = \frac{d_{ij} - d_0}{d_0} \cdot 100 \quad \text{(A3)}$$

  where d_{ij} is the distance between layers i and j, and d_0 is the distance between the layers of the bulk.

These quantities were calculated for the Rh (100) slabs treated with different computational approaches and the results, together with some meaningful literature data, are reported in Section 2.1.

References

1. Intergovernmental Panel on Climate Change. *IPCC's Fifth Assessment Report*; IPCC: Geneva, Switzerland, 2014.
2. Vijayavenkataraman, S.; Iniyan, S.; Goic, R. A review of climate change, mitigation and adaptation. *Renew. Sustain. Energy Rev.* **2012**, *16*, 878–897. [CrossRef]
3. Mebrahtu, C.; Krebs, F.; Abate, S.; Perathoner, S.; Centi, G.; Palkovits, R. CO_2 Methanation: Principles and Challenges. In *Studies in Surface Science and Catalysis*; Elsevier B.V.: Amsterdam, The Netherlands, 2019; Volume 178, pp. 85–103, ISBN 9780444641274.
4. Rönsch, S.; Schneider, J.; Matthischke, S.; Schlüter, M.; Götz, M.; Lefebvre, J.; Prabhakaran, P.; Bajohr, S. Review on methanation—From fundamentals to current projects. *Fuel* **2016**, *166*, 276–296. [CrossRef]
5. Miao, B.; Ma, S.S.K.; Wang, X.; Su, H.; Chan, S.H. Catalysis mechanisms of CO_2 and CO methanation. *Catal. Sci. Technol.* **2016**, *6*, 4048–4058. [CrossRef]
6. Su, X.; Xu, J.; Liang, B.; Duan, H.; Hou, B.; Huang, Y. Catalytic carbon dioxide hydrogenation to methane: A review of recent studies. *J. Energy Chem.* **2016**, *25*, 553–565. [CrossRef]
7. Erdőhelyi, A. Hydrogenation of carbon dioxide on supported rh catalysts. *Catalysts* **2020**, *10*, 155. [CrossRef]
8. Kattel, S.; Liu, P.; Chen, J.G. Tuning Selectivity of CO_2 Hydrogenation Reactions at the Metal/Oxide Interface. *J. Am. Chem. Soc.* **2017**, *139*, 9739–9754. [CrossRef] [PubMed]
9. Zhang, Y.; He, S.; Guo, W.; Hu, Y.; Huang, J.; Mulcahy, J.R.; Wei, W.D. Surface-Plasmon-Driven Hot Electron Photochemistry. *Chem. Rev.* **2018**, *118*, 2927–2954. [CrossRef] [PubMed]
10. Zhang, X.; Li, X.; Zhang, D.; Su, N.Q.; Yang, W.; Everitt, H.O.; Liu, J. Product selectivity in plasmonic photocatalysis for carbon dioxide hydrogenation. *Nat. Commun.* **2017**, *8*, 1–9. [CrossRef]
11. Li, X.; Everitt, H.O.; Liu, J. Confirming nonthermal plasmonic effects enhance CO_2 methanation on Rh/TiO_2 catalysts. *Nano Res.* **2019**, *12*, 1906–1911. [CrossRef]
12. Kim, C.; Hyeon, S.; Lee, J.; Kim, W.D.; Lee, D.C.; Kim, J.; Lee, H. Energy-efficient CO_2 hydrogenation with fast response using photoexcitation of CO_2 adsorbed on metal catalysts. *Nat. Commun.* **2018**, *9*, 1–8. [CrossRef] [PubMed]
13. Avanesian, T.; Gusmão, G.S.; Christopher, P. Mechanism of CO_2 reduction by H_2 on Ru(0001) and general selectivity descriptors for late-transition metal catalysts. *J. Catal.* **2016**, *343*, 86–96. [CrossRef]

14. Dai, X.; Sun, Y. Reduction of carbon dioxide on photoexcited nanoparticles of VIII group metals. *Nanoscale* **2019**, *11*, 16723–16732. [CrossRef]
15. Wang, J.; Kawazoe, Y.; Sun, Q.; Chan, S.; Su, H. The selectivity and activity of catalyst for CO hydrogenation to methanol and hydrocarbon: A comparative study on Cu, Co and Ni surfaces. *Surf. Sci.* **2016**, *645*, 30–40. [CrossRef]
16. Sexton, B.A.; Somorjai, G.A. The hydrogenation of CO and CO_2 over polycrystalline rhodium: Correlation of surface composition, kinetics and product distributions. *J. Catal.* **1977**, *46*, 167–189. [CrossRef]
17. Castner, D.G.; Sexton, B.A.; Somorjai, G.A. Leed and Thermal Desorption Studies of Small Molecules (H_2, O_2, CO, CO_2, NO, C_2H_4, C_2H_2 and C) Chemisorbed on the Rhodium (111) and (100) Surfaces. *Surf. Sci.* **1978**, *71*, 519–540. [CrossRef]
18. van Tol, M.F.H.; Gielbert, A.; Nieuwenhuys, B.E. The adsorption and dissociation of CO_2 on Rh. *Appl. Surf. Sci.* **1993**, *67*, 166–178. [CrossRef]
19. Fisher, I.A.; Bell, A.T. A comparative study of CO and CO_2 hydrogenation over Rh/SiO_2. *J. Catal.* **1996**, *162*, 54–65. [CrossRef]
20. Novák, É.; Fodor, K.; Szailer, T.; Oszkó, A.; Erdöhelyi, A. CO_2 hydrogenation on Rh/TiO_2 previously reduced at different temperatures. *Top. Catal.* **2002**, *20*, 107–117. [CrossRef]
21. Jacquemin, M.; Beuls, A.; Ruiz, P. Catalytic production of methane from CO_2 and H_2 at low temperature: Insight on the reaction mechanism. *Catal. Today* **2010**, *157*, 462–466. [CrossRef]
22. Karelovic, A.; Ruiz, P. Mechanistic study of low temperature CO_2 methanation over Rh/TiO_2 catalysts. *J. Catal.* **2013**, *301*, 141–153. [CrossRef]
23. Liu, X.; Sun, L.; Deng, W.Q. Theoretical Investigation of CO_2 Adsorption and Dissociation on Low Index Surfaces of Transition Metals. *J. Phys. Chem. C* **2018**, *122*, 8306–8314. [CrossRef]
24. Solymosi, F.; Pásztor, M. Analysis of the IR-spectral behavior of adsorbed CO formed in H_2 + CO_2 surface interaction over supported rhodium. *J. Catal.* **1987**, *104*, 312–322. [CrossRef]
25. Henderson, M.A.; Worley, S.D. An Infrared Study of the Dissociation of Carbon Dioxide over Support Rhodium Catalyst. *Surf. Sci.* **1985**, *149*, L1–L6. [CrossRef]
26. Claver, C. *Rhodium Catalysis*; Springer International Publishing: Cham, Switzerland, 2018; ISBN 9783319666631.
27. Dietz, L.; Piccinin, S.; Maestri, M. Mechanistic insights into CO_2 activation via reverse water—Gas shift on metal surfaces. *J. Phys. Chem. C* **2015**, *119*, 4959–4966. [CrossRef]
28. Alfonso, D.R. Further theoretical evidence for hydrogen-assisted CO dissociation on Ru(0001). *J. Phys. Chem. C* **2013**, *117*, 20562–20571. [CrossRef]
29. Zhang, S.T.; Yan, H.; Wei, M.; Evans, D.G.; Duan, X. Hydrogenation mechanism of carbon dioxide and carbon monoxide on Ru(0001) surface: A density functional theory study. *RSC Adv.* **2014**, *4*, 30241–30249. [CrossRef]
30. Zhang, M.; Wu, X.; Yu, Y. A comparative DFT study on the dehydrogenation of methanol on Rh(100) and Rh(110). *Appl. Surf. Sci.* **2018**, *436*, 268–276. [CrossRef]
31. Zhu, Y.A.; Chen, D.; Zhou, X.G.; Yuan, W.K. DFT studies of dry reforming of methane on Ni catalyst. *Catal. Today* **2009**, *148*, 260–267. [CrossRef]
32. Henkelman, G.; Uberuaga, B.P.; Jónsson, H. Climbing image nudged elastic band method for finding saddle points and minimum energy paths. *J. Chem. Phys.* **2000**, *113*, 9901–9904. [CrossRef]
33. Perdew, J.P.; Burke, K.; Ernzerhof, M. Generalized gradient approximation made simple. *Phys. Rev. Lett.* **1996**, *77*, 3865–3868. [CrossRef] [PubMed]
34. Hammer, B.; Hansen, L.B.; Nørskov, J.K. Improved adsorption energetics within density-functional theory using revised Perdew-Burke-Ernzerhof functionals. *Phys. Rev. B Condens. Matter Mater. Phys.* **1999**, *59*, 7413–7421. [CrossRef]
35. Tolba, S.A.; Gameel, K.M.; Ali, B.A.; Almossalami, H.A.; Allam, N.K. Density Functional Calculations—Recent Progresses of Theory and Application. Intech Open: London, UK, 2018; pp. 3–30. [CrossRef]
36. Patra, A.; Bates, J.E.; Sun, J.; Perdew, J.P. Properties of real metallic surfaces: Effects of density functional semilocality and van der Waals nonlocality. *Proc. Natl. Acad. Sci. USA* **2017**, *114*, E9188–E9196. [CrossRef]
37. Xie, J.; Scheffler, M. Structure and dynamics of Rh surfaces. *Phys. Rev. B* **1998**, *57*, 4768–4775. [CrossRef]
38. Begley, A.M.; Kim, S.K.; Jona, F.; Marcus, P.M. Surface relaxation of Rh{001}. *Phys. Rev. B* **1993**, *48*, 12326–12329. [CrossRef]
39. Derry, G.N.; Kern, M.E.; Worth, E.H. Recommended values of clean metal surface work functions. *J. Vac. Sci. Technol. A* **2015**, *33*, 060801. [CrossRef]
40. Tyson, W.R. Surface energies of solid metals. *Can. Metall. Q.* **1975**, *14*, 307–314. [CrossRef]
41. De Waele, S.; Lejaeghere, K.; Sluydts, M.; Cottenier, S. Error estimates for density-functional theory predictions of surface energy and work function. *Phys. Rev. B* **2016**, *94*, 235418. [CrossRef]
42. Kose, R.; Brown, W.A.; King, D.A. Role of Lateral Interactions in Adsorption Kinetics: CO/Rh{100}. *J. Phys. Chem. B* **1999**, *103*, 8722–8725. [CrossRef]
43. Jansen, M.M.M.; Gracia, J.; Nieuwenhuys, B.E.; Niemantsverdriet, J.W. Interactions between co-adsorbed CO and H on a Rh(100) single crystal surface. *Phys. Chem. Chem. Phys.* **2009**, *11*, 10009–10016. [CrossRef]
44. De Jong, A.M.; Niemantsverdriet, J.W. The adsorption of CO on Rh(100): Reflection absorption infrared spectroscopy, low energy electron diffraction, and thermal desorption spectroscopy. *J. Chem. Phys.* **1994**, *101*, 10126–10133. [CrossRef]
45. Kim, J.; Peebles, H.C.; White, J.M. Electron spectroscopic study of the interaction of coadsorbed CO and D_2 on Rh(100) at low temperature. *Surf. Sci.* **1982**, *114*, 363–380. [CrossRef]

46. Van Bavel, A.P.; Hopstaken, M.J.P.; Curulla, D.; Niemanstsverdriet, J.W.; Lukkien, J.J.; Hilbers, P.A.J. Quantification of lateral repulsion between coadsorbed CO and N on Rh(100) using temperature-programmed desorption, low-energy electron diffraction, and Monte Carlo simulations. *J. Chem. Phys.* **2003**, *119*, 524–532. [CrossRef]
47. Baraldi, A.; Gregoratti, L.; Comelli, G.; Dhanak, V.R.; Kiskinova, M.; Rosei, R. CO adsorption and CO oxidation on Rh(100). *Appl. Surf. Sci.* **1996**, *99*, 1–8. [CrossRef]
48. Hung, T.C.; Liao, T.W.; Liao, Z.H.; Hsu, P.W.; Cai, P.Y.; Lu, W.H.; Wang, J.H.; Luo, M.F. Dependence on size of supported Rh nanoclusters for CO adsorption. *RSC Adv.* **2016**, *6*, 3830–3839. [CrossRef]
49. Nieskens, D.L.S.; Jansen, M.M.M.; Van Bavel, A.P.; Curulla-Ferré, D.; Niemantsverdriet, J.W. The influence of carbon on the adsorption of CO on a Rh(100) single crystal. *Phys. Chem. Chem. Phys.* **2006**, *8*, 624–632. [CrossRef]
50. Nieskens, D.L.S.; Curulla-Ferré, D.; Niemantsverdriet, J.W. Atom-molecule interactions on transition metal surfaces: A DFT study of CO and several atoms on Rh(100), Pd(100) and Ir(100). *ChemPhysChem* **2006**, *7*, 1075–1080. [CrossRef]
51. Liu, D.J. CO oxidation on Rh(100): Multisite atomistic lattice-gas modeling. *J. Phys. Chem. C* **2007**, *111*, 14698–14706. [CrossRef]
52. Gajdoš, M.; Eichler, A.; Hafner, J. CO adsorption on close-packed transition and noble metal surfaces: Trends from ab initio calculations. *J. Phys. Condens. Matter* **2004**, *16*, 1141–1164. [CrossRef]
53. Mason, S.E.; Grinberg, I.; Rappe, A.M. First-principles extrapolation method for accurate CO adsorption energies on metal surfaces. *Phys. Rev. B* **2004**, *69*, 161401. [CrossRef]
54. Tan, L.; Huang, L.; Liu, Y.; Wang, Q. Detailed mechanism of the NO + CO reaction on Rh(100) and Rh(111): A first-principles study. *Appl. Surf. Sci.* **2018**, *444*, 276–286. [CrossRef]
55. Kresse, G.; Gil, A.; Sautet, P. Significance of single-electron energies for the description of CO on Pt(111). *Phys. Rev. B* **2003**, *68*, 3–6. [CrossRef]
56. Köhler, L.; Kresse, G. Density functional study of CO on Rh(111). *Phys. Rev. B* **2004**, *70*, 165405. [CrossRef]
57. Efstathiou, A.M.; Bennett, C.O. Enthalpy and entropy of H_2 Adsorption on Rh/Al_2O_3 measured by temperature-programmed desorption. *J. Catal.* **1990**, *124*, 116–126. [CrossRef]
58. Kose, R.; Brown, W.A.; King, D.A. Calorimetric heats of dissociative adsorption for O_2 on Rh{100}. *Surf. Sci.* **1998**, *402–404*, 856–860. [CrossRef]
59. Panayotov, D.; Mihaylov, M.; Nihtianova, D.; Spassov, T.; Hadjiivanov, K. Spectral evidence for hydrogen-induced reversible segregation of CO adsorbed on titania-supported rhodium. *Phys. Chem. Chem. Phys.* **2014**, *16*, 13136–13144. [CrossRef]
60. Zhang, R.; Liu, F.; Zhao, X.; Wang, B.; Ling, L. First-Principles Study about the Effect of Coverage on H_2 Adsorption and Dissociation over a Rh(100) Surface. *J. Phys. Chem. C* **2015**, *119*, 10355–10364. [CrossRef]
61. Wang, B.; Song, L.; Zhang, R. The dehydrogenation of CH_4 on Rh(111), Rh(110) and Rh(100) surfaces: A density functional theory study. *Appl. Surf. Sci.* **2012**, *258*, 3714–3722. [CrossRef]
62. Wellendorff, J.; Silbaugh, T.L.; Garcia-Pintos, D.; Nørskov, J.K.; Bligaard, T.; Studt, F.; Campbell, C.T. A benchmark database for adsorption bond energies to transition metal surfaces and comparison to selected DFT functionals. *Surf. Sci.* **2015**, *640*, 36–44. [CrossRef]
63. Lin, Y.Z.; Sun, J.; Lin, J.D.; Chen, H.B.; Liao, D.W.; Yi, J.; Liao, D.W.; Chen, H.B.; Liao, D.W. Energetics of chemisorption and conversion of methane on transition metal surfaces. *J. Mol. Struct. THEOCHEM* **2002**, *587*, 63–71. [CrossRef]
64. Van Grootel, P.W.; Van Santen, R.A.; Hensen, E.J.M. Methane dissociation on high and low indices Rh surfaces. *J. Phys. Chem. C* **2011**, *115*, 13027–13034. [CrossRef]
65. Van Grootel, P.W.; Hensen, E.J.M.; Van Santen, R.A. The CO formation reaction pathway in steam methane reforming by rhodium. *Langmuir* **2010**, *26*, 16339–16348. [CrossRef]
66. Wang, Y.Q.; Lv, C.Q.; Wang, G.C. Chemisorbed oxygen atom on the activation of C-H bond in methane: A Rh model study. *RSC Adv.* **2015**, *5*, 66221–66230. [CrossRef]
67. Diao, Z.Y.; Hao, C.; Wang, Z.X.; Dong, C.C.; Pang, X.H. Adsorption, vibration, and diffusion of O atoms on Rh low-index and (711) stepped defective surfaces. *J. Phys. Chem. B* **2005**, *109*, 12467–12473. [CrossRef]
68. Xing, B.; Pang, X.Y.; Wang, G.C. C-H bond activation of methane on clean and oxygen pre-covered metals: A systematic theoretical study. *J. Catal.* **2011**, *282*, 74–82. [CrossRef]
69. Brown, W.A.; Kose, R.; King, D.A. Femtomole adsorption calorimetry on single-crystal surfaces. *Chem. Rev.* **1998**, *98*, 797–831. [CrossRef]
70. Jiang, R.; Guo, W.; Li, M.; Zhu, H.; Zhao, L.; Lu, X.; Shan, H. Methanol dehydrogenation on Rh(111): A density functional and microkinetic modeling study. *J. Mol. Catal. A Chem.* **2011**, *344*, 99–110. [CrossRef]
71. Solymosi, F.; Erdöhelyi, A. Methanation of CO_2 on supported rhodium catalysts. *Stud. Surf. Sci. Catal.* **1981**, *7*, 1448–1449. [CrossRef]
72. Zhang, Z.; Kladi, A.; Verykios, X.E. Effects of carrier doping on kinetic parameters of CO_2 hydrogenation on supported rhodium catalysts. *J. Catal.* **1994**, *148*, 737–747. [CrossRef]
73. Beuls, A.; Swalus, C.; Jacquemin, M.; Heyen, G.; Karelovic, A.; Ruiz, P. Methanation of CO_2: Further insight into the mechanism over $Rh/\gamma\text{-}Al_2O_3$ catalyst. *Appl. Catal. B Environ.* **2012**, *113*, 2–10. [CrossRef]
74. Bao, J.L.; Truhlar, D.G. Variational transition state theory: Theoretical framework and recent developments. *Chem. Soc. Rev.* **2017**, *46*, 7548–7596. [CrossRef]

75. Giannozzi, P.; Baroni, S.; Bonini, N.; Calandra, M.; Car, R.; Cavazzoni, C.; Ceresoli, D.; Chiarotti, G.L.; Cococcioni, M.; Dabo, I.; et al. QUANTUM ESPRESSO: A modular and open-source software project for quantum simulations of materials. *J. Phys. Condens. Matter* **2009**, *21*, 395502. [CrossRef] [PubMed]
76. Arblaster, J.W. Crystallographic properties of rhodium. *Platin. Met. Rev.* **1997**, *41*, 184–189.
77. Head, J.D.; Zerner, M.C. A Broyden—Fletcher—Goldfarb—Shanno optimization procedure for molecular geometries. *Chem. Phys. Lett.* **1985**, *122*, 264–270. [CrossRef]
78. Bengtsson, L. Dipole correction for surface supercell calculations. *Phys. Rev. B* **1999**, *59*, 12301–12304. [CrossRef]

Supplementary Material

Study of the rate determining step of Rh catalyzed CO_2 reduction: insight on the hydrogen assisted molecular dissociation

Mirko Vanzan [1], Margherita Marsili [1,*] and Stefano Corni [1,2,*]

[1] Department of Chemical Sciences, University of Padova, Via Marzolo 1, 35131 Padova, Italy; mirko.vanzan@phd.unipd.it (M.V.)

[2] CNR Institute of Nanoscience, S3-center, 213/A 41125 Modena, Italy

* Correspondence: margherita.marsili@unipd.it (M.M.) ; stefano.corni@unipd.it (S.C.);

Tel.: +39-049-8275295 (S.C.)

Details on the calculations of the interaction energy among co-adsorbed species

Let us define the following quantities:

$$E_A = E_{Rh} + E_O + E_O^{ADS} \quad (1)$$

$$E_B = E_{Rh} + E_{CH} + E_{CH}^{ADS} \quad (2)$$

$$E_C = E_{Rh} + E_O + E_{CH} + E_{CH,O}^{ADS} \quad (3)$$

$$E_D = E_{Rh} + E_{CHO} + E_{CHO}^{ADS} \quad (4)$$

Where E_{Rh}, E_O, E_{CH}, E_{CHO} represent the energy of the clean Rh slab, free oxygen, free CH and free CHO respectively; E_O^{ADS}, E_{CH}^{ADS}, E_{CHO}^{ADS} represent the adsorption energy of O*, CH* and

CHO* respectively and $E_{CH,O}^{ADS}$ is the adsorption energy of the co-adsorbed CH*/O* pair. E_A, E_B, E_C and E_D are the total energy of the systems where O*, CH*, CH/O* and CHO* are adsorbed on the Rh (100) surface, and this implicitly determine the values of adsorption energies.

By combining equations (1), (2), and (3) we recover that:

$$E_{CH,O}^{ADS} = E_C - E_A - E_B + E_{Rh} + E_O^{ADS} + E_{CH}^{ADS} \quad (5)$$

With this definition we can easily come up to the following expression for the reaction energy of the CHO* → CH* + O* process which is:

$$E_C - E_D = (E_O^{ADS} + E_{CH}^{ADS} - E_{CHO}^{ADS}) + (E_O + E_{CH} - E_{CHO}) + [E_C + E_{Rh} - (E_B + E_A)] \quad (6)$$

Notice that equation (6), which represent the reaction energy of the dissociation step, depends on three terms: the differences among the adsorption energies of O* and CH* vs CHO*; the differences among the energies of the free species O and CH vs CHO and the difference among the total energy of the co-adsorbed system vs the energy of the isolated single-molecule adsorbed systems, normalized by the energy of the free slab. The latter term is the CH*-O* co-adsorption energy.

With these equations we were able to quantify the impact of these three quantities on the reaction energies and compare the performances of the various XC-functionals, as illustrated in the main text.

Snapshots of the meaningful species involved in the PBE+U calculated NEB trajectory

In Figure S1 we reported the PBE+U calculated Nudge Elastic Bands (NEB) profile for the CO*+H* → CH* + O* reaction, labeling the notable points of the landscape with specific names. Romanic numbers refer to the species located in the energy minima i.e. the CO*/H* co-adsorbed configurations (I), the CHO* intermediate (II) and the stages where CH* and O* are co-adsorbed but have different relative positions (III and IV). Meanwhile, the label TS indicates the Transitions States. We reported a representation of the geometry configurations of these key-structures in Figure S2, while we invite the reader to watch the attached movies SM1 and SM2 for the dynamic representation of the process.

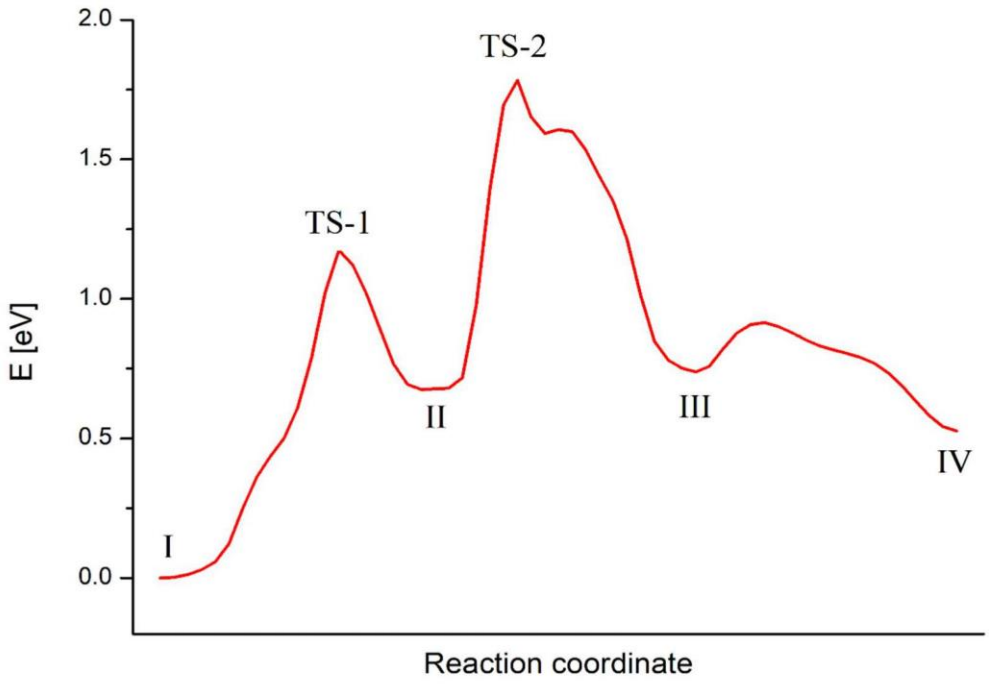

Figure S1. PBE+U computed energy profile for the whole CO*+H* → CH* + O* reaction involving CHO*. The labels, indicating the key-points intermediate of the reaction, refers to the trajectory snapshots in in Figure S2.

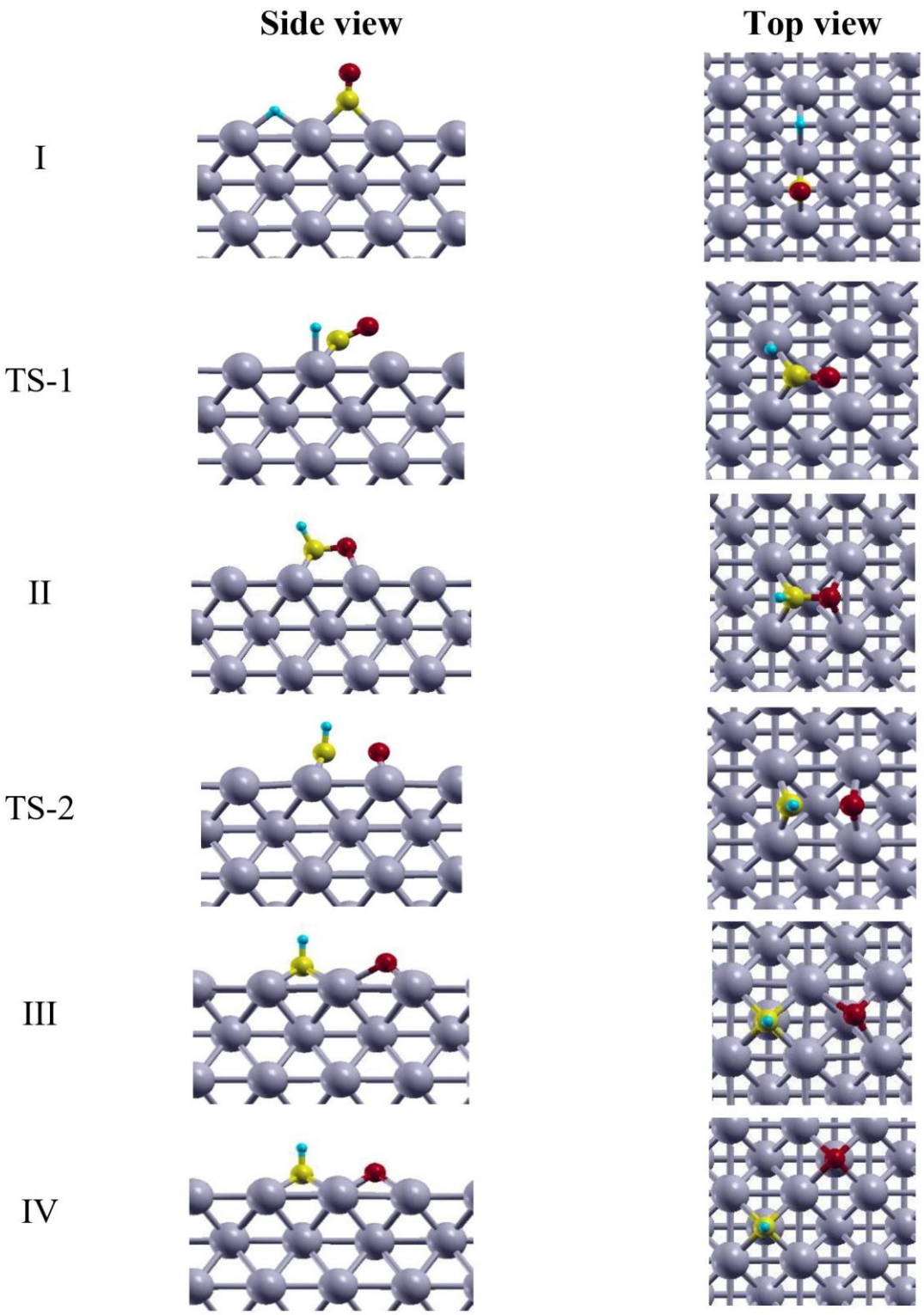

Figure S2. Snapshots of the key-intermediate of the whole CO* + H* → CH* + O* reaction, via CHO* formation. The snapshots refers to PBE+U predicted molecular configurations labeled in Figure S1. Yellow, red, light blue and grey represent C, O, H and Rh atoms respectively.

Supplementary Movie

Supplementary Movie (SM) reports the PBE+U CI-NEB calculated mechanism for the CHO* generation and dissociation. The latter process is visible after the former in the movie.
For completeness and to ease the interpretation of the results, SM is included via a Qrcode in this section.

Qrcode link for Supplementary Movie

Chapter 3. Energy transfer to molecular adsorbates by transient hot-electron tunnelling

This chapter explicitly focuses on the study of the interactions occurring between hot-electrons and molecular species in hybrid nanoparticle-molecular systems, proposing a new possible mechanism by which the carriers can promote photochemistry. This mechanism, originally proposed by Prof. P. Nordlander (Department of Physics and Astronomy, Rice University, Texas, United States), assumes the hot-electrons can transiently tunnel from the nanostructure to the molecular adsorbate, releasing part of their energy onto the vibrational motions of the molecule.

I investigated this novel mechanism by means of real-time Time Dependent Density Functional Theory calculations, contributing to the design of the nanoparticle-molecule system which are represented as silver or gold chains on which termination are attached notable target molecules.

I set-up and performed all the calculations and I was able to estimate the amount of energy that can be transiently transferred from the carriers to the molecules through this mechanism, finding how it is distributed among all possible molecular vibrational modes and highlighting its dependence on the nature of target molecule.

Moreover I provide an estimate of the effect the inelastic tunnelling of several hot-electrons can have within this framework and prove this effect could have non-negligible contribution to the whole hot-electron-molecule interaction mechanism, suggesting in turn the important role this process can have in plasmonic-driven photocatalysis.

In this chapter I summarize the main outcomes of this work starting with an introductive part and proceeding with an exposition of the adopted theoretical methodologies, a dissertation on the findings of this research and a conclusive section. Moreover, I attached an appendix containing also a movie showing the hot-electron dynamics within the silver-CO chain, which can be seen by scanning the associated QR code. This chapter will serve as a draft for a future publication.

As final remark I would like to mention that this work was conducted in collaboration with my PhD colleague D. Castaldo, Dr. G. Gil from Institute of Cybernetics, Mathematics and Physics of La Habana (Cuba), who assisted me in designing the model systems and in analysing the calculation outcomes, and Prof. P. Nordlander, who suggested the original idea behind this work with whom I held stimulating discussions that profoundly influence the line of investigation.

Introduction

Understanding and controlling the physics of light-matter interaction at the nanoscale is an indispensable step for future technologies. Knowing the microscopic mechanisms of the phenomena occurring when electromagnetic radiations interact with nanostructured objects, allows the manipulation of light and matter with extremely high precision and accuracy, thus potentially affecting many relevant technological fields such as sensing, chemical catalysis, renewable energy, communication, medicine and so on.[1–3]

Among all possible processes taking place at these scales, the activation of the Surfaces Plasmon Resonances (SPR) is one of the most peculiar and in the past decades, its theoretical comprehension gives notable outcomes such as the extremely sensible experimental techniques like Surface Enhanced Raman Spectroscopy or Plasmon Enhanced Fluorescence Spectroscopy.[4–6]

Particularly interesting and technologically relevant feature arising from the existence of the SPR in metallic nanostructures, resides in the use of the energy released by the SPR decays. Just recently, SPR decay have been thoroughly investigated unveiling a host of potential applications.[7–10] Such process can be briefly described through the following main stages. The collective oscillation of the electronic cloud starts to diphase because of its natural damping (i.e. Landau damping), resulting in the formation of several electron-hole pairs excitations that store the energy initially absorbed by the plasmons. Such non equilibrium state of excited electrons and holes rapidly thermalizes. This results in a configuration where the carriers (electrons or holes) can be described through a Fermi-Dirac distribution proper for a higher temperature with respect to the actual lattice temperature, as if the electronic system was heated up. That is why these excited particles are called “hot-carriers”. This configuration remains until the electron-phonon scattering transfers all the extra electron energy to the lattice, from where it is then further dissipated thermalizing the system to the room temperature.[11–14]

The aforementioned mechanisms for the hot-carriers production were studied in detail both experimentally and theoretically over the past years and the community agrees on the steps just described. However, there are many uncertainties regarding the way those carriers can be exploited, especially in the field of photocatalysis.[15–17] Indeed, once created, the hot-carriers may effectively interact with other systems attached to the nanoparticle, like a solid semiconductor or a molecule.[18] This interaction can then be exploited in several ways, like activating chemical reactions. To date, several groups were able to harness hot-carriers to perform different reactions, usually with higher

selectivity and rates as compared with their thermal counterpart.[19–24] It is worth mentioning that some of these hot-carrier catalyzed reactions e.g. nitrogen fixation, water splitting or carbon dioxide reduction, are extremely important from the technological point of view, especially considering the challenges set by the global warming and the climate change.[25] Hot-carriers photocatalysis can then represent a way towards a green and sustainable future.[26–29]

Despite the many advancements achieved on the experimental side concerning the characterization of these reactions, the way the hot-carriers interact with molecules and activate chemical reactions are still a matter of debates.[30–32] Focusing on the hot-electrons (HE), the two dominant theories aiming to explain their role in photocatalysis are the so called indirect and direct electron transfer. In the former approach, the HE are transferred to the Lowest Unoccupied Molecular Orbital (LUMO) of the target molecules, weakening the molecular bonds and thus reducing the energy barrier required for a bond split. In the latter view, carriers are directly transferred onto the molecule LUMO state during the plasmon dephasing and thus without passing through a proper hot-electron stage.[8,11,18] Although these mechanisms can explain a wide range of observations, they are not comprehensive of all possibilities. Indeed, according to such, the reactions occur because of the transfer of the HE on the molecule, thus ignoring the role that transient tunneling of the carriers into the adsorbate can have on the system dynamics. Moreover, as a mandatory requirement, the HE should have an energy high-enough to access the LUMO, and its wavefunction must be strongly hybridized with the molecular orbitals. These conditions imply strict limitations on the processes that may happen and preclude any role for HE with an energy not high enough to be actually transferred to the adsorbate, which are the most abundant. To date, there are a few alternative ideas to the aforementioned paradigm, involving e.g. the near field enhancement effects[33,34], or the local increases of the system temperature[35–38]; but none of them analyses the actual dynamics of HE and its interactions with molecules.

Here I aim at proposing and supporting a new and unexplored way through which the hot-carriers can interact with molecular species. In this perspective, once formed, the hot-carriers can transiently tunnel into the adsorbed species, and then return into the nanoparticle, while releasing part of its energy to molecular vibrations. This results in a sort of swing-like motion where the hot-carriers act as an external source of energy that could initiate and amplify the vibrational oscillations. Such idea was considered previously in the literature (e.g., see page 136 of ref.[32], reporting the proceedings of a recent Faraday Discussion). Moreover, a recent experimental inspections, has highlighted the primary role the molecular vibrations have in the photoactivation of chemical processes like Cu-

catalyzed H_2-D_2 exchange reaction.[39] In contrast with direct/indirect electron transfer approaches where the molecular species is intimately destabilized by the hot-carriers occupying specific molecular orbitals, here the reactions is promoted by the continuous arrival of hot-carriers and consequent energy release, weakening the bonds as the molecule is thermally excited along specific vibrations.

To test the validity of this hypothesis and theoretically estimating the magnitude of this effect, I performed a set of *ab-initio* calculations on simple atomistic models, composed of a linear chain of metallic atoms and a molecular adsorbate tethered to one of its ends (see Figure 1 as an example). In this model, the chain is a minimalistic model of a plasmonic system supporting HE propagation, and the molecule is the target adsorbate to be thermally excited by the carrier. In these simulations HE were initially confined on the terminal part of the metallic system, in the furthest site with respect to the molecule location, and then allowed to move along the chain, simulating this motion by means of real time Time Dependent Density Functional Theory (rt-TDDFT) with clamped nuclei. Figure 1 shows a graphical representation of these kind of systems, where Ag is used as metallic substrate, while a movie showing an example of the HE dynamics is given in the Appendix (Supplementary Movie SM1). By analyzing the amount of charge and the classical forces acting on the molecule as a function of time, I was able to observe the way the HE interacts with the adsorbed species, which vibrational motions are preferably activated, and how these effects depend on the energy of the HE themselves. I applied this methodology to different adsorbates (CO, N_2, H_2O) and metal substrates (Ag, Au) and this allowed to isolate the effects of the various contributions as well as to understand the role the chemical nature of atoms and bonds have in the process. Despite the simplified nature of the adopted modellistic approach, I could to develop a solid picture of the overall process with results querying many open points in the HE debates. Furthermore, these findings support recent evidences on hot-carriers mediated reactions like ammonia photocatalyzed decomposition[40–42] and suggest how HE could strongly improve the lifetime of photocatalysts in reactions like methane stream reforming.[43–45] Compared to other protocols exploited on similar systems based e.g. on the analysis of the optical responses[46–51], this method allows a simple and direct observation of the HE dynamics and gives insights of the energetics involved in the HE-molecule interaction, accounting for the effect a single injection mechanism has on the photocatalysis performances.

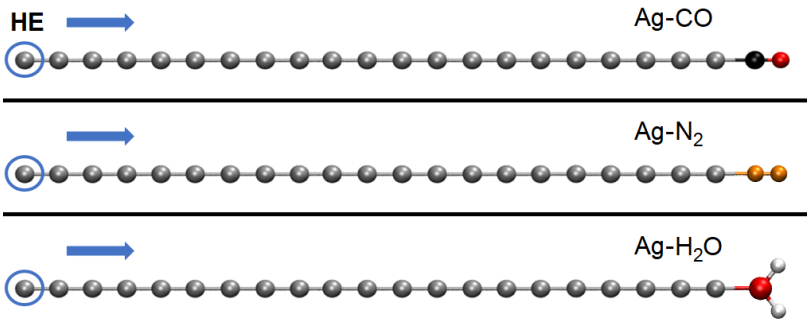

Figure 1. Schematic representation of one of the chain-molecule configurations exploited to study the HE-molecule interaction. In this case, the Ag_{21} chains represent the metal substrate and CO, N_2 and H_2O the various target molecules. Blue circles indicate the site whereas HE were initially confined, while the arrow indicates the direction of HE motion during the TDDFT simulation. Silver, black, red, orange and white balls represent Ag, C, O, N and H atoms respectively.

Computational Details and Methods

The nanostructure-adsorbate hybrid systems were described at the atomistic level through one-dimensional models. Here the plasmonic nanostructures were approximated through a 21-metal atoms chain made of Ag or Au, while as target species I chose three widespread and technologically relevant molecules, namely CO, N_2 and H_2O. This allowed to explore how HE act in well-known plasmonic metals[52–56] and interact with relevant molecules with different polarities and number of atoms. A picture representing a subset of these models is available in Figure 1. I chose to simulate a 21-atoms long chain as substrate since such length allow to represent a configuration where the existence of HE at time t=0 do not interfere with the molecule (they are separated by more than 40 Å), while being close enough to represent a likely physical situation (it is well known that the greatest part of hot-carriers are generated on the nanoparticle surface and hot-spots, i.e. generally close to the molecular species).[57] To assure the size of the system itself does not influence the calculations, I tested the replicability of the results obtained within this framework by repeating the simulations for an Ag_7-CO system and verified that I got similar results as in the case of longer chain, see the Appendix. To mimic the presence of HE coming from elsewhere in the nanoparticle, all calculations accounts for an extra electron, so that all systems were negatively charged. Before performing the electron-dynamics calculations, all considered systems were optimized at the Density Functional Theory (DFT) level using the Local Density Approximation (LDA) exchange-correlation functional and applying a Broyden–Fletcher–Goldfarb–Shanno (BFGS) optimization procedure. During the

optimization the geometry were constrained along the directions orthogonal to the chain extension to preserve the monodimensional nature of the systems. All the simulations were carried out using the package Octopus 10.4, which performs ab-initio calculations by computing the electronic density on a real-space mesh.[58,59] Both DFT and rt-TDDFT simulations were conducted on a space grid with a 0.12 Å spacing, contained within a simulation box built as the intersection of 6 Å radius spheres, each of which centered on each atom. Obtained interatomic distances for the relaxed systems are collected as Appendix in Table A1. The core electrons for the metal atoms were represented via Hartwigsen-Goedecker-Hutter (HGH) pseudopotentials[60], while for the non-metallic species I used standard pseudopotentials (psf files) as implemented in the code. The starting configurations for TDDFT simulations, namely the state where HE were confined on the terminal atom of the chain, was obtained as the ground state electronic density of systems where the pseudopotential files of the terminal atoms were modified in order to deepen the potential hole for the electrons. Such deepening of the HGH pseudopotentials were obtained by increasing the absolute values of C_1 and C_2 coefficients entering in the pseudopotential equation, defined according to the HGH equation presented in the original paper.[60] The energy of the HE was identified as the difference between the ground state energy of these "pseudo-modified" systems and the ground state energy of the optimized chains. A picture of the charge excess given by this modification is shown in the first frame of the movie SM1. The modified pseudopotential files were then replaced with the standard ones, using these out-of-equilibrium electronic density configurations representing the confined HE as the starting point of a rt-TDDFT dynamics. These states were allowed to evolve by means of rt-TDDFT using an Approximated Enforced Time-Reversal Symmetry (AETRS) algorithm, selecting a timestep of 0.01 fs and a total simulation time of 5 fs, a time window long enough to observe the HE transports and injection process, considering the length of the systems.

As first attempt I tried to perform the simulations explicitly accounting for the nuclei motion of by coupling rt-TDDFT with Ehrenfest dynamics, as implemented in the code.[58,59] However, these calculations were affected by numerical errors due to the presence of residual forces coming from the geometry optimization of the systems, which magnitude were comparable with the ones produced by the injection of a single HE.

Therefore, the estimate of the HE-molecule transferred energy was conducted by modelling the molecular species as collections of coupled harmonic oscillators and recovering the energies through the integration of the related Newton's second laws of motion, i.e. the Classical Equations

Of Motions (C-EOM). In this approach the molecular systems are represented by a set of classical particles and harmonic bonds whose masses and force constants were the ones of the atomic species (C, O, H and N) and the relative bonds (C≡O, O-H, N≡N), while the metallic atoms were considered static due to their relatively larger mass. The metal-atomic species M-X bonds (where M=Au, Ag and X=C, O, N) were also modelled considering the spring constants available in the literature. See Figure 2 for a representation of these models.

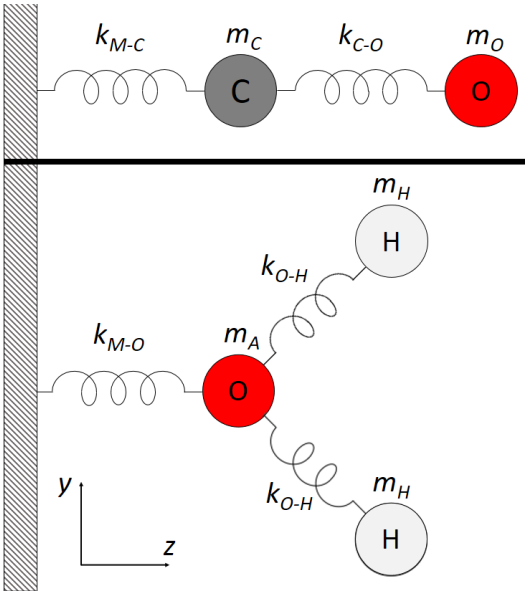

Figure 2. Graphical representation of the coupled harmonic oscillator models chosen to calculate the dynamics and energetics of the molecular systems along the simulations. Please notice that the uppermost model (CO) is analogous to the case of N_2 molecule, when masses and spring constants are properly chosen.

The C-EOM of the coupled harmonic oscillators systems were recovered by solving the Eulero-Lagrange equations for a set of Lagrangians which account for the classical kinetic and elastic potential terms associated to the various atoms.

In the case of CO species, the C-EOM for the atoms can be written as:

$$\begin{cases} m_C \ddot{z}_C(t) + k_{M-C} z_C(t) + k_{C-O}[z_C(t) - z_O(t)] = F_C^z(t) \\ m_O \ddot{z}_O(t) - k_{C-O}[z_C(t) - z_O(t)] = F_O^z(t) \end{cases} \quad (1)$$

Where m_C, m_O, are the masses of atoms C and O, k_{M-C}, k_{C-O} are the spring constants of the M-C (M=Au, Ag) bond and intramolecular C≡O bond, $z_C(t)$, $\ddot{z}_C(t)$, $z_O(t)$, $\ddot{z}_O(t)$ are the positions and accelerations of atoms C and O given with respect to their initial values, and $F_C^z(t)$, $F_O^z(t)$ are the forces acting along the z axis on C and O at time t and due to the time dependent electron density. I considered only the z-projection of the forces because, since both the metal chains and the CO molecule extend along the z axis, the forces coming from the electron density have non-zero

components along the z direction only. By a proper substitution of the parameters in equations (1), one could represent the C-EOM also for the N_2 case, since it has the same geometrical configuration of CO (see Figure 1). A complete description of C-EOM in the case of water molecule is available in the Appendix.

The coupled harmonic oscillator C-EOM have been solved numerically by means of a first order Euler integration method allowing the computation of the displacements for all the atoms. Atomic masses were collected from the latest release of the official IUPAC periodic table of elements[61] while the values chosen for the spring constants are collected in Table 1.

M	X	k_{M-X}	X-Y	k_{X-Y}
Ag[a]	C	31	C-O	1822
	N	20	N-N	2407
	O	84	O-H	813
Au[b]	C	46	C-O	1589
	N	20	N-N	2407
	O	96	O-H	796

Table 1. Spring constants for the various M-X and X-Y intramolecular bonds. M=Ag, Au; X=C, N, O and Y=O, N, H. All values are given in N/m. [a] = taken from ref.[62] ; [b] = taken from ref.[63] except for the Au-N and N-N case, which values come from ref.[62]

Here, M is the metal while X and Y are the atoms constituting the various molecules. Please notice that the spring constants in the case of M-N_2 calculations are the same for both M=Au, Ag. This because it was demonstrated that N_2 does not favorably absorb on Au and therefore an estimation of k_{Au-N} in the case of N_2 species is far-fetched.[64,65] Moreover, I encountered severe convergence problems in the optimization of the Au-N_2 geometry, since N_2 naturally tends to move away from the terminal gold atom. This prevents to obtain a proper geometry in this case and thus I chose to model the system imposing the Au-N and N-N distance as in the Ag-N_2 case, as clarified in the Appendix. Because of these reasons, I decided to chose $k_{Au-N} = k_{Ag-N}$ so that at least I could qualitatively compare the performances of the two metals toward the dissociation of this molecule. The energy transferred by HE on each vibrational motion were calculated on the basis of the atomic displacements, as the sum of the kinetic and potential energy associated to the particular vibrational motion. Considering the CO case, these quantities were defined as:

$$E_D = \frac{1}{2} m_{CO} [\dot{z_{CO}}(t)]^2 + \frac{1}{2}\, k_{M-C} [z_C(t)]^2 \qquad (2.1)$$

$$E_S = \frac{1}{2} \mu_{CO} [\dot{r}_{CO}(t)]^2 + \frac{1}{2}\, k_{C-O} [r_{CO}(t)]^2 \qquad (2.2)$$

Where E_D, E_S are the energies transferred to the desorption vibrational motions (the one involving the M-C bond) and the intramolecular C-O stretching vibrational motion respectively, m_{CO} is the mass of the CO molecule, $\dot{z_{CO}}(t)$ is the first derivative of the position of the CO molecule center of mass with respect to time, μ_{CO} is the reduced mass of the CO molecule, $r_{CO}(t)$ is the calculated intramolecular bond length defined as $r_{CO}(t) = z_C(t) - z_O(t)$ and $\dot{r}_{CO}(t)$ is its derivative with respect to time. Even here, by properly substituting the parameters in equations (2.1) and (2.2), it can be computed the transferred energies for the N_2 case. For H_2O desorption there is an analogous equation for the energy transferred to the desorption motion:

$$E_D = \frac{1}{2} m_O [\dot{z_O}(t)]^2 + \frac{1}{2}\, k_{M-O} [z_O(t)]^2 \tag{3.1}$$

On the contrary, for inner vibrations in this case the equations are slightly more complicated since the O and H relative motions can be associated to both O-H symmetric stretching and H_2O scissoring (bending) motions. Asymmetrical stretching is not accounted since transfer of energy to that motion is forbidden by the symmetry of the system. To distinguish among the two inner motions, I computed the displacement vector associated to the H_2O molecule at the DFT level, as implemented in the code Gaussian09.[66] I performed this calculation at the LDA/6-31+G* level and recovered the normalized vibrational displacement vectors for the symmetric stretching and bending motions that from now on will be called $\overline{\boldsymbol{d_S^i}}$ and $\overline{\boldsymbol{d_B^i}}$ where *i* indicates the O and H species**.** I then computed the projections of the relative atomic forces over the vibrational displacements vectors as follows:

$$F_S^i(t) = [\overline{\boldsymbol{F(t)}} \cdot \overline{\boldsymbol{d_S^i}}] \tag{3.2}$$

$$F_B^i(t) = [\overline{\boldsymbol{F(t)}} \cdot \overline{\boldsymbol{d_B}}] \tag{3.3}$$

Where $F_S^i(t)$ and $F_B^i(t)$ are the projection of the forces acting on the atom *i* over the normalized vibrational displacements related to symmetric stretching and bending respectively. I then express the obtained forces on the basis of the cartesian coordinates and used them to solve the C-EOM for water (see the Appendix section). This allowed to obtain the atomic displacements relative to the two possible motions in cartesian coordinates. The transferred energy can be calculated as:

$$E_S = \frac{1}{2}\mu_{OH} \left[\dot{r_{OH}^S}(t)\right]^2 + \frac{1}{2}\, k_{O-H} [r_{OH}^S(t)]^2 \tag{3.4}$$

$$E_B = \frac{1}{2}\mu_{OH} \left[\dot{r_{OH}^B}(t)\right]^2 + \frac{1}{2}\, k_{O-H} [r_{OH}^B(t)]^2 \tag{3.5}$$

Where $r_{OH}^{S}(t)$ and $r_{OH}^{B}(t)$ are the relative variation of the normal coordinates calculated on the basis of the atomic displacements coming from the resolution of the C-EOM system.

By integrating the electronic densities within the volume of the box corresponding to the molecule with respect to the simulation time and comparing these results with the transferred energies, I could estimate the moment in which the HE is injected in the molecule and thus the amount of transferred energy connected to its presence. The estimation of the amount of charge located on the molecule as a function of time through integration of the electronic density, were conducted as follows:

$$Charge(t) = \int_{V_m}^{a} \rho(x,y,z,t) - \rho_{GS}(x,y,z)\, dV_m \tag{4}$$

Where V_m is the volume of the cell containing the molecule defined as the volume ranging from the plane orthogonal to the z axis and bisecting the M-X bond to the terminal part of the simulation box, $\rho(x,y,z,t)$ is the electronic density of the system at time t and $\rho_{GS}(x,y,z)$ is the electronic density of the ground state of the system. To monitor the position of the HE along the chain extension in time, I calculated the Centroid Of Charge (COC) as a function of time as follows:

$$COC(t) = \frac{\int_V^a z\,[\rho(x,y,z,t) - \rho_{GS}(x,y,z)]dV}{\int_V^a [\rho(x,y,z,t) - \rho_{GS}(x,y,z)]dV} \tag{5}$$

Where V indicates the volume of the whole simulation box and z is the coordinate along the chain axis. Notice that the difference between these two densities is maximum when t=0 since here the HE confinement is maximum. The spread of the HE wave packet is the related root mean square deviation, expressed as follows:

$$RMSD\ (t) = \sqrt{\frac{\int_V^a [z - COC(t)]^2\ [\rho(x,y,z,t) - \rho_{GS}(x,y,z)]dV}{\int_V^a [\rho(x,y,z,t) - \rho_{GS}(x,y,z)]dV}} \tag{6}$$

All images, including the ones picturing the electronic densities, were produced using the VMD visualization package.[67]

Results and Discussion

The first evidence emerging from the calculations is an insight on the nature of the HE motions which in turn reflects on the interaction with the molecules. Simulations are built in order to emphasize the transient HE migrations on the region occupied by the molecule, preventing efficient carriers localization within the adsorbate orbitals. In this framework, the HE-molecule interactions cannot be properly represented as consequence of pure charge transfer processes and this allows to explore the consequences of the sole transient HE tunneling effect. From the movie SM1, visible scanning the QRcode attached in the Appendix, it can be clearly seen that as the simulation proceeds, the confined wave packet starts to spread all over the system, gradually losing the initial coherency. The evolution of the wave packet over time can be quantitatively assessed by looking at the evolution of the Centroid Of Charges (COC), representing the average location of the HE wave packet as a function of time (see Computational Details and Methods for more details).

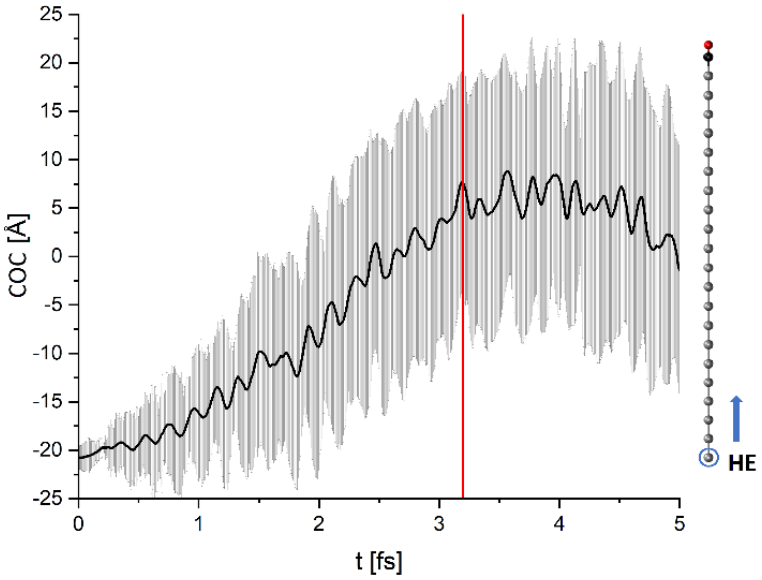

Figure 3. Time evolution of the COC(t) for the Ag-CO system when HE energy is 3.81 eV. The chain model reported on the right site serve as reference to understand the motion of COC(t) along the trajectory. Red line indicates the moment identified as the actual HE injection on the absorbed molecule (3.2 fs), according to the charge analysis in Figure 4.

In Figure 3 is reported the COC evolution for the Ag-CO system. It can be noticed that the system gradually moves from a configuration where the HE wave packet is strongly confined (t=0) to a state where the charges are homogenously distributed along the chain length. This is highlighted by the COC position, which gradually moves towards the center of the metal chain, together with the progressive increasing of the uncertainty associated with the COC position. Such kind of motion for

the COC were recovered in all cases under study (see Figure A1 in the Appendix), meaning that this type of dynamic is intimately connected with the physics behind the HE motion rather than with the chemical nature of the system. Considering the length of the chain I chose to model the metal nanoparticle (21 atoms, i.e. 44.5 Å), together with the time interval spent to reach the molecule (see Figure 3 and related discussion), I estimate an average velocity for the motion of HE of about $1.39 \cdot 10^6$ m/s, which matches the Fermi velocity of conduction electrons in bulk silver.[68] These evidences suggest that within this computational framework, the HE dynamics can be roughly viewed as a ballistically moving wave-packet which progressively loose its proper confinement as its moves within the systems. Such perspective represents a different but complementary point of view with respect to the ballistic charge-transfer paradigm, commonly adopted to describe the HE-molecule interplay dynamics.[12,57,69,70]

The moment the HE wave packet starts to interact with the adsorbed molecules can be identified by looking at the time-dependence of the molecular charge density. Indeed, the arrival of the HE induces a sensible change in the electronic density of the molecule and therefore in the amount of charge localized there. By properly integrating the electronic density of the systems (equation 4 in Computational Details and Methods section) I quantified the amount of transferred charge for a single injection process in the various cases. As shown in Figure 4, the extra charges localized on the molecule is strongly affected by the dynamics of the HE wave packet. In particular, there is a major peak around 3.2 fs (red lines in Figure 3 and 4) corresponding to the instant the interaction between HE and the species is maximum, namely the moment that can be associated to the actual HE injection. The height of these peaks, and thus the amount of transferred charges, are grow accordingly to the HE energy, as reported also in Figure A2 of the Appendix, making the injection process strongly dependent on the original HE energy. Such major spikes are not the only ones recovered along the whole trajectory, but are the sole meaningful for the study of the HE injection. Indeed, since the simulations do not account for the nuclei motions, the injected energy cannot be dissipated through electron-phonon interactions and therefore the physics occurring following this first HE injection step is unreliable. These evidences provide a new perspective on the mechanisms behind the HE-molecule injection. In parallel with the commonly accepted discrete charge transfer process paradigm[18], here I propose the HE injection can have also the effect of transiently perturb the adsorbate electronic density, indirectly activating some specific nuclei degrees of freedom and stimulating inner vibrational motions. In this scenario, energy transfer pathways involving lower energy HE are possible.

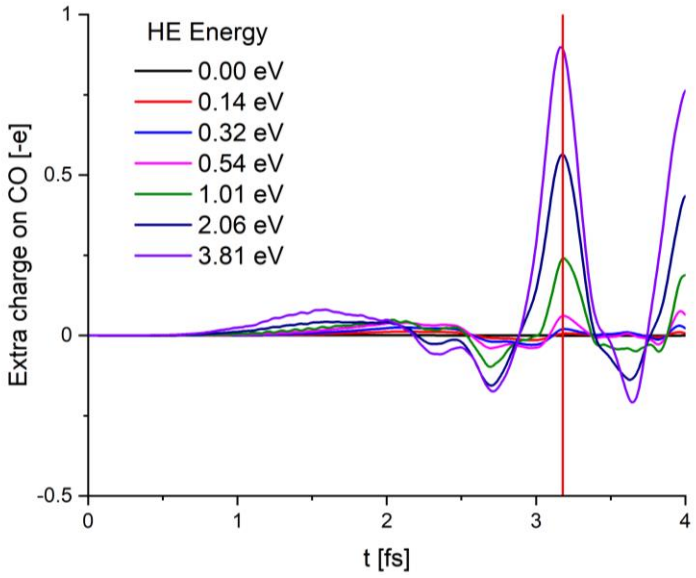

Figure 4. Amount of extra charges located on CO in the case of Ag-CO model chain systems, as function of time and HE energy. Red line indicates the moment identified as the actual HE injection on the absorbed molecule (3.2 fs)

Moreover, the presence of the smooth peaks around 1.55 fs in Figure 4, indicates that this process has a non-negligible long-range character that allows this HE-molecule interaction mechanism to take place even when most of the excited electrons are still localized within the nanoparticle. In fact, around 1.55 fs the wave packet is still moderately coherent and far from the adsorbate (COC=-9.2±10.4 Å while CO molecule is at c.a. 20 Å). However, its approach to the adsorbate produces a perturbation within the electronic systems which translates into a weak but noticeable long-range interaction, as testify by the shallow peaks shown in Figure 4. This effect could be related in principle to the size of the system and thus emerges as a computational artifact, also because it was not recovered in the simulations on shorter chains (see Figure A3 in the Appendix for more details). However, to date the long-range character of HE dynamics was already observed in some particular devices[71,72], and this could be the first time this effect and its interplay with a molecular species are observed through atomistic calculations. Another valuable aspect coming out from the simulations resides in reproducing polaronic-like effects within the dynamics. When compared to the unexcited chain, the systems accounting for the presence of the confined HE wave packet, that serve as starting configurations for the rt-TDDFT simulations, naturally include an electron-deficient spatial region surrounding the HE. Even if it is not legitimate to deem this configuration as properly polaronic (due to the lack of correlation with nuclei motion[73]), such a configuration resemble the presence of these polaronic states within the nanoparticles since show its essential feature i.e. the positively charged cloud surrounding the moving electrons, even though it arises here as a pure

electronic effect. The presence of this polaronic-like cloud can be noticed in the first frames of the dynamics, as visible from the movie SM1, as well as from Figure 4. Indeed the smooth decrease of electronic charge in the molecular region, occurring between 2.2-2.7 fs, indicates a charge withdrawing or, in an opposite perspective, the injection of positive charges. This phenomenon corresponds to the interaction between the species and the polaronic-like cloud that surrounds the arriving HE. As far as I know, this is the first study where the interaction between a polaronic-like cloud of a nanoparticle and the electronic structure of an adsorbate directly emerges from the hot-carriers dynamics and produces measurable effects on the evolution of the atomic displacements.

Once identified the exact moment in which the injection process transfers the largest amount of charge on the molecular states, I calculated the total amount of transferred energy occurring in this frame for each system as a function of the energy of the HE, distinguishing between the various vibrational motions that can be indirectly activated by the HE transient injection. The corresponding results are reported in Figure 5 and 6 (for details on the calculations see Computational Details and Methods). Figure 5 collects the results for the diatomic species CO and N_2 distinguishing between the activation of intramolecular stretching (panel A) and the nanoparticle-adsorbate vibration, namely the molecular desorption mode (panel B). The first aspect emerging from the plots is the direct proportionality among the HE energy and the amount of energy transferred to the vibrational motions of the involved molecules. This is valid for both the molecular inner stretching motion (C-O and N-N vibrations) and the metal-adsorbate desorption vibration. However, the energy transferred to the two modes are sensibly different and this has profound consequences, even though their magnitude are extremely small (within $1.2\text{-}6.5\cdot10^{-6}$ eV, I discuss the implications of these magnitudes later). As visible from the plots, for these molecules the desorption motions are preferably activated, with a desorption-to-stretching transferred energy ratio spawning from 1.9 to 3.5, depending on the system, when HE energy is within 3.5-4.0 eV. This indicates that while the HE injection could activate both vibrational modes, the great part of the energy is transferred to stimulate the molecules desorption and Au seems to give slightly better performances in this sense compared to Ag. Such evidences have different consequences, depending on the reactions considered. Taking into account e.g. the synthesis of ammonia, N_2 dissociation and fixation on the catalyst surface is a fundamental step. In this view, considering also the extremely weak bonds between the metals and N_2, using Ag or Au nanoparticles as photocatalysts seems to have more disadvantages than advantages.

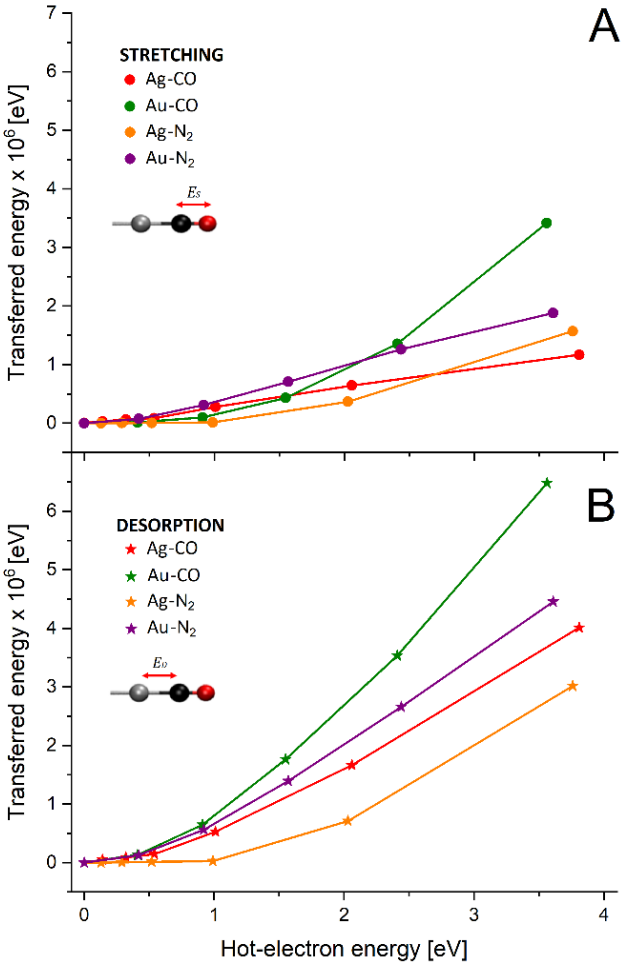

Figure 5. Estimated transferred energy per injection process, as a function of HE energy, in the case of M-CO and M-N_2 systems (M=Ag, Au). Panel A refers to the intramolecular stretching modes while panel B reports the results on the activation of the desorption modes. Inset pics denote the two possible molecular vibrational motions. Solid lines have to be used as a guide for the eye.

This is why many efforts are currently being spent in order to find effective photocatalyst for N_2 fixation that rely on other transition metals or composite materials.[74,75] However, N_2 desorption is a crucial step in ammonia decomposition reactions, which is a key-reactions in all processes that use NH_3 as a medium such as the H_2 production.[40] This reaction was demonstrated to occur with a sensibly low energy barrier if hot-carriers are involved.[41] It was speculated that among the various contribution photoexcited carriers can give to the ammonia decomposition, N_2 associative desorption plays a major role[41,42] and, using simple model, I demonstrated that the HE can actually enhance this process by stimulating the molecular detachment. On the other side, CO desorption is a remarkably important process in methane steam reforming.[43,76] Indeed, once formed CO tends to remains adsorbed on the catalyst surface and reacts with other CO molecules, forming a layer of carbon atoms that reduces the active surface thus poisoning the catalyst. Such poisoning

mechanism is known as coking.[44] This is a major problem in the case of thermally activated methane steam reforming that can be reduced using photocatalysts exploiting hot-carriers. Through simple models I demonstrated that HE selectively activate the vibration mode corresponding to CO desorption, and this could sensibly reduce the cocking rate. Therefore, using as photocatalyst plasmonic nanoparticles with high hot-carriers production rates and low affinity towards CO could give major improvements to the efficiency and sustainability of stream reforming processes. Conversely, thinking about CO_2 reduction, using as photocatalyst a surface with high CO affinity was proved to lead to highly reaction yields and selectivity towards a full reduction to CH_4 due to their role in the reaction rate-determining step.[19,77,78] These evidences suggest that CO activation could be at least partially justified by the excitations of C-O vibrational motions that, however weaker than the M-C motion, are present. Different considerations came from the analysis of M-H_2O systems (M=Ag, Au). As shown in Figure 6, even though preserved the dependence among the transferred energy and HE energy, the injection preferably stimulates the inner molecule symmetric O-H stretching. In this case the ratios with the energy transferred to desorption are 7 for the Ag- H_2O chain and 5 for Au-H_2O in the 3.5-4.0 eV HE energy window. Even larger numbers are obtained considering the stretching-to-bending ratio that, for the same HE energy interval, reach 21 and 17 for Au and Ag cases respectively. This indicates that in the presence of HE, water O-H symmetric stretching is selectively activated, and the magnitude of these transfers are sensibly higher compared to the diatomic cases, being these maximum values around $41.9 \cdot 10^{-6}$ eV and $24.1 \cdot 10^{-6}$ eV for Ag and Au respectively. Please notice that with stretching I am referring to the H_2O symmetric stretching mode, being the asymmetric stretching forbidden by the symmetry of the M-H_2O systems (see Appendix). The fact that hot-carriers can effectively activate water splitting reactions is nowadays well established[79–82] and a few computational studies were conducted to study the hot-carriers-water interaction.[48,51,83] However, they focus on the reaction mechanism involving a net charge transfer to the adsorbate. This approach allows to expand this view and suggests that the inner O-H symmetric bond stretching activation could have a crucial role in plasmonic-driven water splitting reactions. It is interesting to highlight that in all tested cases, the greatest part of the energy transferred during the injection processes translates into a kick to the atoms of the molecule which starts to move acquiring kinetic energy. The total energy transferred has two contributions namely the kinetic term, associated to the atomic velocities, and the potential term coming from the atomic displacements. In all cases, as the HE starts to interact with the species, the predominant contribution is the kinetic one, being generally 10^2-10^3 times larger than the potential.

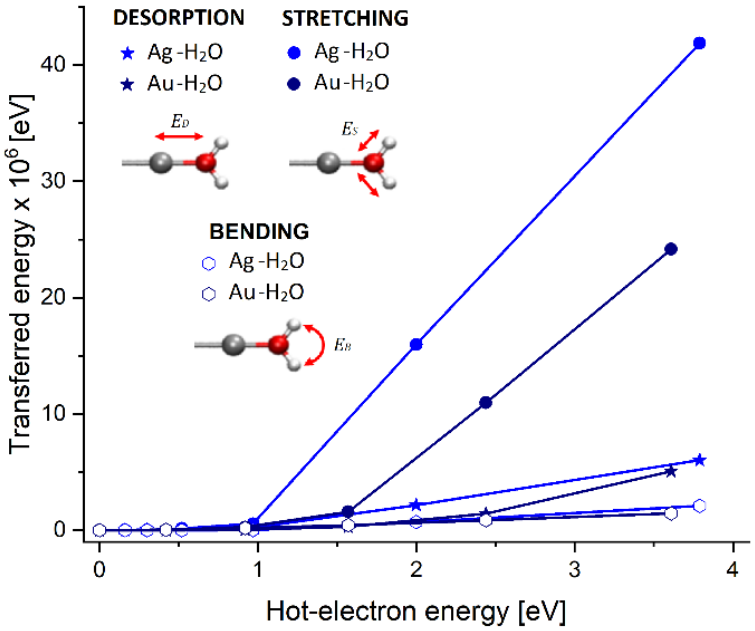

Figure 6. Estimated transferred energy per injection process, as a function of HE energy, in the case of M-H_2O systems (M=Ag, Au). Inset pics denote the three possible molecular vibrational modes. Solid lines have to be used as a guide for the eye.

This because while a single injection process does not change much the atomic positions within its small acting interval (changes are on the order of 10^{-5}-10^{-6} Å) the impinging pulse due to the HE arrival is large enough to give atoms significant velocities, which can reach about 10^{-4} Å/fs in the case of O-H bond.

The selective activation of a particular molecular vibrational motion can understood by looking at the changes in the molecular electronic density taking place during the HE injection. In Figure 7 I reported the variation of electronic density compared to its ground state electronic density, for the various systems when the charge on the molecule is maximum because of the HE injection. These quantities are calculated as the difference between the electronic densities at the moment of injection and the ground state of the same chain-molecule system. Although these two quantities account for the same number of electrons, in the ground-state there is not artificial charge confinements (see Computational Details and Methods for more details); thus a comparison between these two quantities provide a solid descriptor for the HE evolution along the dynamics. By simple visual inspection, it is clear how in all cases there is a loss of electron density in the region within the metal and the molecule, suggesting a weakening of the metal-molecule bond and thus a condition where the molecular desorption is more likely, explaining what previously noticed during the transferred energy analysis.

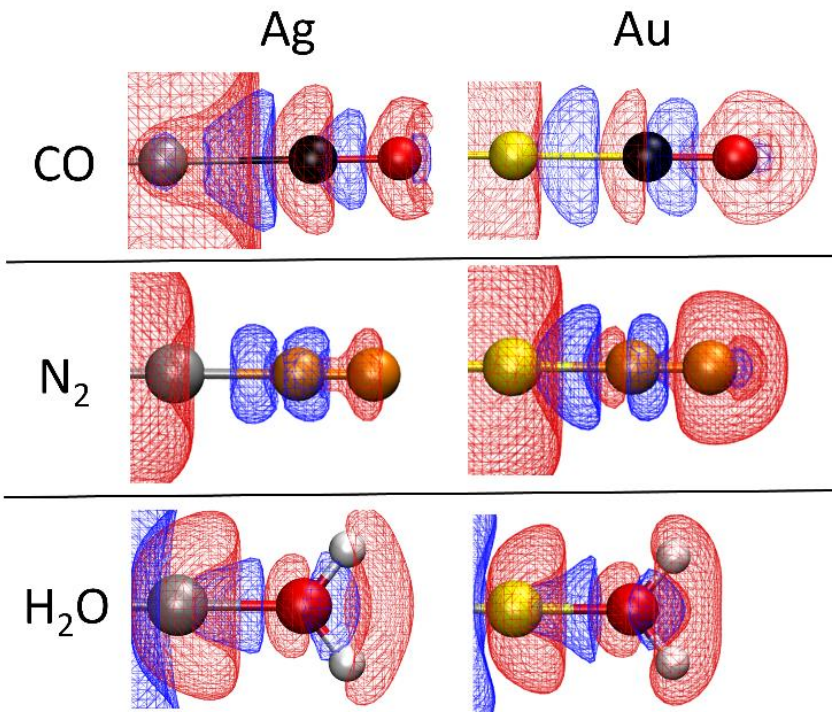

Figure 7. Excess electronic density distribution occurring during the HE injection. Red and blue wireframe surfaces represent electons excess and defect respectively. Silver, gold, black, red, orange and white balls represent Ag, Au, C, O, N and H atoms respectively. Results come from the simulations with the highest HE energy (3.56 eV and 3.81 eV for Au and Ag supported systems respectively). Isovalues=$\pm 10^{-4}$ e·Å^{-3}.

Regarding the electron density distribution within the molecule, there are minor differences depending on the system. In the case of CO, it can be noticed an electron density accumulation on top of the two atomic species, while the C-O bond results less populated by the electronic density compared to the ground state. This is valid for both Ag and Au based systems and points to a picture in which the C-O σ-bond orbital result depopulated in favor of C-O σ* antibonding orbital. This reflects the activation of the C-O stretching motion. Same considerations can be applied to H_2O where in both Ag and Au cases, electron density was drained from the O-H bond towards the atoms themselves, suggesting a weakening of the O-H bonds and thus an activation of the bond stretching. Finally, in the case of N_2, while the metal-nitrogen bond is weakened as in all other molecules considered so far, the N-N bond is actually strengthen as visible from the red wireframe surface surrounding the N-N bond that indicate increased electron population in the bond region. This confirms the low propensity of N_2 to split via this mechanism, as observed in Figure 5 panel A, and is also in line with the difficulty of performing hot-electron catalyzed reactions on N_2.[41,42]

Finally, I provide here an estimate on the entity of energy that can be stored in molecular vibrations by means of this mechanism. This is relevant to asses if it can compete or anyway supplement other photocatalytic mechanisms involving hot-carriers (such as direct and indirect electrontransfer[11,18]). As visible from the plots in Figure 5 and Figure 6, the maximum amount of transferred energy to a single vibrational mode is in the order of 10^{-5}-10^{-6} eV. Naturally such a small amount of energy would be irrelevant to promote chemical reaction. However, the energy estimated from the calculations refers to a single tunneling injection. Therefore, it can be hypothesized the existence of cumulative effects arising from multiple HE transient visits on a certain molecule, each of which contribute to excite its vibrational modes accordingly to the mechanism here studied. The total amount of energy that can be transferred considering multiple injections can be expressed as follows:

$$E_{tot} = R_{prod} \cdot P_{HE} \cdot \tau_{therm} \cdot E_T \quad (7)$$

Where $R_{prod}$is the hot-carriers production rate, P_{HE} is the probability of HE-molecule interaction, τ_{therm} is the dissipation time constant for a certain molecule vibrational mode and E_T is the energy transferred per injection event (10^{-5}-10^{-6} eV from the calculations). R_{prod} strongly depends on the shape and nature of the plasmonic device.[84,85] If equation (7) is applied in the case of a CO molecule adsorbed on a silver nanoparticle, a reasonable estimate for R_{prod} is 10^{17} s^{-1}.[53] Assuming that the CO species is adsorbed on a nanoparticle hot-spots, $P_{HE}$is around 0.5 (50% of HE are produced on the hot-spots).[52,86] A conservative estimation for τ_{therm} can be 2 ps for the Ag-CO stretching motion, even thus larger value were obtained on other metallic surfaces[87]; and lastly, from calculations E_T resulted to be around $1.6 \cdot 10^{-6}$ eV for the desorption motion in the case of the Ag-CO system when the HE energy is 2.06 eV, which is a realistic reference value for the carriers energy.[52] By solving equation (7) I recovered an estimation for E_{tot} ≈ 0.16 eV, a remarkably value large enough to excite the vibrational levels of small molecules.

For a more clear understanding of the magnitude of such value, I express this as the equivalent vibrational temperature $T_{eq,v}$, defined as the temperature at which an harmonic oscillator would have the same average total energy. With E_{tot} ≈ 0.12 eV, $T_{eq,v}$~1800K. Due to its strong dependency on the HE energy, I suggest this effect can be relevant only for carriers with energy larger than 1.00 eV. Indeed, when the HE energy is around the latter value, I obtain E_{tot} ≈ 0.04 eV and $T_{eq,v}$~340K, meaning the equivalent temperature for the Ag-CO bond is barely warmer than room temperature. However, depending on the amount of produced carriers and on the value of τ_{therm} (it can reach up to 50 ps on specific metal surfaces)[87] it can be reasonably assume that significant contribution

can be given also by carriers with energy below 1.00 eV. Though a simple estimate, these results suggest that, the hypothesis of inelastic transient electron transfer can actually provide a significant and bond selective boost to reaction rate, and represents a feasible mechanism occurring during hot-carriers mediated reactions. Of course, this mechanism does not replace other, actually it can cooperate with them to enhance the performances of the plasmonic device.

Conclusions

In this chapter I have presented first-principle simulations that provided an insight on the role the inelastic transient electron transfer can play in hot-carrier driven photochemistry. In particular, by means of rt-TDDFT, I simulated the injection of hot-electrons from the metal substrate to the molecule, to investigate the role the injection itself can have in plasmonic-driven reactions. Such simple and versatile approach returns important indications on the phenomena occurring when hot-carriers are injected in a molecule. First of all, I showed that the charge motions within the metallic system can be viewed as a wave packet moving with a ballistic motion, that allows long-range interactions among the carriers and the molecule while lose its confinement-coherence as it moves within the systems. Then I noticed that the movement of the hot-electrons are connected to the presence of a positive cloud surrounding the carriers, clearly visible from the charge dynamics, which resemble the effect a polaronic state could have towards the molecular species. Most remarkably, hot-electrons injection stimulates particular vibrational modes involving both the nanoparticle-molecule bond and the inner molecular structure. Some of the normal modes of the system are selectively activated, depending on the nature of the molecular species. In particular I found that in the case of CO and N_2, the vibrational mode corresponding to the molecular desorption is activated more than the intramolecular vibrations, while in the case of H_2O the activation of O-H symmetric stretching is largely favorite over the bending and the desorption motion. These observations follow the experimental evidences[19,41,42,77,79–81] and allow new atomistic-based interpretations of the processes occurring hot-carriers mediate reactions involving those molecules. These features were explained by an analysis of the electronic density of the systems at the time when the carriers are injected. The charge distribution clearly indicated that some bonds are weakened due to the carriers injection, suggesting in turn that they are stimulated by the energy released during the HE injection. Finally, I proposed a way to extend the observation towards a picture where several hot carriers are produced and can interact with the molecule. Accounting for

what is currently known about the rate of hot-carriers production and distribution, I estimate the vibrational excitation of particular bonds can actually have an active part in the whole photocatalytic process, being the magnitude of the energy cumulatively transferred to a specific vibration of the order of 10^{-1} eV (i.e., $\approx 10^3$ K equivalent vibrational temperature). Therefore, this effect could play a key-role in promoting chemical reactions.

Appendix

Centroid Of Charges (COC) analysis

In Figure A1 I reported the evolutions of COC with respect to the time for the tested systems. In all cases, the results refer to the simulations where the HE energy is maxima (3.81 eV in the case of Ag-N_2 and Ag-H_2O, 2.0.3 eV for Ag_7-CO and 3.56 eV in the case of Au based systems). Red lines indicate the moment in which the HE is injected in the molecule. This time is 3.2 fs in the case of Ag substrate and 2.75 fs in the case of Au-supported systems. This time difference is not related to the metal itself (the fermi velocity of Ag and Au are almost identical[68]) but to the different metal-metal bond length within the chain that makes gold-based chains shorter than the silver systems (see Table A1 in the Appendix for more details). The moments in which the injection processes occur are fully compatible with the estimations that can be made on the basis of the systems Fermi velocities. Notice that in the case of Ag_7-CO (top left panel of Figure A1), the injection takes place in a sensibly shorter time, since the chain is shorter compared to all other systems (it is made by 7 metal atoms while all others are 21-atoms long).

Transferred charge as a function of the HE energy

As mentioned in the main text, the amount of charges that transiently localizes on the adsorbate depends on the original HE energy. This is clearly visible Figure A2 where I reported the maximum amount of charge that is transferred to the CO molecule in the Ag-CO simulations, as a function of the HE original energy. The charge values are taken at 3.2 fs, which is the moment in which the HE injection occur according to the graph in Figure 3. Notice that there is a direct proportionality among the initial HE energy and the charge transferred to the adsorbate.

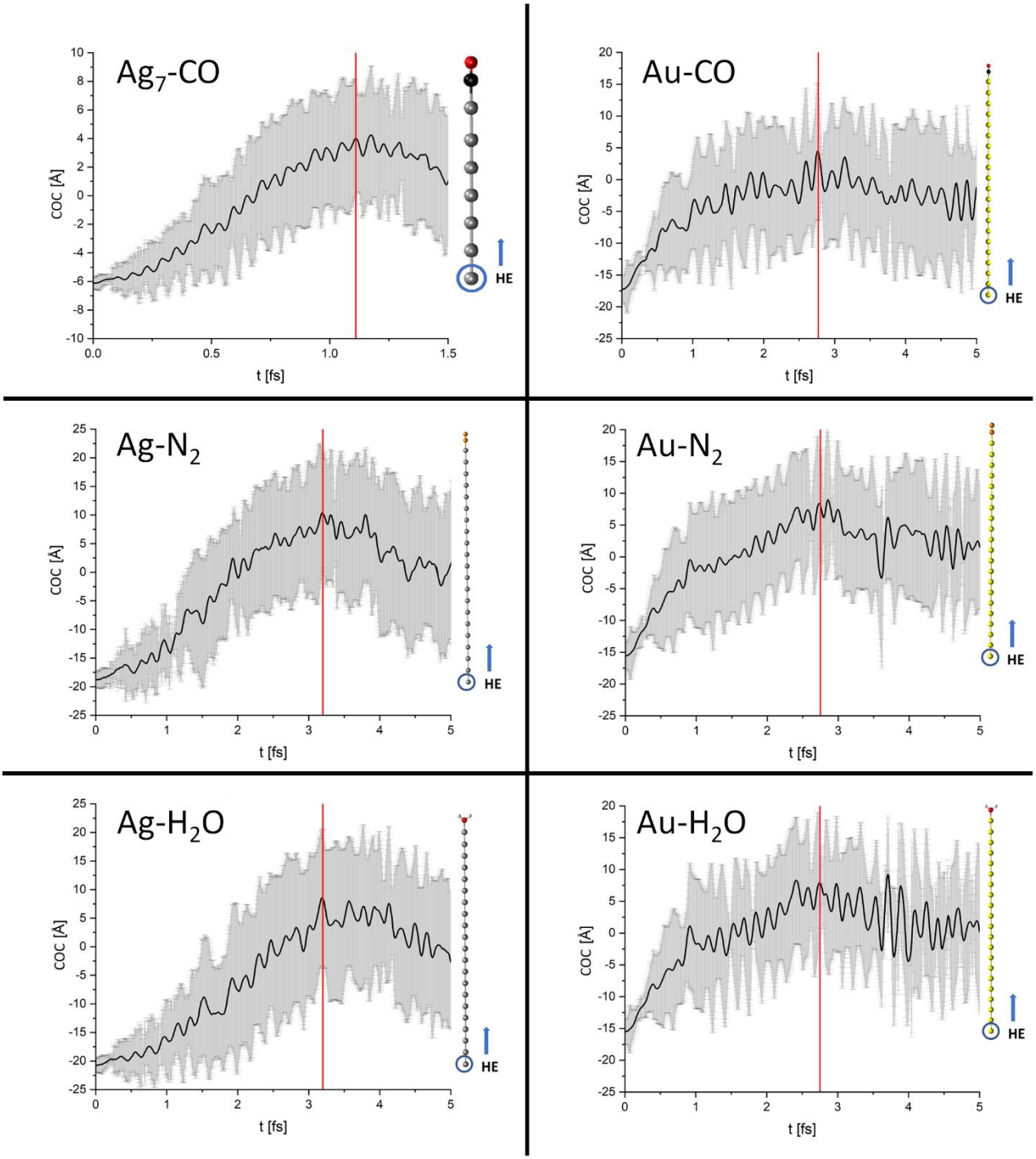

Figure A1. Centroid Of Charges (COC) analysis of all tested systems, when the energy of the adopted HE is maximum. Red lines indicate the moment in which the charge on the molecular species is maximum, namely the moment when the injection process occurs. Graphical representation of the model systems served as a guide to understand the HE wave-packet displacement along the system extension.

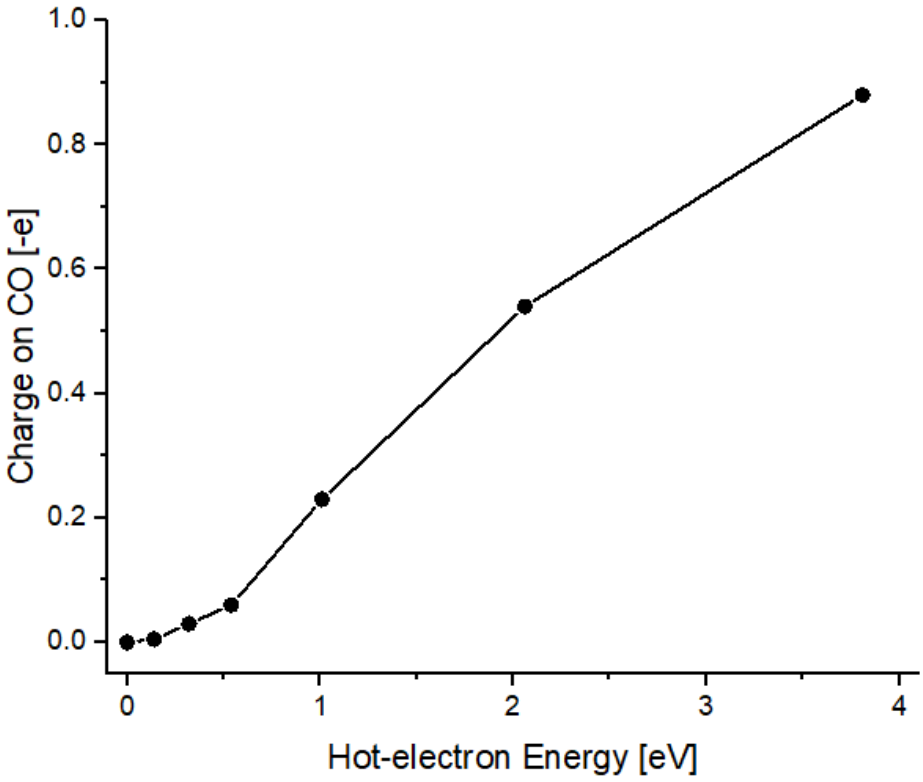

Figure A2. Amount of extra charges located on CO in the case of Ag-CO model short-chain system, as function of the HE energy. The values are taken at t=3.2 fs, namely the moment when the injection actually take place. Solid line have to be used as a guide for the eye.

Ag_7-CO results

As mentioned in the chapter, I performed the calculations on a shorter system, to assure the dimension of the chain itself does not affects the simulations results. I therefore apply the methodology to a chain-moecule system composed on a CO molecule adsorbed on a 7-atoms silver chain. The COC motion when the HE energy is 2.03 eV is pictured in Figure 1. Such HE energy was the larger we could simulate for such a small system (calculations accounting for higher HE energy did not converge). As visible from the COC trend, this follows the expected dynamics, being the HE confined on the last atom of the silver chain (around -6 Å) and gradually moving towards the other side of the system, while increasing its delocalization. The charge analysis in Figure A3 clearly measure a growing of the charge density on the molecule as the simulation proceeds, showing maxima at 1.1 fs. Considering that the chains is c.a. 13 Å long, this result is compatible with the fermi velocity of silver, as well as for the other systems.

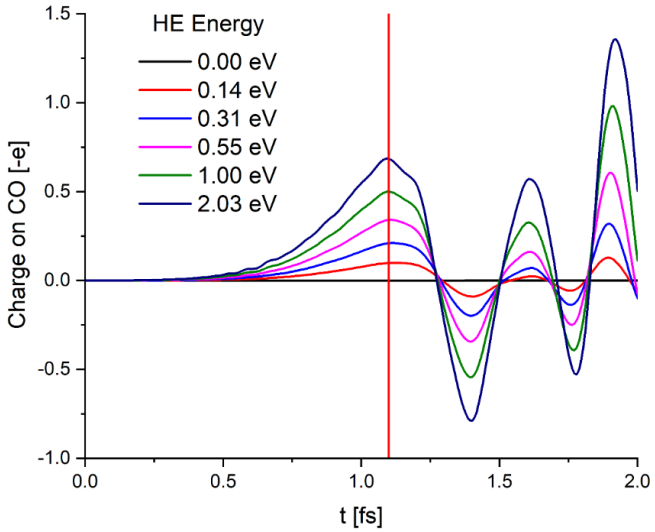

Figure A3. Amount of extra charges located on CO in the case of Ag_7-CO model short-chain system, as function of time and HE energy. Red line indicates the moment identified as the actual HE injection on the absorbed molecule (1.1 fs)

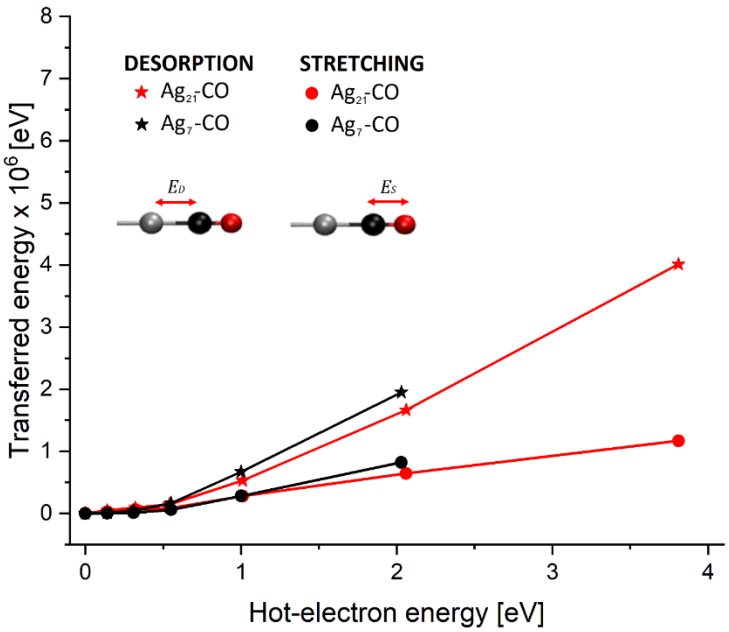

Figure A4. Estimated transferred energy per injection process, as a function of HE energy, in the case of Ag_{21}-CO (main model) and Ag_{21}-CO (short-chain model). Inset pics denote the two possible molecular vibrational motions. Solid lines have to be used as a guide for the eye.

The HE-molecule transferred energy analysis reveal a dependence on the HE energy fully compatible with what observed in the case of longer 21-metal atoms Ag-CO system, as shown in Figure A4. However, such deviations are almost negligible, suggesting that our simulations are not sensibly influenced by the choice of the chain length, at least in the 7-21 metal atoms range.

Structural and geometrical parameters

In Table A1 there are collected the structural parameters of the systems adopted in the simulations. All intramolecular bonds length are compatible with the theoretical values calculated for the species adsorbed on Ag (111)[62] and Au (111)[63] and are very similar to the ones of the free molecules in the gas phase.[88] The latter consideration remains valid for H_2O inner angle which measure 108.5° and 105.2° in the case of Ag and Au supported systems respectively.

Regarding the metal-metal distances within the chains, I found an average bond length of about 2.1±0.1 Å and 1.8±0.1 Å for Ag-Ag and Au-Au respectively. Such distances are considerably shorter than what is observed in the bulk (c.a. 2.9 Å) and in small metal aggregates.[89,90] Such an important rate of contraction could be related to the monodimensional nature of the systems since, being the atoms highly uncoordinated, they tend to get closer and assume a more compact configuration. This represents one of the main limitations of this methodology that, rather than representing a realistic system, wants to qualitatively explore the effects occurring during the HE-molecule interaction through a simple, versatile and feasible strategy.

Finally, I remark I could not recover any stable relaxed geometry for the Au-N_2 system. It is indeed well known that N_2 does not attach on gold surfaces and can only be physiosorbed.[65] Therefore I impose as reference values for the Au-N and the N-N distance the one obtained in the case of silver chains, in order to have a direct comparison on the HE performances in the two cases.

M	X	d_{M-X}	d^{L}_{M-X}	X-Y	d_{X-Y}	d^{L}_{M-X}
Ag	C	1.96	2.12	C-O	1.12	1.16
	N	1.74	-	N-N	1.08	1.09
	O	1.62	1.47	O-H	0.97	0.98
Au	C	1.53	1.36	C-O	1.10	1.19
	N	1.74	-	N-N	1.08	1.09
	O	1.72	1.76	O-H	0.97	0.99

Table S2. Bond lenght for the various M-X and X-Y bonds. M=Ag, Au; X=C, N, O and Y=O, N, H. d_{M-X} is the bond length values in our systems, while d^{L}_{M-X} are the theoretical values reported in the literature for the molecules adsorbed on the M (111) slab.[62,63] All values are given in Å.

Description of C-EOM in the case of water molecule

The Classical Equation Of Motions (C-EOM) system for the water molecule is:

$$\begin{cases} m_O \ddot{z}_O(t) + k_{M-O} z_O(t) + 2k_{O-H}[z_O(t) - z_H(t)] = F_O^z(t) \\ m_H \ddot{y}_{H_1}(t) + k_{O-H}\, y_{H_1}(t) = F_{H_1}^y(t) \\ m_H \ddot{z}_{H_1}(t) - k_{O-H}\left[z_O(t) - z_{H_1}(t)\right] = F_{H_1}^z(t) \\ m_H \ddot{y}_{H_2}(t) + k_{O-H}\, y_{H_2}(t) = F_{H_2}^y(t) \\ m_H \ddot{z}_{H_2}(t) - k_{O-H}\left[z_O(t) - z_{H_2}(t)\right] = F_{H_2}^z(t) \end{cases} \quad \text{(A.1)}$$

Where m_O, m_H, are the masses of oxygen and hydrogen, k_{M-O}, k_{O-H} are the spring constants of the M-O (M=Au, Ag) bond and intramolecular O-H bond, $z_O(t)$, $\ddot{z}_O(t)$, are the positions and accelerations of oxygen given with respect to their initial values, $z_{H_1}(t)$, $z_{H_2}(t)$, $\ddot{z}_{H_1}(t)$, $\ddot{z}_{H_2}(t)$, $y_{H_1}(t)$, $y_{H_2}(t)$, $\ddot{y}_{H_1}(t)$, $\ddot{y}_{H_2}(t)$ are the projection of the two H atoms displacements and accelerations along the z and y axis respectively with respect to their initial values, $F_O(t)$ is the force acting on oxygen and $F_{H_1}^z(t)$, $F_{H_2}^z(t)$, $F_{H_1}^y(t)$, $F_{H_2}^y(t)$ are the projections of the forces acting on the two H atoms along z and y axis respectively at time t. As pictured in Figure 1, since the M-O bond is oriented along the z axis and the molecule extends on the z-y plane, the symmetry of the system imposes that the forces coming from the arrival of HE acting on the two H atoms, have the same components on the z axis and have opposite components on the y axis, meaning $F_{H_1}^y(t) = -F_{H_2}^y(t)$.

Supplementary Movie

Supplementary Movie (SM1) reports the carrier dynamics in the case of the Ag-CO system, when the initial HE energy is 3.81 eV. The top half part of the movie represents the electronic density evolution on the plane x=0 with respect to the density of the unexcited Ag-CO system. The bottom half part of the movie reports the electronic density evolution along the z axis on the section x=0, y=0. The movie contains a reference stopwatch measuring the simulated time.

For completeness and to ease the interpretation of the results, SM is included via a QRcode in this section.

QRcode link for Supplementary Movie SM1

References

1 U. Aslam, V. G. Rao, S. Chavez and S. Linic, *Nat. Catal.*, 2018, **1**, 656–665.

2 M. L. Brongersma, N. J. Halas and P. Nordlander, *Nat. Nanotechnol.*, 2015, **10**, 25–34.

3 N. Jiang, X. Zhuo and J. Wang, *Chem. Rev.*, 2018, **118**, 3054–3099.

4 R. Pilot, R. Signorini, C. Durante, L. Orian, M. Bhamidipati and L. Fabris, *Biosensors*, 2019, **9**, 57.

5 H. Yu, Y. Peng, Y. Yang and Z. Y. Li, *npj Comput. Mater.*, 2019, **5**, 45.

6 J. F. Li, C. Y. Li and R. F. Aroca, *Chem. Soc. Rev.*, 2017, **46**, 3962–3979.

7 N. J. Halas, *Faraday Discuss.*, 2019, **214**, 13–33.

8 C. Zhan, X. J. Chen, J. Yi, J. F. Li, D. Y. Wu and Z. Q. Tian, *Nat. Rev. Chem.*, 2018, **2**, 216–230.

9 J. Gargiulo, R. Berté, Y. Li, S. A. Maier and E. Cortés, *Acc. Chem. Res.*, 2019, **52**, 2525–2535.

10 L. V Besteiro, E. Cortés, S. Ishii, P. Narang and R. Oulton, *J. Appl. Phys.*, 2021, **129**, 150401.

11 P. Christopher and M. Moskovits, *Annu. Rev. Phys. Chem.*, 2017, **68**, 379–398.

12 P. Narang, R. Sundararaman and H. A. Atwater, *Nanophotonics*, 2016, **5**, 96–111.

13 E. Kazuma and Y. Kim, *Angew. Chemie - Int. Ed.*, 2019, **58**, 4800–4808.

14 A. Manjavacas, J. G. Liu, V. Kulkarni and P. Nordlander, *ACS Nano*, 2014, **8**, 7630–7638.

15 M. Kim, M. Lin, J. Son, H. Xu and J. M. Nam, *Adv. Opt. Mater.*, 2017, **5**, 1700004.

16 Z. Zhang, C. Zhang, H. Zheng and H. Xu, *Acc. Chem. Res.*, 2019, **52**, 2506–2515.

17 L. Chang, L. V. Besteiro, J. Sun, E. Y. Santiago, S. K. Gray, Z. Wang and A. O. Govorov, *ACS Energy Lett.*, 2019, **4**, 2552–2568.

18 Y. Zhang, S. He, W. Guo, Y. Hu, J. Huang, J. R. Mulcahy and W. D. Wei, *Chem. Rev.*, 2018, **118**, 2927–2954.

19 X. Zhang, X. Li, D. Zhang, N. Q. Su, W. Yang, H. O. Everitt and J. Liu, *Nat. Commun.*, 2017, **8**, 14542.
20 S. Neatu, J. A. Maciá-Agullò, P. Concepciòn and H. Garcia, *J. Am. Chem. Soc.*, 2014, **136**, 15969–15976.
21 K. Qian, B. C. Sweeny, A. C. Johnston-Peck, W. Niu, J. O. Graham, J. S. Duchene, J. Qiu, Y. C. Wang, M. H. Engelhard, D. Su, E. A. Stach and W. D. Wei, *J. Am. Chem. Soc.*, 2014, **136**, 9842–9845.
22 H. Robatjazi, H. Zhao, D. F. Swearer, N. J. Hogan, L. Zhou, A. Alabastri, M. J. McClain, P. Nordlander and N. J. Halas, *Nat. Commun.*, 2017, **8**, 27.
23 Y. F. Huang, M. Zhang, L. Bin Zhao, J. M. Feng, D. Y. Wu, B. Ren and Z. Q. Tian, *Angew. Chemie - Int. Ed.*, 2014, **53**, 2353–2357.
24 A. Gellé, T. Jin, L. De La Garza, G. D. Price, L. V. Besteiro and A. Moores, *Chem. Rev.*, 2020, **120**, 986–1041.
25 Intergovernmental Panel on Climate Change., *IPCC's Sixth Assessment Report*, Geneva, Switzerland, 2021.
26 S. Luo, X. Ren, H. Lin, H. Song and J. Ye, *Chem. Sci.*, 2021, **12**, 5701–5719.
27 S. E. Hosseini and M. A. Wahid, *Int. J. Energy Res.*, 2020, **44**, 4110–4131.
28 C. H. Choi, K. Chung, T. T. H. Nguyen and D. H. Kim, *ACS Energy Lett.*, 2018, **3**, 1415–1433.
29 A. J. Leenheer, P. Narang, N. S. Lewis and H. A. Atwater, *J. Appl. Phys.*, 2014, **115**, 134301.
30 S. Linic, S. Chavez and R. Elias, *Nat. Mater.*, 2021, **20**, 916–924.
31 Q. Wei, S. Wu and Y. Sun, *Adv. Mater.*, 2018, **30**, 1802082.
32 J. Aizpurua, M. Ashfold, F. Baletto, J. Baumberg, P. Christopher, E. Cortés, B. De Nijs, Y. Diaz Fernandez, J. Gargiulo, S. Gawinkowski, N. Halas, R. Hamans, B. Jankiewicz, J. Khurgin, P. V. Kumar, J. Liu, S. Maier, R. J. Maurer, A. Mount, N. S. Mueller, R. Oulton, M. Parente, J. Y. Park, J. Polanyi, J. Quiroz, S. Rejman, S. Schlücker, Z. Schultz, Y. Sivan, G. Tagliabue, M. Thangamuthu, L. Torrente-Murciano, X. Xiao, A. Zayats and C. Zhan, *Faraday Discuss.*, 2019, **214**, 123–146.
33 F. Binkowski, T. Wu, P. Lalanne, S. Burger and A. O. Govorov, *ACS Photonics*, 2021, **8**, 1243–1250.
34 Y. Huang, L. Ma, M. Hou, J. Li, Z. Xie and Z. Zhang, *Sci. Rep.*, 2016, **6**, 30011.
35 Y. Dubi, I. W. Un and Y. Sivan, *Chem. Sci.*, 2020, **11**, 5017–5027.
36 Y. Dubi and Y. Sivan, *Light Sci. Appl.*, 2019, **8**, 89.
37 Y. Sivan, I. W. Un and Y. Dubi, *Faraday Discuss.*, 2019, **214**, 215–233.
38 N. Hogan, S. Wu and M. Sheldon, *J. Phys. Chem. C*, 2020, **124**, 4931–4945.
39 L. Zhou, M. Lou, J. L. Bao, C. Zhang, J. G. Liu, J. M. P. Martirez, S. Tian, L. Yuan, D. F. Swearer, H. Robatjazi, E. A. Carter, P. Nordlander and N. J. Halas, *Proc. Natl. Acad. Sci. U. S. A.*, 2021, **118**, 20.
40 T. E. Bell and L. Torrente-Murciano, *Top. Catal.*, 2016, **59**, 1438–1457.
41 L. Zhou, D. F. Swearer, C. Zhang, H. Robatjazi, H. Zhao, L. Henderson, L. Dong, P. Christopher, E. A. Carter, P. Nordlander and N. J. Halas, *Science*, 2018, **362**, 69–72.
42 V. A. Spata and E. A. Carter, *ACS Nano*, 2018, **12**, 3512–3522.
43 M. Msheik, S. Rodat and S. Abanades, *Energies*, 2021, **14**, 1–35.
44 C. H. Bartholomew, *Appl. Catal. A Gen.*, 2001, **212**, 17–60.

45 L. Zhou, J. M. P. Martirez, J. Finzel, C. Zhang, D. F. Swearer, S. Tian, H. Robatjazi, M. Lou, L. Dong, L. Henderson, P. Christopher, E. A. Carter, P. Nordlander and N. J. Halas, *Nat. Energy*, 2020, **5**, 51–70.
46 R. D. Senanayake, D. B. Lingerfelt, G. U. Kuda-Singappulige, X. Li and C. M. Aikens, *J. Phys. Chem. C*, 2019, **123**, 14734–14745.
47 L. Yan, M. Guan and S. Meng, *Nanoscale*, 2018, **10**, 8600–8605.
48 L. Yan, J. Xu, F. Wang and S. Meng, *J. Phys. Chem. Lett.*, 2018, **9**, 63–69.
49 M. Vanzan, T. Cesca, B. Kalinic, C. Maurizio, G. Mattei and S. Corni, *ACS Photonics*, 2021, **8**, 1364–1376.
50 P. V. Kumar, T. P. Rossi, M. Kuisma, P. Erhart and D. J. Norris, *Faraday Discuss.*, 2019, **214**, 189–197.
51 L. Yan, F. Wang and S. Meng, *ACS Nano*, 2016, **10**, 5452–5458.
52 L. V. Besteiro, X. T. Kong, Z. Wang, G. Hartland and A. O. Govorov, *ACS Photonics*, 2017, **4**, 2759–2781.
53 T. Liu, L. V. Besteiro, Z. Wang and A. O. Govorov, *Faraday Discuss.*, 2019, **214**, 199–213.
54 T. P. Rossi, P. Erhart and M. Kuisma, *ACS Nano*, 2020, **14**, 9963–9971.
55 O. A. Douglas-Gallardo, M. Berdakin, T. Frauenheim and C. G. Sánchez, *Nanoscale*, 2019, **11**, 8604–8615.
56 M. Berdakin, O. A. Douglas-Gallardo and C. G. Sánchez, *J. Phys. Chem. C*, 2020, **124**, 1631–1639.
57 J. B. Khurgin, *Nanophotonics*, 2019, **9**, 453–471.
58 X. Andrade, D. Strubbe, U. De Giovannini, A. H. Larsen, M. J. T. Oliveira, J. Alberdi-Rodriguez, A. Varas, I. Theophilou, N. Helbig, M. J. Verstraete, L. Stella, F. Nogueira, A. Aspuru-Guzik, A. Castro, M. A. L. Marques and A. Rubio, *Phys. Chem. Chem. Phys.*, 2015, **17**, 31371–31396.
59 N. Tancogne-Dejean, M. J. T. Oliveira, X. Andrade, H. Appel, C. H. Borca, G. Le Breton, F. Buchholz, A. Castro, S. Corni, A. A. Correa, U. De Giovannini, A. Delgado, F. G. Eich, J. Flick, G. Gil, A. Gomez, N. Helbig, H. Hübener, R. Jestädt, J. Jornet-Somoza, A. H. Larsen, I. V. Lebedeva, M. Lüders, M. A. L. Marques, S. T. Ohlmann, S. Pipolo, M. Rampp, C. A. Rozzi, D. A. Strubbe, S. A. Sato, C. Schäfer, I. Theophilou, A. Welden and A. Rubio, *J. Chem. Phys.*, 2020, **152**, 1–32.
60 C. Hartwigsen, S. Goedecker and J. Hutter, *Phys. Rev. B*, 1998, **58**, 3641–3662.
61 IUPAC, International Union of Pure and Applied Chemistry, https://iupac.org/what-we-do/periodic-table-of-elements/.
62 B. W. J. Chen, D. Kirvassilis, Y. Bai and M. Mavrikakis, *J. Phys. Chem. C*, 2019, **123**, 7551–7566.
63 Y. Santiago-Rodríguez, J. A. Herron, M. C. Curet-Arana and M. Mavrikakis, *Surf. Sci.*, 2014, **627**, 57–69.
64 K. R. Lykke and B. D. Kay, *J. Phys. Condens. Matter*, 1991, **3**, S65–S70.
65 G. Meng, R. Yin, X. Zhou and B. Jiang, *J. Phys. Chem. C*, 2021, **125**, 24958–24966.
66 M. J. Frisch, G. W. Trucks, H. B. Schlegel, G. E. Scuseria, M. A. Robb, J. R. Cheeseman, G. Scalmani, V. Barone, G. A. Petersson, H. Nakatsuji, X. Li, M. Caricato, A. Marenich, J. Bloino, B. G. Janesko, R. Gomperts, B. Mennucci, H. P. Hratchian, J. V. Ortiz, A. F. Izma and D. J. Fox, 2010, Revision B.01; Gaussian, Inc; Wallingford, CT, 201.

67 W. Humphrey, A. Dalke and K. Schulten, *J. Mol. Graph.*, 1996, **14**, 33–38.
68 N. W. Ashcroft and N. D. Mermin, *Solid State Physics*, Saunders College Publishing, 1976.
69 J. Y. Park, S. M. Kim, H. Lee and I. I. Nedrygailov, *Acc. Chem. Res.*, 2015, **48**, 2475–2483.
70 G. Tagliabue, A. S. Jermyn, R. Sundararaman, A. J. Welch, J. S. DuChene, R. Pala, A. R. Davoyan, P. Narang and H. A. Atwater, *Nat. Commun.*, 2018, **9**, 3394.
71 R. Hernandez, R. Juliano Martins, A. Agreda, M. Petit, J. C. Weeber, A. Bouhelier, B. Cluzel and O. Demichel, *ACS Photonics*, 2019, **6**, 1500–1505.
72 C. Xu, H. W. Yong, J. He, R. Long, A. R. Cadore, I. Paradisanos, A. K. Ott, G. Soavi, S. Tongay, G. Cerullo, A. C. Ferrari, O. V. Prezhdo and Z. H. Loh, *ACS Nano*, 2021, **15**, 819–828.
73 C. Franchini, M. Reticcioli, M. Setvin and U. Diebold, *Nat. Rev. Mater.*, 2021, **6**, 560–586.
74 N. Cherkasov, A. O. Ibhadon and P. Fitzpatrick, *Chem. Eng. Process. Process Intensif.*, 2015, **90**, 24–33.
75 J. Yang, Y. Guo, W. Lu, R. Jiang and J. Wang, *Adv. Mater.*, 2018, **30**, 1802227.
76 L. García, *Hydrogen production by steam reforming of natural gas and other nonrenewable feedstocks*, Elsevier Ltd, 2015, vol. 1.
77 X. Li, H. O. Everitt and J. Liu, *Nano Res.*, 2019, **12**, 1906–1911.
78 M. Vanzan, M. Marsili and S. Corni, *Catalysts*, 2021, **11**, 538.
79 H. Robatjazi, S. M. Bahauddin, C. Doiron and I. Thomann, *Nano Lett.*, 2015, **15**, 6155–6161.
80 S. Mubeen, J. Lee, N. Singh, S. Krämer, G. D. Stucky and M. Moskovits, *Nat. Nanotechnol.*, 2013, **8**, 247–251.
81 L. Mascaretti, A. Dutta, Š. Kment, V. M. Shalaev, A. Boltasseva, R. Zbořil and A. Naldoni, *Adv. Mater.*, 2019, **31**, 1–23.
82 G. Graziano, *Nat. Nanotechnol.*, 2021, **16**, 1053.
83 J. Huang, X. Zhao, X. Huang and W. Liang, *Phys. Chem. Chem. Phys.*, 2021, **23**, 25629–25636.
84 L. Yuan, M. Lou, B. D. Clark, M. Lou, L. Zhou, S. Tian, C. R. Jacobson, P. Nordlander and N. J. Halas, *ACS Nano*, 2020, **14**, 12054–12063.
85 E. Cortés, W. Xie, J. Cambiasso, A. S. Jermyn, R. Sundararaman, P. Narang, S. Schlücker and S. A. Maier, *Nat. Commun.*, 2017, **8**, 1–10.
86 E. Y. Santiago, L. V. Besteiro, X.-T. Kong, M. A. Correa-Duarte, Z. Wang and A. O. Govorov, *ACS Photonics*, 2020, **7**, 2807–2824.
87 S. Kumar, H. Jiang, M. Schwarzer, A. Kandratsenka, D. Schwarzer and A. M. Wodtke, *Phys. Rev. Lett.*, 2019, **123**, 156101.
88 CRC Handbook of Chemistry and Physics, *Structure of Free Molecules in the Gas Phase*, CRC Press, 102nd Edit., 2021.
89 R. Fournier, *J. Chem. Phys.*, 2001, **115**, 2165–2177.
90 J. T. Miller, A. J. Kropf, Y. Zha, J. R. Regalbuto, L. Delannoy, C. Louis, E. Bus and J. A. van Bokhoven, *J. Catal.*, 2006, **240**, 222–234.

Chapter 4. Exploring AuRh nanoalloys: a computational perspective on synthesis and physical properties

This chapter aims at investigating the geometrical structure and the physical properties of small (20-150 atoms) AuRh nanoalloys. Indeed, despite these systems are known to have remarkable photocatalytic capabilities, to date they are poorly investigated and there is not a consensus on the structures and arrangement assumed by those nanostructures, as well as the basic physical features. The work contained in this chapter aims to fill these gaps, exploiting Molecular Dynamics (MD) and Density Functional Theory (DFT) calculations to explore the mechanism of gold-rhodium aggregation and to study the alloys properties with ab-initio accuracy.

I actively participate in the simulations design, and performed all the calculations and data analysis. From these, I was able to extrapolate and characterise a set of notable structures differing in size and composition. The results contained in this chapter not only provide valuable information about those systems but also represent a solid ground for future insight on the comprehension of AuRh optical activity and photodynamic properties.

This chapter is divided as follows. First, I introduce the problem investigated and describe the adopted computational methodologies, then I present the outcomes of the calculations and the corresponding data analysis. Finally, I end the chapter with conclusive remarks and perspectives.

I would like to mention that I already drafted and submitted these results in the form of manuscript to the journal ChemPhysChem, as an invited contribution for a special issue dedicated to nanoalloys. It has been accepted and it is currently published on the journal website (DOI: 10.1002/cphc.202200035).

As a final remarks, I would like to specify this work were conducted in collaboration with Prof. F. Baletto from the Department of Physics of University of Milano (formerly employed at King's Collage, London), and Prof. R. D'Agosta from Department of Polymers and Advanced Materials of University of the Basque Country (Spain), and were developed in the context of a 3-months visiting period spent at the University of the Basque Country (Spain), granted to me by the European program HPC-EUROPA3 (http://www.hpc-europa.eu). Moreover, I presented the results of this project at the 3rd HPC-Europa3 Transnational Access Meeting in the form of a poster presentation and that I was awarded with the first prize for posters.

Introduction

Most of chemical's production is nowadays based on reactions catalysed by transition metals and their alloys. These catalysts usually offer high activities and recyclability, but suffer from poor selectivity and, usually, require a high amount of energy to work properly.[1] A possible way to overcome these problems is considering nanoalloys. With their reduced dimensions (less than 2 nm)and alloying metals with different properties, such ultra-small systems are characterised by strong quantum confinement effects. This is the reason for their unique properties in terms of opto-electronic features, magnetism, and catalytical capabilities.[2–6] The adaptability and the catalytic efficiency of these nanosystems can be further enhanced by alloying two or more metallic species, which structural and then electronic properties are significantly different from those of the individual constituents.[7–12] Furthermore, at the nanoscale it is possible to alloy bulk-immiscible elements giving rise to new unexplored compounds, as in the case of gold-rhodium nanoalloys. According to literature, gold and rhodium are almost immiscible in bulk: the dissolution of the metals is below 1% even when temperature reaches 1200 °K.[13,14] However, at the nanoscale Au and Rh form hybrid structures which was proved to be very effective in catalysing light-induced reactions such as hydrogen generation from water[15], oxygen evolution[16], H_2O_2 synthesis[17] and NO reduction in presence of carbon monoxide.[18,19] The AuRh nanoalloy shows also superb catalytic activity towards carbon-based compounds, as in the case of tetralin hydroconversion with H_2S[20], alkenes reduction with gaseous hydrogen[21] and CO oxidation.[22] Last but not least, it was recently shown that such system has strong bactericide action towards drug-resistant bacteria.[23] Despite the extraordinary performances and adaptability, AuRh alloy has been rarely investigated to date, mostly because batch-synthesized AuRh particles are mildly stable and tends to dissociate.[24] Most of the available data are therefore related to surface-supported systems, using as supporting materials TiO_2 or Al_2O_3. However, it was shown that such experimental setting induces phase segregation, affecting the catalytic potential which remains largely unexpressed.[20,25] Thus, finding a feasible synthetic way to obtain stable AuRh alloys that do not segregate is a crucial point that must be addressed.

To date, the computational efforts spent on the study of this nanoalloy mainly focus on the characterisation of the systems, barely accounting for its dynamics. Several studies indicate how the most stable configuration for the isolated nanoalloy seems to be the one with the rhodium encapsulated inside gold, forming a core-shell structure, in line with what can be predicted on the basis of the relative surface energy of the two components.[26] Interestingly, this feature was

recovered either in small aggregates (few dozens of atoms) and in large systems (more than 10000 atoms), using both ab-initio and classical atomistic approaches.[27–30] Despite these evidences, there is no general consensus among the theoretical and experimental communities
on which are the more favorable geometrical arrangements, how these depend on variables as the relative metal composition or the operating temperature and what is the relation between the structure and the photocatalytic properties. Indeed, very recent studies seems to undermine the net stability of core-shell pattern compared to others configurations, suggesting a hybrid mixed-Janus motif as the most favorable arrangement[31,32] while in parallel, other investigations started to shed light on the dynamics behind the synthetic process of these nanoalloys in some particular cases.[33]
To date, what appears to be certain by mixing Au and Rh is that the shapes and properties strongly deviate from the ones of pure metal systems and this mismatch can be recovered even in aggregates composed of a few atoms.[34] Moreover, it seems that in these aggregates an odd number of atoms stabilize the system and that the optimal Au:Rh ratio is around 50%.[35] This naturally prompts the question: do these evidences still apply to larger system sizes? Understanding the relative stabilities of the various isomers and homotopes[36] as a function of their size and chemical composition is a fundamental step to deeply understand their catalytic activity. To do that, it is necessary to study the formation process of the alloys using atomistic resolution and correlate the geometrical properties of the obtained structures with their physical features. I therefore conducted a computational study aimed to investigate the synthesis and the physical properties of AuRh nanoalloys in the subnanometer regime, between 20-150 atoms, by means of a multi-scale approach. I combined classical Molecular Dynamics (MD) and Density Functional Theory (DFT) simulations. The former method was applied to explore three different synthetic routes commonly adopted in the nanoalloys gas-phase synthesis, namely the one-by-one growth over a small metallic seed, the collision between nanostructures with different dimensions, and the annealing of liquid nanodroplets.[37] By analysing the evolution of the energetics along the simulations, I could identify the most favourable nanoalloy morphology and their likelihood of being formed. The latter technique was further exploited to study their physical properties and their correlation with the nanoalloys shapes, obtaining interesting connections between the nanocluster structures and features.

Computational Methods

Classical Molecular Dynamics simulations

All calculations were performed as implemented in the open-source package LoDiS[38], using the RGL protocol to describe the interatomic potential.[39,40] Such force field is well known to give reliable results when the system involve metallic atoms.[36,41,42] By means of MD I studied three different synthetic mechanisms using the following methodologies:

1) One-by-one growth: I simulated the growth of Rh over a tetrahedron Au_{20} seed (Au_{20}-Th) and of Au over various Rh seeds, namely double-icosahedron Rh_{19} (Rh_{19}-DI), truncated cuboctahedron Rh_{38} (Rh_{38}-Co) and icosahedron Rh_{55} (Rh_{55}-Ih). These structures are visible in the bottom panel of Figure 1. All simulation were conducted at 600 K, depositing one atom every 50 ns. The deposition stopped when the whole nanocluster reaches the sizes of 150 atoms. The choice of simulating Rh deposition on a gold seed in a single case come from the evidence that Au naturally tends to diffuse towards the surface and constitute the external part of the particle, losing its role as kernel.

2) Nanocluster's coalescence: I simulated the collision and further coalescence of the gold-based systems Au_{20}-Th, Au_{38}-Co, Au_{55}-Ih and Au_{75}-Co with the rhodium Rh_{19}-DI, Rh_{55}-Ih and Rh_{75}-Co nanoclusters. This allowed me to obtain and analyze the dynamics of formation of several alloyed structures which differ in sizes and compositions. The collision always occurs along the same cartesian axis, thus using the same nanoclusters impact angle. All systems were simulated for at 600 K for a total amount of 500 ns, allowing the system to relax after the impact which always takes place within the firsts 50 ns. Snapshots showing coalesced structures are reported within the graphs in Figure 2.

3) Nanodroplets annealing: I simulated the annealing process of several Au, Rh and AuRh systems. In particular I tested the following structures: Au_{55}-Ih, Au_{147}-Ih; Rh_{55}-Ih, Rh_{147}-Ih; Rh@Au core-shell 55 atoms $Au_{42}Rh_{13}$-Ih and $Au_{36}Rh_{19}$-Ih, 71 atoms $Au_{52}Rh_{19}$, 92 atoms $Au_{73}Rh_{19}$, 147 atoms $Au_{92}Rh_{55}$-Ih, $Au_{128}Rh_{19}$-Ih and $Au_{134}Rh_{13}$-Ih; Au@Rh inverse core-shell 55 atoms $Au_{13}Rh_{42}$-Ih; randomly mixed chemical ordered 55 atoms $Au_{26}Rh_{29}$-Ih; Janus ordered 55 atoms $Au_{27}Rh_{28}$-Ih. Notice that most of the chosen nanoalloys come from the simulations described in 1) and 2) while other structures were built *ad hoc* to be tested in these simulations and measure their T_m. The systems were first melted by gradually increasing the temperature and then cooled down using an

heating (and cooling) rate of 1 K/ns, which is small enough to consider the solid-liquid transitions as a reversible process and was proven to give reliable T_m within a ±50 K range.[43] The initial and final temperatures depend on each system, and are chosen in order to make the solid–liquid transition clearly visible from the excess energy data, as shown in Figure 3. Please notice that some of the mentioned nanoclusters are not explicitly treated in the discussion and not considered in the plot reported in Figure 4. This because, as mentioned in the text, some of the considered 55 atoms structures (inverse core-shell $Au_{13}Rh_{42}$, randomly mixed chemical ordered $Au_{26}Rh_{29}$-Ih and Janus ordered $Au_{27}Rh_{28}$-Ih) are highly unstable and naturally assume core-shell motifs during the initial heating, giving caloric patterns and structure similar to the core-shell cases (e.g. $Au_{42}Rh_{13}$-Ih or $Au_{36}Rh_{19}$-Ih).

Before performing the simulations, all nanoclusters were quenched through a 5 ns long equilibration. The simulations were performed through a Velocity–Verlet algorithm to resolve Newton's equation, using a time-step of 5 fs and imposing a temperature control through an Andersen thermostat with a stochastic collision frequency of $5 \cdot 10^{11}$ Hz. This protocol has already been assessed as reliable by other simulations involving metallic nanoclusters.[41,44,45] All described simulations were repeated 10 times, randomly assigning the initial value of the atomic velocities from a fixed-temperature Maxwell-Boltzmann distribution. All results I reported in this chapter are averaged over the 10 trajectories, and thus neglect spurious contributions coming from the initial conditions of the systems. Lastly, notice that most of the calculations are performed on geometrically closed shapes since they are the most energetically favourable in the case of bare metallic nanoclusters.[46]

Density Functional Theory calculations

As discussed in the Result and Discussion section, I performed ground-state DFT calculations on the most favorable geometries recovered along the MD simulations and relative isomers. These calculations were conducted at the PBE level[47] using plane-waves basis sets, as implemented in the code Quantum ESPRESSO version 6.6.[48,49] To describe the core electrons of the metal species I employed fully relativistic norm-conserving pseudopotentials. For both Au and Rh, the kinetic energy cut-off for the wavefunction and the electronic density were converged to 60 Ry and 300 Ry respectively. The various structures were relaxed through spin-polarized BFGS optimizations, assigning a non-null magnetization to both Au and Rh species of 0.5 bohr/atoms and imposing a 0.01 Ry gaussian smearing to facilitate the convergence of the electronic densities. Calculations

were performed at Γ point using a system-dependent cubic cell large enough to assure at least a 15 Å vacuum layer among a nanocluster and its replica. A subset of the structures relaxed with this approach are visible in Figure 5. The effective atomic charges assigned on each atom of the nanoalloys were calculated as $Q_{eff} = n_e - q$ where n_e is the number of accounted valence electrons for Rh and Au, while q is the Bader charge calculated through the Bader partitioning charge analysis.[50–52]

Energetics and characterisation

To characterise the thermodynamics of the trajectories and estimate the stabilities of various isomers, I defined some useful quantities that allow a characterization of the processes and systems energetics. These quantities are defined as follows:

- Excess energy: this represents the energy required to form a certain alloyed structure starting from the Au and Rh bulk phases. This quantity was proved to be a reliable descriptor for the relative stability of alloys with different sizes and compositions.[46,53,54] It is defined as:

$$E_{exc} = \frac{\left[N_{Au}E_{Au}^{coh} + N_{Rh}E_{Rh}^{coh}\right] - E_{alloy}}{(N_{Au}+N_{Rh})^{2/3}} \quad (1)$$

where $N_{Au}$and N_{Rh} are the number of Au and Rh atoms constituting the alloy, $E_{Au}^{coh}$and $E_{Rh}^{coh}$are the cohesive energy of bulk Au and Rh and E_{alloy} is the total energy of the nanoalloy, estimated classically by MD. In all cases, E_{Au}^{coh}= 3.55 eV and E_{Rh}^{coh}= 5.75 eV which are the values of cohesive energies predicted by the adopted force field.

- Binding energy: the energy gained by the systems when the atoms bind together starting from their gas phase, defined as:

$$E_{bond} = \frac{\left[N_{Au}E_{Au}^{free} + N_{Rh}E_{Rh}^{free}\right] - E_{alloy}}{N_{Au}+N_{Rh}} \quad (2)$$

where E_{Au}^{free} and $E_{Rh}^{free}$are the energy of single Au and Rh atoms in the gas phases, estimated at the DFT level. In this case E_{alloy} refers to the total energy of the relaxed nanoalloy, calculated at the DFT level.

- Mixing energy: energy gained by the systems when alloys with specific geometries are formed, compared to the pure metal nanoclusters. It is defined as:

$$E_{mix} = \frac{\left[\frac{N_{Au}}{N_{Au}+N_{Rh}}E_{Au}^{alloy}+\frac{N_{Rh}}{N_{Au}+N_{Rh}}E_{Rh}^{alloy}\right]-E_{alloy}}{N_{Au}+N_{Rh}} \quad (3)$$

where E_{Au}^{alloy} and E_{Rh}^{alloy} are the DFT calculated energy of pure Au and Rh nanoclusters at the geometry of the considered alloy. Even in this case E_{alloy} is the total energy of the relaxed nanoalloy computed at the DFT level. The ε_{mix} values collected in Table 1, are the mixing energy defined in equation (3) normalized by the number of atoms.

Finally, I want to mention that the graphical representation of all nanocluster structures were obtained using the visualization code OVITO.[55]

Results and Discussion

The first explored synthetic route was the one-by-one growth in the gas phase. Here, a nanocluster of a certain species (Au or Rh) act as a nucleation site for the nanoalloy growth which is performed by subsequent deposition of atoms of the other species. I explored the growth of Au over three different Rh seeds, namely the Rh_{19} double-icosahedron (Rh_{19}-DI), Rh_{38} truncated cuboctahedron (Rh_{38}-Co), and Rh_{55} icosahedron (Rh_{55}-Ih), while the growth of Rh atoms over gold were performed for a single seed, i.e. the Au_{20} tetrahedron seed (Au_{20}-Th). Graphical representations of these nanoclusters, as well as the excess energy trend as a function of the alloy composition and total number of atoms are collected in Figure 1. The excess energy is defined as the energy loss with respect the same amount of atoms in the bulk, roughly divided by the number of atoms at the surface (see equation 1 in the Computational Methods section). The choice of such particular seeds come from what is already known about the structure of small metal clusters which tend to generate compact aggregates with well-defined geometries. 38-Co and the 55-Ih are configurations commonly assumed by many metal aggregates,[54] while the Au_{20}-Th and Rh_{19}-DI are known stable structures for these two particular metal species.[56,57] As visible from the excess energy plots, the thermodynamic and the stability of the systems strongly depend on the size and composition. In particular, it appears that the larger the amount of gold the lower the excess energy of the alloy. This is because the bulk cohesive energy, which directly influence the excess energy as reported in

equation (1), is remarkably lower for gold compared to rhodium (c.a. 3.8 eV vs 5.9 eV)[58] and therefore larger Au:Rh ratio are characterised by smaller excess energies. The latter argument explains also why the growth of Rh over Au_{20}-Th (red line) seems to follow an opposite trend in the bottom panel of Figure 1. Notably, each line in the graphs presents a non-monotonic behavior and local energy minima. This is particularly evident in the case of Au deposition over Rh_{19}-DI (black line) where 5 local minima can be identified. These points correspond to the 5 morphologies, depicted at the bottom panel of Figure 1.

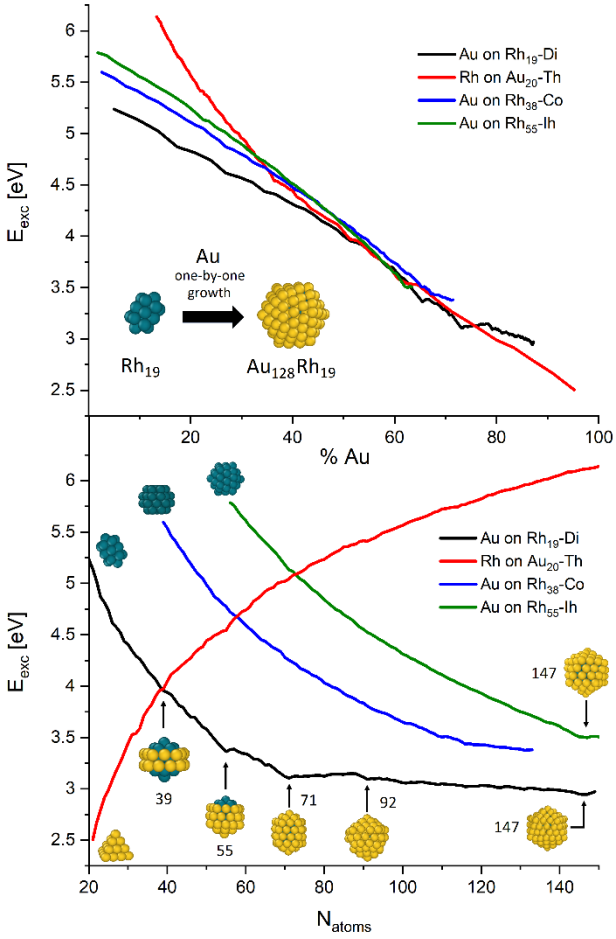

Figure 1. Excess energy as a function of composition (upper panel) and total number of atoms (bottom panel) for the AuRh formation through one-by-one growth in gas phase. Inset images at the beginning of the curves represent the starting metal seeds, while the others are schematic representations of notable structures. Blueish and yellow balls represent Rh and Au atoms, respectively. Plotted curves are averaged over 10 trajectories, error bars are omitted, curves are given within ±0.1 eV.

Those morphologies have a Rh_{19} core enclosed in a gold-shell which covering extension and motif depend on the number of Au-atoms. Among these 5 structures, the ones with lower number of atoms are worth of particular interest as they present very unusual and exotic arrangements. The 39 atoms $Au_{20}Rh_{19}$ structure is composed by an inner Rh_{19} core surrounded by an atomic gold stripe;

the 55 icosahedral $Au_{36}Rh_{19}$ system presents a ball-cup arrangement where a Rh tip emerges from the inner part of the icosahedron and the 71 atom $Au_{52}Rh_{19}$ which shows a chiral core-shell motif. For the sake of brevity from now on these clusters will be named 39-GS (gold stripe), 55-BC (ball-cup) and 71-CM (chiral motif).

At this stage of the investigation, it is worth noticing that the configuration of the Rh_{19} seed seems to play a major role in determining the formation process of those structures. While in the case of 71-CM the seed still shows a double-icosahedron symmetry, in the case of 39-GS and 55-BC, the Rh_{19} seed presents a fused icosahedron-decahedron geometry, as visible from Figure 2. I never observed the Rh-seed assuming a double-decahedron, but the Ih-Dh is similar to what recently found in ab-initio MD of Al-nanoalloys.[59] This indicates that geometrical modification can occur within the nanoalloy cores during the formation process and that these changes directly influence the stability of the whole nanoalloy and drive its growth. I will refer to this seed configuration as Rh_{19}-ID. The role the seed geometry has on the whole structure stability, together with a thorough analysis of the mentioned notable structures is given in the following section, where DFT calculations results will be presented and discussed.

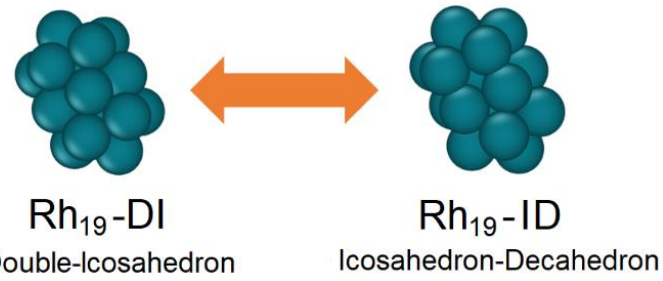

Figure 2. Graphical representation of the two configurations assumed by the Rh_{19} seed along the nanoalloys growth.

The two morphologies corresponding to the other excess energy minima in the one-by-one deposition of Au over Rh_{19} (black curve in Figure 1) corresponds to the 92 atoms $Au_{73}Rh_{19}$ and the 147 atoms $Au_{138}Rh_{19}$ respectively. These structures present more predictable and less unique shapes compared to the previous ones, since they possess complete ($Au_{138}Rh_{19}$) or incomplete ($Au_{73}Rh_{19}$) icosahedral geometries.[46] Therefore, despite these structures are marked by relative low-energy geometries, I did not include them in the examinations which is dedicated to the sole structures which due to their exotic shapes, could present notable and unique physical and catalytical properties. The discarded nanoclusters will be however taken into account in the simulations investigating nanodroplets annealing, as I will discuss later.

Focusing on the growth over the other Rh seeds (Rh_{38}-Co and Rh_{55}-Ih), the excess energy trend does not reveal any particular structure corresponding to a certain nanocluster size or composition, except for the icosahedral $Au_{92}Rh_{55}$ 147 atoms nanocluster, coming from the growth of Au over Rh_{55}-Ih which is stable due to the geometrical closure of the shell enveloping the inner seed. Lastly, the deposition of Rh atoms over a gold seed does not produces any notable structures. The mild variation of the excess energy trend in Figure 1 (red line) refers to geometries in which the gold atoms of the seed migrate toward the external surface of the nanocluster, locally smoothening the monotonical growth of the excess energy. Obtained Rh-rich systems do not produce high symmetry structures, preferring to form aggregates reminding the FCC structures of bulk rhodium. The remarkable propensity of Au atoms to migrate towards the surface notwithstanding its small diffusion coefficients[60] (it was estimated in the order of 10^{-17} cm^2/s) suggests a strong tendency to form segregated phases with Rh preferably confined within a gold shell, in line with what observed in the previously discussed simulations where the seed was made of Rh atoms. Despite the general consensus in reputing the Rh@Au core-shell arrangement as the most stable for AuRh arising from computational inspections,[27–30,61] this is the first time the arising of this chemical order is directly observed with atomistic accuracy in such small nanoclusters through MD simulations. This tendency to form alloys with this specific chemical ordering can be justified by the higher cohesive of Rh atoms compared to Au, which naturally arrange in order to minimise the exposed surface and saturate all pending bonds. Having in mind photocatalytic applications where the strong plasmonic properties of gold are combined with the catalytic capabilities of rhodium, this phase segregation could heavily affect the device performances since no Rh atoms are available to bond molecular species on the surface of the nanosystems. Thus, searching for strategies that promote synthesis of alloys rich in surface Rh content is currently a major challenge that must be faced. Simply increasing the Rh content of the alloy cannot represent a solution, since the disordered spread of the gold atoms on the surface would dramatically affect the plasmonic resonance and thus the optical properties of the system. Indeed, these would be dominated by the poor optical response of rhodium, losing the main driver for the photocatalysis. Within this framework, the presented 39-GS and 55-BC systems could represent a concrete possibility for catalytic applications since they expose Rh atoms on the surface while maintaining well-defined structures and thus specific and well distinguishable electronic transitions. For photocatalytic purposes, 71-CM could also represent a valuable candidate due to its chiral superficial texture that could bind molecules with a chiral configuration, even though the shell is made of gold atoms.

The second explored synthetic route was the coalescence between pure nanoclusters in the gas phase. The complete list of structures I chose for these simulations is available in the Computational Methods section, while the excess energy of the obtained alloys as a function of composition and dimensions are given in Figure 3. As expected, the stability of the coalesced nanoclusters directly depends on the ratio between the two metals: the higher the Au:Rh ratio, the lower the excess energy. Notably, regardless the dimension of the gold counterpart, the coalesced nanoclusters coming from the collision of Rh_{19} have the lowest excess energies and closely follow the trend recovered in the case of the one-by-one growth, included in Figure 3 as reference to evaluate the coalescence efficiency. This because, due to its small dimension, the Rh nanocluster can be fully enveloped within a gold shell and this rapidly occur in order to minimize the whole surface energy, similarly to what is observed in the one-by-one growth.

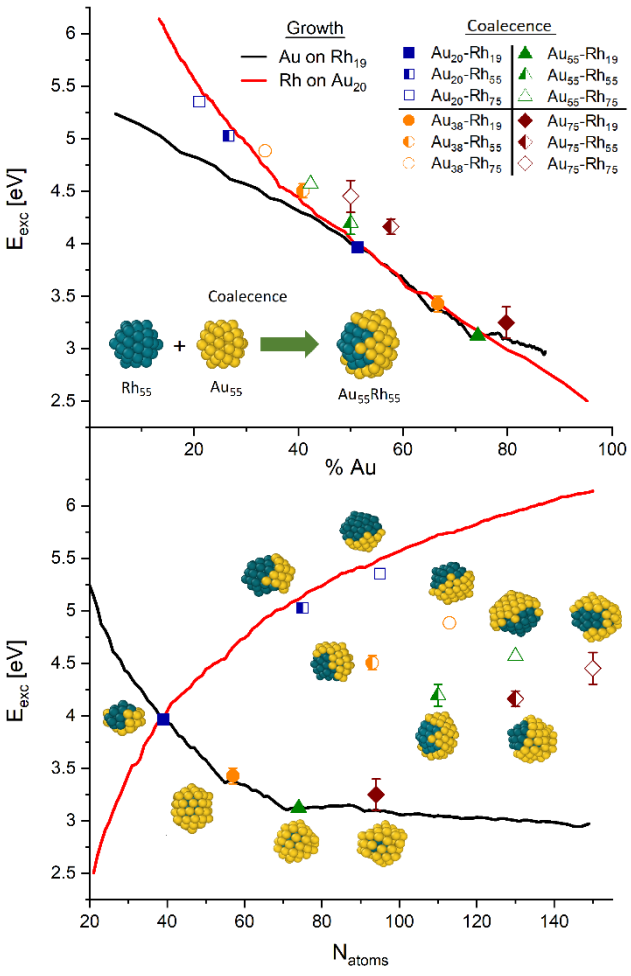

Figure 3. Excess energy as a function of the chemical composition (upper panel) and the total number of atoms (bottom panel) for the AuRh formation through coalescence (coloured symbols). For the sake of comparison, the graphs include the excess energy trends of the one-by-one growth in the case of Au_{20}-Th and Rh_{19}-DI seeds. Inset images represent the alloys recovered from the coalescence simulations. Error bars are the standard deviation of the excess energy calculated over 10 trajectories.

Apart minor differences, the structures obtained in this case have morphology which is surprisingly similar to the ones of the gold deposition over Rh_{19} seed. An interesting exception is represented by the case of the coalescence between Au_{20} and Rh_{19} which produce a nanocluster where the Rh kernel is partially covered by Au atoms, in a covering motif quite different from the one of the 39-GS case obtained during the deposition.

Despite the different structural arrangements, isomers obtained through these two synthetic approaches have practically the same excess energy, indicating the same relative stability compared to other possible shapes. This suggests that, although coalescence can produce structures energetically identical to the one of the growths over seeds in some specific cases, this technique can be used to synthesise isomers of the same nanocluster whose properties could be sensibly different from its one-by-one growth counterpart. These considerations are however valid only in some specific cases. As observable from Figure 3, most of the coalesced alloys strongly deviate from the ones of the metal deposition over a seed, either considering the growth over Au_{20}-Th and Rh_{19}-DI (red and black lines in Figure 3). Most of the simulations produce non-symmetric shapes which often are energetically higher than those obtained from the one-by-one growth at the same Au:Rh compositions (see e.g. the results concerning the coalescence of Au_{75}). In general, they have energies higher compared to the ones obtainable through metal deposition and nucleation on a seed. At finite temperatures, it is likely coalesced morphologies will evolve to those shapes obtained from the one-by-one growth. I did not consider asymmetric morphologies for further analysis. Before proceeding with the presentation of the results concerning the last explored synthetic procedure, it is interesting to highlight the natural propensity to generate Rh@Au core-shell nanoclusters where the Au atoms tends to cover the surface of the Rh counterpart as noticeable in the inset images reported in Figure 3, confirming the natural predisposition observed in the previously analysed synthetic route.

The third and last way I explored for the formation of AuRh nanoalloys is the annealing of small nanodroplets. In these simulations, some of the tested systems were collected from the trajectories of the processes already discussed, while others were specifically built for this purpose. A detailed list of the tested systems is available in the Computational Methods section. Compared to the previous synthetic approaches, this process allows the formation of the thermodynamically stable isomer for a certain nanocluster and this highlight which structures are more likely to be obtained in an experimental setup. Moreover, these simulations provide the melting temperature (T_m) of the investigated alloys, since the solid-liquid phase transition can be directly observed from the trend

of the excess energy as function of the temperature in both melting and subsequent freezing processes. An example of this plot is given in Figure 4 where the excess energy for the 55 atoms core-shell $Au_{42}Rh_{13}$ icosahedral nanocluster is given as function of temperature, in both processes. In this case, the systems present a phase transition which begins at 1000K and terminate around 1200K, leading to a liquid nanodroplet. I define the T_m of the nanocluster as the inflection point of the functions which in this case falls around 1100K. The overlap of the two lines referring to the melting and freezing processes indicates that the transition is thermodynamically reversible and that the geometries recovered from the solidification, i.e. the thermodynamically stable isomer of the alloy, coincide with the nanocluster initially melted.

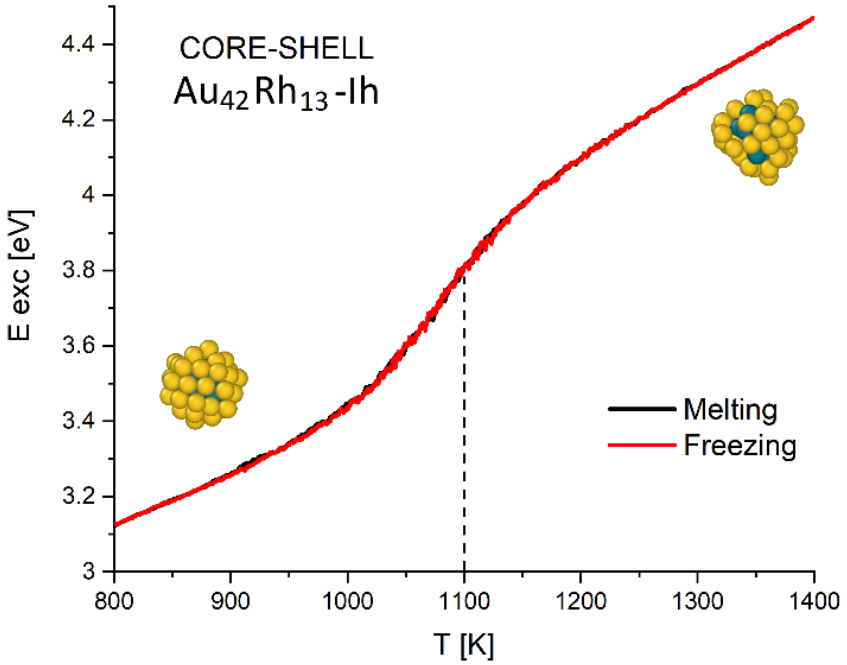

Figure 4. Caloric curves for core-shell $Au_{42}Rh_{13}$ nanocluster for both melting and freezing processes. Inset images represent the alloy conformation at 800K and at 1400K.

As a general trend, I recover that all investigated nanoalloys present excess energy trends similar to the ones of Figure 3. However, there were specific cases where the plots show discontinuities and non-monotonical trends for the excess energy dependence on the temperature. This is especially the cases for the systems I built to study the stabilities of Janus, inverse core-shell, and randomly mixed chemical ordering. The uncommon tendencies of their excess energy indicate large instabilities and testify the presence of phases transition toward the Rh@Au core-shell chemical order even below 300 K, thus highlighting the high instabilities of these arrangement compared to the core-shell one.

Apart from these cases, most of the investigated nanosystems present annealing patterns that confirm the thermodynamical stability of the structures annealed, presenting no mismatches

between the excess energy trends for the melting and freezing simulations and well-defined T_m. Dynamically, it appears that the solid-liquid transition is generally driven by the integrity of the gold shell. In the case of melting process, as the temperature approaches the T_m, the atoms constituting the Au shell starts to vibrate and diffuse, losing a coherent motif while the inner Rh seed remains compact. As the temperature exceeds T_m, the rhodium kernel starts to lose its structure and gradually melts. This phenomenon, always observed in the systems, can be interpreted on the basis of the following considerations. First, T_m for gold is sensibly lower than the one of rhodium (1337K vs 2237K in the bulk phase[62]) indicating a weaker temperature stability for gold structures. Secondly, rhodium core is usually enveloped within the gold shell in a compact shape where the atom coordination numbers are generally higher than the ones of the gold atoms constituting the shell. Therefore, the binding energy per atom is higher for Rh than Au. This does not mean the Rh kernel do not play an active role in the process. In the case of 71-CM, for example, the rotational motion of Rh_{19}-DI seed is activated by the temperature, allowing a continuous swap between Rh_{19}-DI and Rh_{19}-ID shapes, whose graphical models are presented in Figure 2. A plot showing the T_m as function of the cluster sizes and metal contents for the investigated nanoalloys is available in Figure 5.

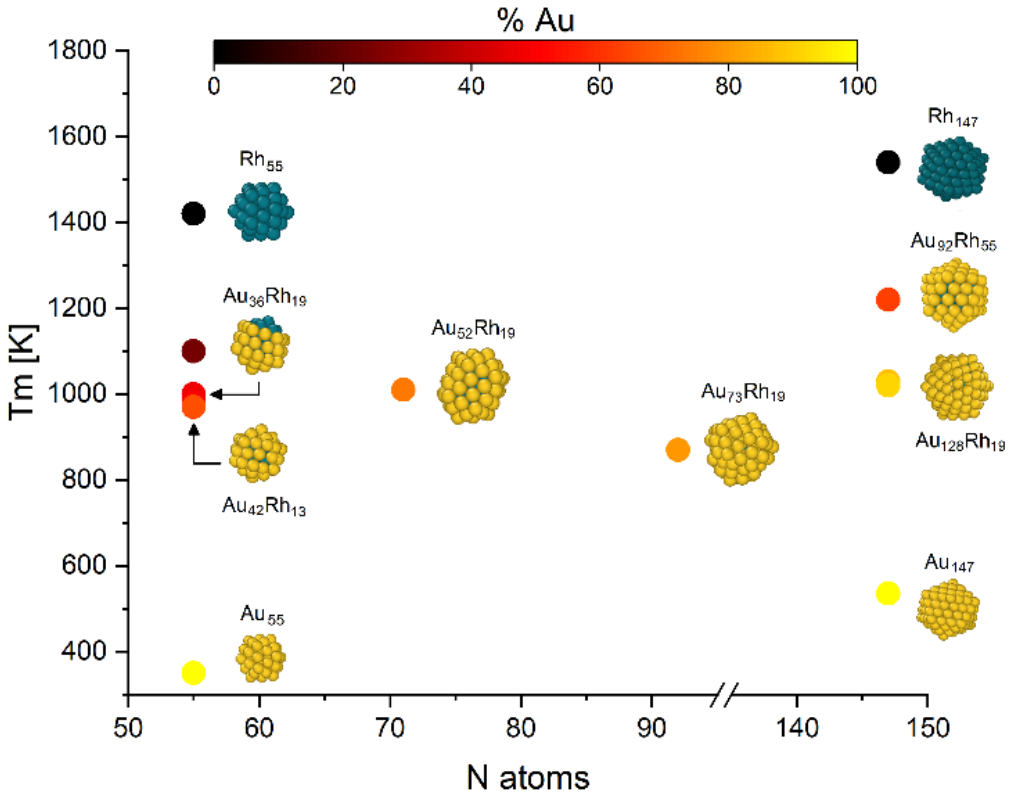

Figure 5. Melting temperatures of the investigated nanoalloys, as a function of size and metal content. The images are graphical representations of the particular systems. T_m are given within a confidence interval error of ±50K.

Pure Au and Rh icosahedral structures made on 55 and 147 atoms were included in the analysis as benchmark to evaluate the features of the nanoalloys. As expected, the T_m of systems owning the same number of atoms (e.g. when N=55, 147 in Figure 5) locate between the values identified for the pure nanoclusters. This proves that T_m is a multifactorial function that depend on both system size and composition. Such dependencies are however not so trivial as could be thought in the first place. It is indeed surprising how the T_m of 71-CM is 140K higher than the one of the 92 atom structure $Au_{73}Rh_{19}$. Such temperature difference is too large to be justified on the basis of the sole difference in metal content which is indeed quite moderate (73% of Au content for 71-CM vs 79% in the case of $Au_{73}Rh_{19}$) and anyway is not coherent with the fact that the 147 atoms $Au_{128}Rh_{19}$ present a higher T_m compared to $Au_{73}Rh_{19}$. Furthermore, all those structures arise from the same synthesis, and thus this peculiar T_m behaviour cannot be related to differences in chemical ordering or nanoclusters inner morphology. The explanation of this phenomenon must lie elsewhere. Thinking about the relative structures stabilities it can be noticed that the 71-CM and the $Au_{128}Rh_{19}$ nanoclusters possess remarkable energetic stabilities given by the geometrical closure of the gold shell surrounding the inner part of the system. Being stacked within a well-defined texture, the gold atoms have a high kinetic diffusion barrier and texture is less affected by the enhanced thermal vibrations. On the opposite side the superficial atoms of $Au_{73}Rh_{19}$ are not constrained within any particular motif and further suffer from low-coordinated Au atoms, making them more sensible to the increasing of temperature.

Another interesting aspect that emerges from the analysis of T_m is that all nanoalloys shows remarkably high thermal stabilities. There are nanoalloys like 55-BC with remarkably high T_m (around 1000K), which is an outstanding value for a 55 atoms aggregate. The case of 147 atoms structure is even more surprising. Even though some of them have a very low Rh content (e.g. around 13% in the case of $Au_{128}Rh_{19}$), the T_m are still impressive being located around 1000K. This indicates that even a small amount of Rh can heavily modify the physical properties of these systems and influence their thermal stabilities. This in turn suggests that a Rh doping of gold structures could effectively increase the thermal stability of the system and extend the range of temperature in which gold-nanostructured devices can be applied, potentially leading to important improvements in technologically relevant applications.

These latter observations, which are here based on a theoretical approach to the problem, follows what is experimentally known about the thermal stabilities of these nanoalloys. In a work from 2017, Shubin et al. studied the formation and stability of gold-based nanoalloys exploring also the AuRh

system.[33] Despite the investigated sizes and compositions were slightly different from the ones of my nanosystems, their analysis reflects what I observed in the simulations. High Temperature Synchrotron X-Ray Diffraction techniques revealed that AuRh nanoalloys have a remarkable thermal stability (even though smaller than the ones I observed) and the authors suggested this is due to the slow kinetics of rearrangements which require large amount of thermal energy to be activated. My simulations are compatible with the experimental observations on the impressive thermal stabilities and the high kinetic energy barriers, while highlighted the importance of the latter and its connection with the geometrical arrangements of the atoms. I indeed recover a non-monotonic trend in the size dependence of T_m, which I related to the structures of the alloys themselves and their structural closure. To conclude this section on the results of MD simulations, I want to comment and integrate the synthetic mechanism Shubin et al. proposed their work. From the data obtained through X-Ray Diffraction, they proposed the synthesis of AuRh could occur through a *conversion chemistry* mechanism where Au seeds act as nucleation spots for Rh growth, which gradually migrates towards the inner part of the structure as the sizes increase.[33] The experimental conditions indeed forced the synthesis to proceed that way and it was demonstrated to generate thermally stable nanoclusters. However, the melting temperature recovered by the authors are sensibly smaller compared to the ones I predict in The simulations, being around 700-800K for nanoparticles with sizes around 5 nm. In my opinion this is due to the chosen synthetic procedure (Rh nucleation over Au seeds), which I demonstrated is not the most suitable for these kinds of nanoalloys, leading to relatively unstable systems. On the contrary, performing the growth the opposite way i.e., by depositing Au onto Rh seeds could bring to structures with higher thermal stabilities, lower topological disorder and could lead to a more accurate atomic species distribution, selectively producing minimum energy alloy isomers.

In the second part of this chapter, I deepen the insights on some specific AuRh structures and investigate their features by means of DFT. I focused the treatment on the formerly described 39-GS, 55-BC and 71-CM nanoclusters since their exotic shapes together with their remarkably relative stability makes them good potential candidates for photocatalytic applications. Each of the mentioned cases were studied in two different shapes. As noticed in the one-by-one growth simulations, the geometry of the inner Rh seed seems pivotal to determine the structure and stability of the nanoalloys. I therefore investigated the mentioned alloys taking into account two different isomers, namely Rh_{19}-DI and Rh_{19}-ID. I furthermore extend the calculations on the pure forms of metal structures, i.e. on Rh_{19}, Au_{20}-Th, Rh_{55}-Ih and Au_{55}-Ih. The data recovered from the

Name	Shape	d_{Au-Au} [Å]	d_{Rh-Rh} [Å]	d_{Au-Rh} [Å]	E_{bond} [eV]	ε_{mix} [eV]	M [μ_B]	H-L [eV]
39-GS	DI	2.80±0.02	2.72±0.17	2.77±0.10	3.419	0.297	0.07	0.03
	ID*	2.88±0.07	2.71±0.07	2.82±0.07	3.423	0.255	0.64	0.14
55-BC	DI	2.85±0.08	2.74±0.08	2.80±0.08	3.303	0.178	0.18	0.15
	ID*	2.89±0.04	2.69±0.05	2.81±0.04	3.307	0.146	0.32	0.16
71-CM	DI*	2.87±0.04	2.71±0.06	2.80±0.05	3.213	0.186	0.18	0.11
	ID	2.85±0.04	2.70±0.06	2.79±0.05	3.194	0.181	0.22	0.08
Rh_{19}	DI*	-	2.67±0.04	-	3.888	-	0.55	0.08
	ID	-	2.63±0.08	-	3.876	-	0.41	0.18
Au_{20}	Th	2.81±0.10	-	-	2.360	-	0.00	1.79
Rh_{55}	Ih	-	2.65±0.06	-	4.489	-	0.54	0.10
Au_{55}	Ih	2.84±0.07	-	-	2.527	-	0.00	0.65

Table 1. Data collected from DFT calculations performed on various pure and alloyed nanostructures. Here *d* indicates the average bond length between nearest neighbour for the couple of species indicate as subscript, E_{bond} and ε_{mix} are the bonding and mixing energy, *M* is the average magnetisation per atom and H-L indicate the energy of the HOMO-LUMO gap. Errors associated to d are calculated as the standard deviation of the sets. * stands for the classical predicted lowest energy isomer.

DFT calculations are collected in Table 1. Starting from the systems energetics, the nanoclusters isomer which resulted energetically favoured from the MD simulations still resulted the most favourable structures in the DFT simulations. This is confirmed by the values of the bonding energy E_{bond} which are always higher for the isomers recovered through MD (marked with * in Table 1) compared to the counterpart. However, the relative stability between the two isomers is not constant and seems to increase as the gold shell covers the inner seed. The energy separating the two isomers are 0.16 eV, 0.24 eV and 1.36 eV for 39-GS, 55-BC and 71-CM nanostructures, respectively. This clearly suggests that the higher the constraining given by the gold enveloping, the more difficult is for the seed to retain a certain configuration.

Energetically speaking, there is also a net energy gain in forming the alloy compared from the pure nanoclusters, as confirmed by the positive values of the mixing energy ε_{mix}. This in turn indicates that the production of those systems should be an exothermic process which occurs spontaneously and could in principle catalyse the production of isomers with similar energy, if the kinetic energy barrier for isomers transition is small enough. The geometrical analysis of the DFT relaxed nanoalloys reveals interesting trends for the nearest neighbour interatomic distances. At first, the data demonstrate that as the size of the system increases, the average Au-Au bond length increases and get closer to the bulk reference value of about 2.88 Å.[63] This phenomena is well known to take

place in small metal aggregates, where the average bond length is shortened compared to the bulk because of the lower coordination number of the superficial atoms, which tend to compensate the pending bonds by reducing their relative distance. Even Rh-Rh couples follow the same trend, especially if the average distances of the nanoalloys are compared with the ones of the pure Rh_{19} seeds. This however is not connected to a larger number of Rh constituting the nanocluster, since the seeds always have the same number of atoms; indeed this effect arises from the sole covering effect given by Au, which stimulates an elongation of the Rh-Rh bonds, allowing them to approach and reach the bulk value of 2.69 Å.[63] As far as I know, this is the first time this stimulated bond elongation given by the shell enveloping is observed in AuRh nanosystems. Finally, Au-Rh bonds are not sensibly affected by the size of the nanoalloys since their values remain always within the same confidence interval.

The most remarkable differences involving DI and ID isomers are the ones relative to the magnetic moment per atom and to the energy gap between the frontier orbitals, namely the HOMO-LUMO gap. Simulations reveal that two isomers, which I remember differs for the sole rotation of the Rh seed, can have heavily different magnetic moment. According to the simulations, 39-GS nanocluster in its DI form has an impressive magnetic moment per atom and remarkable large HOMO-LUMO gap compared to its DI shaped counterpart. This suggests that small geometrical changes of the Rh seed could reflect into massive changes of the systems physical features and therefore, on its potential technological applications. Same considerations can be applied to the other analysed alloys and even on the Rh_{19} seed itself whose geometrical configurations strongly affect its electronic properties (see Table 1).

Since I am interested in characterising the optical and photophysical dynamics of these systems, I searched for the existence of charge unbalances within the structures which could reflects to the existence of optically active charge transfer transitions. The analysis of the charge distribution within the most stable isomers is given in Figure 6. Take into account that the charge excesses and loses are given with respect to the number of electrons possessed by the single atomic species, as specified in the Computational Methods section. From the pictures collected in Figure 6, it can be clearly noticed the existence of a strong charge separation between Rh and Au atoms. In particular, gold atoms naturally withdraw electrons from rhodium, resulting in a partially oxidised configuration where Rh atoms can lose up to 0.2 electrons. Such an important charge unbalance directly arises from the electrochemical processes occurring at the Au-Rh interface which lead to a net electron transfer from rhodium to gold due to its lower electrochemical reduction potential. The

presence of partially oxidised Rh atoms in the external part of the clusters (in the case of 39-GS and 55-BC) could lead to interesting photocatalytic processes. Indeed, simple coulomb interactions could favour the adsorption of electron rich molecules on top of these sites. Then by optically stimulating charge transfer transitions within the alloy, these adsorption points could easily take part to the optical activity and this in turn would probably affect the vibrational and/or the electronic structure of the adsorbed molecule, activating chemical reactions. Such a mechanism could also involve the generation of hot-carriers as already proposed for these nanoalloys.[15]

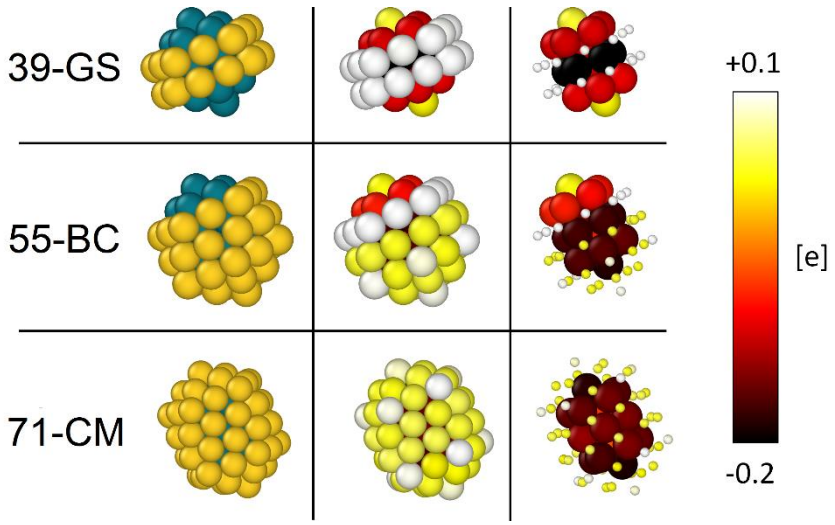

Figure 6. Left panel: morphologies from the classical MD and DFT-relaxed. Au coloured in gold, Rh in blue. Central and right panels: distribution of charge unbalance, accordingly to the colour map. Right panel: Au atoms are shrunk to ease the visualisation of the Rh charge unbalances. Au vertexes are positively charged, while Rh is more negative when covered by Au. Details on the calculations are given in the Computational methods section.

Conclusions

In this chapter, I studied the formation and the physical properties of AuRh nanoalloys, between 20 and 150 atoms, by means of a multiscale protocol involving molecular MD and DFT simulations. Among the tested synthetic procedures, the one-by-one growth produces the most favourable geometries, especially when Au atoms are deposited over a Rh seed. Such processes generate structures with exotic shapes, whose growth is driven by the symmetry assumed by of the Rh seed, and turned to have extremely interesting physical features. All simulations generate structures marked by a strong phase segregation presenting a Rh@Au core-shell ordering. Any other

arrangement resulted to be highly unstable, sometimes even at room temperature (as in the case of randomly mixed chemical ordering). All tested AuRh nanoalloys are characterised by a remarkably high melting temperature, sometimes above 1000K, even in cases where the Rh content is below 20%. Moreover, I noticed that structures presenting geometrical closures resulted particularly stable at high temperature. Ab-initio investigations performed on structures built from a Rh_{19} seed revealed that the shape assumed by the inner parts of the nanostructures plays a major role in determining the system physical features, especially regarding the magnetic moment and HOMO-LUMO gap. An analysis of the charge distribution demonstrates the existence of a net charge separation within the nanoclusters, with gold atoms withdrawing electrons from rhodium. This suggests the existence of optically active charge transfer transitions that could play a major role in the system photocatalytic capabilities. To date these are nothing more than theoretical speculations, however I strongly believe this route deserves to be explored since it could bring massive theoretical and practical improvements in the use of AuRh nanosystems as effective photocatalysts. Globally, these results represent a solid step toward the comprehension of the dynamics and the physical properties of these notable nanoclusters.

References

1 I. Chorkendorff and J. W. Niemantsverdriet, *Concepts of Modern Catalysis and Kinetics*, Wiley-VCH, Weinheim, Germany, 3rd Editio., 2003.

2 R. Jin, *Nanoscale*, 2015, **7**, 1549–1565.

3 I. Chakraborty and T. Pradeep, *Chem. Rev.*, 2017, **117**, 8208–8271.

4 M. Vanzan and S. Corni, *J. Phys. Chem. A*, 2018, **122**, 6864–6872.

5 O. J. H. Chai, Z. Liu, T. Chen and J. Xie, *Nanoscale*, 2019, **11**, 20437–20448.

6 M. Vanzan, T. Cesca, B. Kalinic, C. Maurizio, G. Mattei and S. Corni, *ACS Photonics*, 2021, **8**, 1364–1376.

7 A. S. Lapp, Z. Duan, N. Marcella, L. Luo, A. Genc, J. Ringnalda, A. I. Frenkel, G. Henkelman and R. M. Crooks, *J. Am. Chem. Soc.*, 2018, **140**, 6249–6259.

8 G. W. Piburn, H. Li, P. Kunal, G. Henkelman and S. M. Humphrey, *ChemCatChem*, 2018, **10**, 329–333.

9 V. Amendola, V. Torresan, D. Forrer, A. Guadagnini, D. Badocco, P. Pastore, M. Casarin, A. Selloni, D. Coral, M. Ceolin, M. B. Fernandez Van Raap, A. Busato, P. Marzola and A. E. Spinelli, *ACS Nano*, 2020, **14**, 12840–12853.

10 D. T. L. Alexander, D. Forrer, E. Rossi, E. Lidorikis, S. Agnoli, G. D. Bernasconi, J. Butet, O. J. F. Martin and V. Amendola, *Nano Lett.*, 2019, **19**, 5754–5761.

11 S. Seraj, P. Kunal, H. Li, G. Henkelman, S. M. Humphrey and C. J. Werth, *ACS Catal.*, 2017, **7**, 3268–3276.

12 L. Luo, Z. Duan, H. Li, J. Kim, G. Henkelman and R. M. Crooks, *J. Am. Chem. Soc.*, 2017, **139**, 5538–5546.
13 H. Okamoto and T. B. Massalski, *Bull. Alloy Phase Diagrams*, 1984, **5**, 384–387.
14 P. Villars, Au-Rh Binary Phase Diagram 0-100 at. % Rh, https://materials.springer.com/isp/phase-diagram/docs/c_0900246.
15 N. Kang, Q. Wang, R. Djeda, W. Wang, F. Fu, M. M. Moro, M. D. L. A. Ramirez, S. Moya, E. Coy, L. Salmon, J. L. Pozzo and D. Astruc, *ACS Appl. Mater. Interfaces*, 2020, **12**, 53816–53826.
16 H. Li, L. Luo, P. Kunal, C. S. Bonifacio, Z. Duan, J. C. Yang, S. M. Humphrey, R. M. Crooks and G. Henkelman, *J. Phys. Chem. C*, 2018, **122**, 2712–2716.
17 D. Kim, H. Nam, Y. H. Cho, B. C. Yeo, S. H. Cho, J. P. Ahn, K. Y. Lee, S. Y. Lee and S. S. Han, *ACS Catal.*, 2019, **9**, 8702–8711.
18 X. Wang, H. Wang, N. Maeda and A. Baiker, *Catalysts*, 2019, **9**, 937.
19 X. Wang, N. Maeda, D. M. Meier and A. Baiker, *ChemCatChem*, 2021, **13**, 438–444.
20 Z. Konuspayeva, P. Afanasiev, T. S. Nguyen, L. Di Felice, F. Morfin, N. T. Nguyen, J. Nelayah, C. Ricolleau, Z. Y. Li, J. Yuan, G. Berhault and L. Piccolo, *Phys. Chem. Chem. Phys.*, 2015, **17**, 28112–28120.
21 S. García, L. Zhang, G. W. Piburn, G. Henkelman and S. M. Humphrey, *ACS Nano*, 2014, **8**, 11512–11521.
22 R. Camposeco, M. Hinojosa-Reyes, S. Castillo, N. Nava and R. Zanella, *Environ. Sci. Pollut. Res.*, 2020, **28**, 10734–10748.
23 X. Zhao, Y. Jia, R. Dong, J. Deng, H. Tang, F. Hu, S. Liu and X. Jiang, *Chem. Commun.*, 2020, **56**, 10918–10921.
24 Z. Konuspayeva, G. Berhault, P. Afanasiev, T. S. Nguyen, S. Giorgio and L. Piccolo, *J. Mater. Chem. A*, 2017, **5**, 17360–17367.
25 L. Piccolo, Z. Y. Li, I. Demiroglu, F. Moyon, Z. Konuspayeva, G. Berhault, P. Afanasiev, W. Lefebvre, J. Yuan and R. L. Johnston, *Sci. Rep.*, 2016, **6**, 35226.
26 L. Vitos, A. V. Ruban, H. L. Skriver and J. Kollár, *Surf. Sci.*, 1998, **411**, 186–202.
27 G. Wang, Y. Xu, P. Qian and Y. Su, *Comput. Mater. Sci.*, 2021, **186**, 110002.
28 I. Demiroglu, Z. Y. Li, L. Piccolo and R. L. Johnston, *Catal. Sci. Technol.*, 2016, **6**, 6916–6931.
29 I. Demiroglu, T. E. Fan, Z. Y. Li, J. Yuan, T. D. Liu, L. Piccolo and R. L. Johnston, *Faraday Discuss.*, 2018, **208**, 53–66.
30 G. Rossi and R. Ferrando, *Comput. Theor. Chem.*, 2017, **1107**, 66–73.
31 Z. Valizadeh and M. Abbaspour, *J. Phys. Chem. Solids*, 2020, **144**, 109480.
32 P. C. Chen, M. Gao, S. Yu, J. Jin, C. Song, M. Salmeron, M. C. Scott and P. Yang, *Nano Lett.*, 2021, **21**, 6684–6689.
33 Y. Shubin, P. Plyusnin, M. Sharafutdinov, E. Makotchenko and S. Korenev, *Nanotechnology*, 2017, **28**, 205302.
34 A. S. Chaves, M. J. Piotrowski and J. L. F. Da Silva, *Phys. Chem. Chem. Phys.*, 2017, **19**, 15484–15502.
35 F. Buendía, J. A. Vargas, R. L. Johnston and M. R. Beltrán, *Comput. Theor. Chem.*, 2017, **1119**, 51–58.
36 R. Ferrando, J. Jellinek and R. L. Johnston, *Chem. Rev.*, 2008, **108**, 845–910.
37 F. Calvo, *Nanoalloys: From Fundamentals to Emergent Applications*, Elsevier, 2013.

38 LoDiS software, https://github.com/kcl-tscm/LoDiS.
39 V. Rosato, M. Guillope and B. Legrand, *Philos. Mag. A Phys. Condens. Matter, Struct. Defects Mech. Prop.*, 1989, **59**, 321–336.
40 F. Cleri and V. Rosato, *Phys. Rev. B*, 1993, **48**, 22–33.
41 L. Delgado-Callico, K. Rossi, R. Pinto-Miles, P. Salzbrenner and F. Baletto, *Nanoscale*, 2021, **13**, 1172–1180.
42 F. Baletto, C. Mottet and R. Ferrando, *Chem. Phys. Lett.*, 2002, **354**, 82–87.
43 K. Rossi, L. Bartok-Pártay, G. Csányi and F. Baletto, *Sci. Rep.*, 2018, **8**, 1–9.
44 D. Schebarchov, F. Baletto and D. J. Wales, *Nanoscale*, 2018, **10**, 2004–2016.
45 M. Vanzan, M. Rosa and S. Corni, *Nanoscale Adv.*, 2020, **2**, 2842-2852.
46 F. Baletto, *J. Phys. Condens. Matter*, 2019, **31**, 113001.
47 J. P. Perdew, K. Burke and M. Ernzerhof, *Phys. Rev. Lett.*, 1996, **77**, 3865–3868.
48 P. Giannozzi, S. Baroni, N. Bonini, M. Calandra, R. Car, C. Cavazzoni, D. Ceresoli, G. L. Chiarotti, M. Cococcioni, I. Dabo, A. D. Corso, G. Fratesi, S. De Gironcoli, R. Gebauer, U. Gerstmann, C. Gougoussis, A. Kokalj, L. Martin-Samos, N. Marzari, F. Mauri, R. Mazzarello, S. Paolini, A. Pasquarello, L. Paulatto, C. Sbraccia, S. Scandolo, A. P. Seitsonen, A. Smogunov, P. Umari and R. M. Wentzcovitch, *J. Phys. Condens. Matter*, 2009, **21**, 395502.
49 P. Giannozzi, O. Andreussi, T. Brumme, O. Bunau, M. Buongiorno, M. Marsil, L. Paulatto and D. Rocca, *J. Phys. Condens. Matter*, 2017, **29**, 465901.
50 G. Henkelman, A. Arnaldsson and H. Jónsson, *Comput. Mater. Sci.*, 2006, **36**, 354–360.
51 E. Sanville, S. D. K. Kenny, R. Smith and G. Henkelman, *J. Comput. Chem.*, 2007, **28**, 899–908.
52 W. Tang, E. Sanville and G. Henkelman, *J. Phys. Condens. Matter*, 2009, **21**, 84204.
53 M. Settem, *J. Alloys Compd.*, 2020, **844**, 155816.
54 F. Baletto and R. Ferrando, *Rev. Mod. Phys.*, 2005, **77**, 371–423.
55 A. Stukowski, *Model. Simul. Mater. Sci. Eng.*, 2010, **18**, 015012.
56 J. Li, X. Li, H. J. Zhai and L. S. Wang, *Science*, 2003, **299**, 864–867.
57 C. C. Chang and J. J. Ho, *Phys. Chem. Chem. Phys.*, 2014, **16**, 5393–5398.
58 W. R. Tyson, *Can. Metall. Q.*, 1975, **14**, 307–314.
59 O. López-Estrada, E. Orgaz and F. Baletto, *J. Mater. Chem. C*, 2020, **8**, 2533–2541.
60 W. J. Debonte and J. M. Poate, *Thin Solid Films*, 1975, **25**, 441–448.
61 K. Palotás, L. Óvári, G. Vári, R. Gubó, A. P. Farkas, J. Kiss, A. Berkó and Z. Kónya, *J. Phys. Chem. C*, 2018, **122**, 22435–22447.
62 D. R. Lide, W. M. M. Haynes, G. Baysinger, L. I. Berger, H. V Kehiaian, D. L. Roth, D. Zwillinger, M. Frenkel and R. N. Goldberg, *CRC Handbook of Chemistry and Physics*, 2010.
63 C. Kittel and P. McEuen, *Introduction to solid state physics*, 1998, vol. 7.

Conclusions and perspectives

This PhD thesis is devoted to investigate the mechanisms underlying energy and charge transfer processes occurring between nanostructures and molecular species in the presence of an external electromagnetic field, through the application of various computational methodologies based on ab-initio calculations and classical atomistic techniques.

Each of the four main chapters constituting this thesis aims to focus on a specific aspect of light stimulated nanostructure-molecule interactions in technologically relevant devices or in simplified model systems. This provided new insights on energy and charge transfers phenomena which in some cases resulted to be intimately connected. Unfortunately, exploring those effects was not directly possible for all cases accounted, since exploring such features would require a prior extensive characterization of the unexcited systems which were not available when I first started my PhD. An adequate treatment of the energy and charge transfers processes in these hybrid nanosystems indeed requires particular attention from a computational point of view even in the case of ground-state calculations since the system have an intrinsic multiscale nature. As example, just remind that typical dimensions for plasmonic devices are in the order of 10-100 nm while the typical length of common molecular species are usually smaller than 1 nm. While the latter can be easily handled and studied via first-principles techniques, the former necessarily need some approximation, being a complete first-principle treatment computationally unfeasible.

In order to tackle this problem, I therefore had to make some necessary simplifications to the systems explored. These approximations were chosen in accordance with the problems under study and were always weighed against the type of detail the system required.

In chapter one, for example, the approximation lies in the fact that the object of study is the sole nanocluster and its optical properties, embedded in a certain environment. Here I decided to ignore the presence of the lanthanide as well as the possible resonance effects generated by the presence of a time-resolved light pulse. Although this naturally loses some of the underlying physics, it has allowed me to explore the theoretical behaviour of a set of nanostructured systems and validate, against experimental data, a unifying theoretical approach which can interpret the energy transfer processes occurring in these systems.

In chapter two I could not directly explore the photophysical feature of the reaction since an exhaustive treatment of the ground state properties of the system were lacking. It was then necessary to study the thermal catalysed reaction path, and this required certain approximations.

The main one was that the metallic nanoparticle were modelled as a slab of finite thickness, over which the dynamics of the various reaction intermediates were estimated with ab-initio accuracy. In this way, the contribution the bulk-like electronic structure of the nanoparticle could have toward the dynamics reaction was lost. In addition, I have found that the choice of the appropriate exchange-correlation functional can severely affect the results and thus can represent a further source of inaccuracy. Despite their presence, these simplifications were necessary to characterise the thermodynamics of the CO_2 reduction rate determining step and to lay the foundations for a more in-depth study of the photophysical properties of this process. I would here like to mention that further explorations in this sense are currently being developed following two different approaches, which describe differently the effects the external electric field has toward the system. As mentioned in the Introduction of this thesis, such approaches consist in (i) modelling the nanoparticle-molecule interface through multiscale model based on continuum and atomistic techniques and treating the light-stimulated effects by exploiting real-time dynamics of the polarized system wavefunction and (ii) investigate the thermodynamic profile of the rate determining step in the excited states, adopting a fully atomistic approach based on both DFT calculations and many body perturbation theory techniques. The expectations for these investigations are remarkable: these indeed can unravel the true mechanism underlying the metal-catalysed CO_2 photoreduction and give valuable indications about the role played by the energy and charge transfer processes.

The third chapter is perhaps the one that suffers most from approximations both on the definition of the model system and in the calculation accuracy. Here, major simplifications have been made to the structure of the nanoparticle in order to study how a charge injection can also be accompanied by an energy transfer. Moreover, unfortunately, the presence of computational artefacts within the code prevented me to include the dynamics of the ions in the calculation and this further increased the degree of simplification, this time affecting the calculation methodology. Notwithstanding these strong approximations, in this chapter I was able to demonstrate how charge injection can be also accompanied by energy transfers that can selectively activate certain vibrational modes within the molecule. This in turn provides new evidences on the mechanism interplaying between charge and energy transfers and on how this could have important consequences in photocatalysis.

Finally, in the fourth and last chapter, I decided to adopt a different approach: instead of accounting for certain assumptions about the nanoalloys structures treating it at the first-principle level form the beginning, I have chosen to start the exploration by analysing how these alloys can be formed

in certain conditions and which are the main structural features emerging during the synthesis of those systems, by means of molecular dynamics calculations. Using these techniques on systems with such small dimension (20-150 atoms) and thus intrinsically affected by quantum confinement effects is limiting. However, such protocol could rapidly provide geometries that were then investigated with more refined ab-initio tecniques. By exploiting this multiscale protocol, I was able to obtain a set of particularly interesting nanoalloyed structures, to validate their stability and to characterise them from a structural and physical point of view. More investigations on the optical properties of those systems will be performed in the next months, also thanks to a newly obtained HPC-EUROPA3 grant award, aimed to support a 3-months visiting period during 2022 by granting financial contributions and access to computational facilities. I am convinced that this study will provide new and stimulating insights on the nature of energy and charge transfer phenomena within bimetallic nanosystems and on how this reflects in photocatalysis. Indeed, as demonstrated in chapter 1, there exist alloyed nanosystems which can sustain effective energy transfer and provide energy to a coupled species. This, joined to the fact that within these systems there can be production of excited carriers, naturally lead to the hypothesis that within these system energy and charge transfer effects may cooperate. Studying those systems could then provide new and deeper comprehension of these phenomena.

Globally, the various investigation performed during my PhD have provided new perspectives and in the field of light-stimulated energy and charge transfer processes at the nanoscale, suggesting those mechanism cannot be in principle treated separately.

Compared to the initial state of the art, my contribution expands the range of theoretical tools that can be adopted to study photo stimulated phenomena, while provide original data on specific relevant nanosystems; thus enriching our knowledge on this fascinating field of nanoscience and contributing to unravel the fundamental mechanism behind plasmonic-mediated photochemistry.

Ringraziamenti

Con questa tesi di dottorato si chiude un cammino che, nonostante le apparenze, è iniziato ben più di tre anni fa. Sin da quando ho memoria, il mio obiettivo di vita è stato quello di diventare uno scienziato. Che fossi un bambino ingenuo o un adolescente scapestrato, nel mio futuro ho sempre visto libri contenenti formule complicate, strumenti all'avanguardia, ed un uomo dal camice bianco alla ricerca di qualcosa che avrebbe cambiato il mondo.

Ora, all'età di 28 anni, non sono circondato da strumenti sofisticati, non indosso il camice bianco e certamente non ho cambiato il mondo. Eppure, in un certo senso, posso dire di essermi avvicinato come mai prima d'ora all'uomo che sognavo di essere. E riflettendo su tutta la strada percorsa dal momento in cui ho intrapreso questa via, il cuore mi si riempie di orgoglio, soddisfazione e sincera gratitudine. Vorrei quindi dedicare le ultime righe di questo lavoro a tutti coloro che, direttamente o meno, mi hanno consentito di arrivare fin qui.

Sono grato in primo luogo alla mia famiglia, per aver sempre sostenuto le mie scelte e aver creduto nelle mie capacità anche quando io non ero in grado di farlo; per avermi festeggiato nei momenti di gioia ed avermi sostenuto in quelli di sconforto. Senza di loro non sarei la persona che sono oggi.

Vorrei poi ringraziare coloro che, con pazienza e dedizione, mi hanno accompagnato in questi anni di formazione e mi hanno guidato in questo lungo e faticoso percorso. Ringrazio in particolare dal più profondo del cuore le persone che mi hanno guidato negli ultimi tre anni: il Prof. Stefano Corni, la Prof.ssa Francesca Baletto e la Dr.ssa Margherita Marsili. Sono stati specialmente loro che con insegnamenti, consigli e ragguagli mi hanno trasformato nel ricercatore che sono ora.

Immancabili in questi ringraziamenti i colleghi del gruppo di ricerca di Padova. Incoraggianti nell'amarezza, preziosi nel dubbio e complici nella spensieratezza, loro sono stati attori fondamentali negli ultimi tre anni della mia vita. Grazie a tutti voi.

Vorrei poi esprimere la mia riconoscenza ai miei più cari amici, coloro che in questi tre anni hanno condiviso con me momenti di indimenticabile felicità, profonda riflessione e che mi hanno dato sempre il più solido sostegno nei momenti più bui. Vi voglio bene.

E' solo mentre scrivo queste ultime parole che realizzo davvero come unendo opportunamente passione, forza di volontà e le giuste persone, non esistono obiettivi che non si possano raggiungere. E per aver vissuto finora una vita densa di questi tre elementi, mi sento estremamente fortunato.

Grazie a tutti, per tutto.